UC San Diego
UC San Diego Electronic Theses and Dissertations

Title

Pulsed laser microbeams for cellular manipulation : applications in cell biology and microfluidics

Permalink

https://escholarship.org/uc/item/7mm44161

Author

Hellman, Amy Noel Stacy

Publication Date

2008

Peer reviewed|Thesis/dissertation

UNIVERSITY OF CALIFORNIA, SAN DIEGO

Pulsed Laser Microbeams for Cellular Manipulation:
Applications in Cell Biology and Microfluidics

A dissertation submitted in partial satisfaction of the
requirements for the degree of
Doctor of Philosophy

in

Bioengineering

by

Amy Noel Stacy Hellman

Committee in charge:

University of California, San Diego

     Professor Shu Chien, Chair
     Professor Vasan Venugopalan, Co-chair
     Professor Nancy L. Allbritton
     Professor Sadik Esener
     Professor Bernhard O. Palsson

2008

The Dissertation of Amy Noel Stacy Hellman is approved, and it is acceptable in quality and form for publication on microfilm and in digital formats:

_____

_____

_____

_____
Co-Chair

_____
Chair

University of California, San Diego

2008

To my family.
Without their love and support,
this dissertation would not have been possible.

TABLE OF CONTENTS

LIST OF FIGURES

LIST OF TABLES

ACKNOWLEDGEMENTS

Thank you to Dr. Elliot Botvinick, who I hold partially responsible for the past 5 years, as he talked me into getting a Ph.D. in the first place! His innovative ideas and enthusiasm have been extremely motivating and he is a joy to work with. I am also grateful to Dr. Michael Berns for allowing me to rotate in his lab and introducing me to the Beckman Laser Institute, as well as other members of the BLI: Chung-Ho Sun for her expertise in cell biology and biochemistry, Linda Li for training me in cell culture techniques, and Tatiana Krasieva for being an invaluable resource in microscopy techniques.

I especially thank Dr. Carole Hayakawa, not only for her computational assistance in the modeling work of this dissertation, but for being a great friend. Whether it was lending mathematical expertise or listening to a practice presentation, she always provided much insight and constructive feedback, and makes working in the lab enjoyable. Also, thank you to Dr. Kaustubh Rau, who was a postdoc in the lab when I joined and passed on an invaluable amount of information and training that made this dissertation possible.

I'd like to thank my parents, Robert and Christine Stacy, and my sister, Heidi Ehrbar, for their endless love and support. They always listened even when they had no idea what I was talking about, encouraged me to take the next step, and taught me that I can do anything I set my mind to. I could not have done this without them. I'd also like to thank Howard, Jean, and James Hellman, for their love and interest and support. I am blessed to have such a wonderful family.

I would especially like to thank my loving husband Scott for his patience and support through the past five years (and especially the last few months!). He always gives me something to look forward to, makes my life truly balanced, and is my best friend.

Amy Hellman

EDUCATION

Ph.D.   University of California, San Diego, Bioengineering (2008)
M.S.   University of California, San Diego, Bioengineering (2004)
B.S.   University of California, Santa Barbara, Chemical Engineering (2001)

RESEARCH AND PROFESSIONAL EXPERIENCE

Graduate Student Researcher (01/04 – present)
Department of Chemical Engineering, University of California, Irvine
Department of Bioengineering, University of California, San Diego

R&D Systems Engineering Intern (06/05 – 09/05)
Edwards Lifesciences LLC, Irvine, CA

Undergraduate Student Researcher (06/99 – 06/01)
Department of Chemical Engineering & Materials Science,
Materials Research Laboratory, University of California, Santa Barbara

TEACHING EXPERIENCE

Instructor, Chemistry (01/08 – present)
Orange Coast College, Costa Mesa, CA

Chemistry Teaching Intern (08/07 – present)
California Community College Internship Program
Orange Coast College, Costa Mesa, CA

Graduate Teaching Assistant
Tissue Engineering (Spring 2004), Biochemistry (Fall 2004), Molecular Physical Chemistry (Spring 2003)
Department of Bioengineering, University of California, San Diego

HONORS AND AWARDS

Graduate Research and Education in Adaptive Bio-Technology Training Fellowship, University of California Biotechnology Research and Education Program (2006-2008),
Graduate Teaching Assistant Excellence Award (2004),
National Science Foundation Graduate Research Fellowship Award (2001-2005),
Chancellor's Award for Excellence in Undergraduate Research, UCSB (2001)

JOURNAL PUBLICATIONS (former name: Amy Stacy)

1. "Biophysical Response to Laser Microbeam-Induced Cell Lysis and Molecular Delivery." AN Hellman, KR Rau, H Yoon, V Venugopalan. *Journal of Biophotonics*, 2008: 1(1), 24-35.

2. "Laser-induced mixing in microfluidic channels." AN Hellman, KR Rau, H Yoon, S Bae, JF Palmer, KS Phillips, NL Allbritton, V Venugopalan. *J Analytical Chemistry*, 2007: (79) 4484-4492.

3. "Laser microbeam induced cell lysis: Time-resolved imaging and analysis of hydrodynamic effects." KR Rau, AN Hellman, PA Quinto-Su, V Venugopalan. *Biophysical Journal*, 2006: (91)1, 317-329.

4. "Combined photodynamic and photothermal induced injury enhances damage to in vivo model blood vessels." KM Kelly, S Kimel, T Smith, AN Stacy, MJ Hammer-Wilson, LO Svaasand, JS Nelson. *Lasers Surg Med*. 2004;34(5), 407-413.

CONFERENCES

1. "Integrated Laser-Microbeam Platform for Cell Lysis and Molecular Delivery." AN Hellman, KR Rau, HH Yoon, PA Quinto-Su, NL Allbritton, and V Venugopalan. University of California Biotechnology Research and Education Program Annual Retreat, Monterey, CA. November 2007.

2. "Biological Response to Laser-Generated Cavitation Bubble Induced Cell Lysis and Molecular Delivery." AN Hellman, KR Rau, HH Yoon, PA Quinto-Su, and V Venugopalan. Biomedical Engineering Society Annual Fall Meeting, Los Angeles, CA. September 2007.

3. "Laser-Induced Mixing in Microfluidic Channels to Initiate Biochemical Reactions." AN Hellman, KR Rau, HH Yoon, S Bae, JF Palmer, KS Phillips, NL Allbritton, and V Venugopalan. Biomedical Engineering Society Annual Fall Meeting, Los Angeles, CA. September 2007.

4. "Effects of pulse duration and pulse energy on laser microbeam-induced cell lysis and membrane permeabilization." AN Hellman, KR Rau, PA Quinto-Su, and V Venugopalan. European Conferences on Biomedical Optics. International Conference Centre, Munich, Germany. June 2007.

5. "Analysis of pulsed laser microbeam-induced cell lysis and membrane permeabilization using pulses ranging from 180 ps to 6 ns." Hellman, A, Rau, KR, Quinto-Su, P, and Venugopalan, V. SPIE Photonics West Conference, San Jose, CA. January 2007.

6. "Analysis of varying pulse duration on laser-induced cell manipulations using time-resolved imaging." Hellman, A, Rau, KR, Quinto-Su, P, and Venugopalan, V. Biomedical Engineering Society Annual Fall Meeting, Chicago, IL. October 2006.

ABSTRACT OF THE DISSERTATION

Pulsed Laser Microbeams for Cellular Manipulation:
Applications in Cell Biology and Microfluidics

by

Amy Noel Stacy Hellman

Doctor of Philosophy in Bioengineering

University of California, San Diego, 2008

Professor Shu Chien, Chair
Professor Vasan Venugopalan, Co-Chair

Highly focused pulsed laser radiation (pulsed laser microbeams) provide the ability to deposit energy with high spatial precision and controllable cellular damage. As a result, pulsed laser microbeams have been explored as a fast, non-contact means for cellular manipulations such as cellular microsurgery, transient cell membrane permeabilization, and targeted cell lysis.

In this dissertation we examine the mechanisms of highly focused laser microbeams of nanosecond and picosecond duration to achieve cell lysis, cell necrosis, and molecular delivery. We have developed a time-resolved imaging system to

visualize these processes with nanosecond temporal resolution and use image analysis to measure the physical perturbation applied to the cells as a function of laser microbeam pulse energy and pulse duration. Fluorescence assays are used to assess the biological response (necrosis, molecular delivery, and biochemical pathway activity) to the laser microbeam irradiation, and a biophysical model is developed to establish connections between specific physical characteristics and the resulting cellular effect.

Our studies reveal that pulsed laser microbeam processes are mediated by optical breakdown resulting in plasma formation, shock wave emission, and cavitation bubble formation, expansion, and collapse. Cavitation bubble expansion was found to be the primary mechanism responsible for cellular modification. Hydrodynamic analysis based on the measured time evolution of the cavitation bubble growth, combined with assessment of the cellular response, revealed that the maximum wall shear stress associated with the cavitation bubble expansion governs the location and spatial extent of cell lysis, cell necrosis, and molecular delivery. In addition, we demonstrate how the variation of laser microbeam pulse duration can allow modulation of the spatial extent of cellular modification in order to tailor the cellular perturbations and optimize specific applications.

These detailed studies provide a basis for the informed selection of specific laser parameters (i.e. pulse duration and energy) to achieve a desired cellular outcome, with controllable degrees of collateral damage. We demonstrate three different applications in which the laser parameters are well matched for particular applications in cellular analytics, activation of biochemical pathways, and microfluidics.

Chapter 1

INTRODUCTION

In this chapter I provide an overview of the history of laser microbeams and their progression as research tools in biological applications. I will present various uses of pulsed laser microbeams in biotechnology, followed by the rationale supporting our study of the mechanisms governing interactions of pulsed laser microbeams with cells. Finally, I will delineate the overall goals of the research and present an outline of this dissertation.

1.1 Historical Development of Laser Microbeams

In cell biology, pulsed laser radiation focused at high numerical apertures (i.e., pulsed laser microbeams) has been used to create damage on cellular and sub-cellular levels for over 40 years [12, 54]. Pulsed laser microbeams provide the ability to deposit energy with high spatial precision and controllable cellular damage, and thus offer a fast, non-contact means for cellular manipulation. The ongoing development of available laser, optics, microscopy, and image processing technologies holds great promise for the increasing utilization of laser microbeams in cell biology and biotechnology in the 21st century.

As recounted in recent reviews of laser nanosurgery [6, 133], the first studies examining the use of photons to inactivate cells or cell organelles were conducted by Tschachotin in 1912 using an incoherent UV light source. In these experiments, a quartz microscope objective was used to focus the 280 nm emission of a magnesium spark to a 5-μm diameter spot size on a cell. The use of incoherent UV light sources for cell manipulations was accelerated by the development of UV transmitting quartz objectives, providing the ability to focus the UV light to a sub-micrometer beam diameter by the 1950s. Despite these improvements, conventional light sources provided low intensities, and required long exposure times to achieve the desired effect.

The invention of the ruby laser in 1960 provided a high-intensity, collimated, monochramatic light source, enabling reduction of the exposure time to the microsecond range [13]. The first experiments on mitochondrial inactivation utilized ruby laser pulses of ~ 500 μs duration focused to a 5-μm diameter spot [2, 113]. Shortly thereafter, Berns and co-workers applied the newly developed continuous wave (CW) argon laser to study many aspects of cell biology including cell repair, development, and organelle function [7-9]. The improved quality and shorter wavelength of the argon laser beam allowed much smaller laser microbeam diameters than the initial ruby lasers and provided more precise cellular manipulation, often with the use of exogenous dyes such as acridine orange [133].

Advances in laser technology offered improved capabilities for cellular microbeam studies and provided the basis to explore the effects of key laser parameters, including wavelength and pulse duration, on the resulting cellular effect [6]. Further reductions in pulse duration became available with the invention of Q-switched

nanosecond lasers in 1962 because of the ability to drive nonlinear (multiphoton) processes [11, 12, 19].   This is particularly significant because nonlinear optical processes provide more localized energy deposition at selected locations, allowing more precise cellular microsurgery without the use of exogenous photochemical sensitizing agents [133]. Principal among these processes are multiphoton absorption and optical breakdown leading to laser-induced plasma formation (ionization). Laser parameters such as wavelength, pulse duration, pulse energy, and focusing angle play a fundamental role in the interactions of pulsed laser microbeam irradiation with cells. Yet is has only been in the last five years that significant attention has been given to the relationship between the selected laser parameters and the resulting cellular effects [92-94, 126, 128, 133, 136]. To better establish this relationship, we must first (a) measure and characterize the physical perturbations offered by the delivery of pulsed laser microbeams to cells; (b) model the physical process to establish relationships between specific characteristics of the physical perturbations and the resulting biological response; and (c) explore specific applications that best utilize the physical perturbations offered by specific laser parameters. This study is essential for the continued development of laser microbeams as analytical tools in biotechnology and is the central motivation of this dissertation.

1.2   Applications of Laser Microbeams in Biology and Biotechnology

Laser microbeams were first utilized as tools in cell biology to reveal fundamental biological processes, demonstrated by their use to produce gene inactivation [10], plasma membrane disruption [72], centrosome ablation [55],

microtubule damage [53], and to study forces in mitotic spindle separation [38] and morphogenesis [47]. However, over the last decade, laser microbeams have been utilized increasingly for applications in biotechnology and cellular analytics.

One example is the use of pulsed laser microbeams for targeted cell lysis to selectively obtain a cell population for cell line expansion and purification. Lin and co-workers have demonstrated the use of 20 ns laser pulses at λ = 532 or 565 nm for selective killing of cells loaded with micro-particles and nano-particles within a mixed cell population [65, 90]. A commercial apparatus utilizing pulsed laser microbeams for targeted cell killing has also been described, offering automated *in situ* cell identification and laser-based elimination to provide high yield and high purity of the desired cells within a mixed cell population [84]. Similarly, the Allbritton group has developed micropallet arrays utilizing pulsed laser microbeams to provide rapid, nondisruptive isolation of single adherent cells from a heterogeneous population [98, 99, 138].

Another application receiving interest is the use of pulsed laser microbeams to load membrane-impermeant molecules into cells [25, 61, 95, 109, 117, 123]. Efficient delivery of molecules into living cells is essential in many fields including basic research, applied drug discovery, and gene therapy [25]. The most commonly used methods for loading membrane impermeant molecules into cells include microinjection [22, 40], electroporation [34, 141], liposomal delivery [33], and protein transduction domains [5]. Each of these methods has found utility within specific applications, but most exhibit varying degrees of toxicity, limiting their use to robust cell types [25]. The processes of laser-induced optoinjection and optoporation offer the ability to load

cells with a variety of biomolecules on short time scales (milliseconds to seconds) through optically produced cell membrane permeabilization. Despite recent reports utilizing lasers to deliver molecules into cells, very little is known about the optoporation process, and the technique has not been widely adopted. The mechanisms governing this process will be investigated in this dissertation.

Pulsed laser microbeams have also found utilization in the fields of proteomic and genomic analysis. Procurement of specific samples of histologic material has become important with the increasing refinement of analytic techniques, while separation and transport of living cells is of interest for stem cell research, organ culture, and tissue engineering [30, 130]. Rapid, non-contact and contamination-free separation can be achieved by laser microdissection (LMD) of the sample of interest, followed by laser pressure 'catapulting' (LPC) of the dissected material for further analysis. These techniques utilize 3 nanosecond UV laser pulses ($\lambda = 337$ nm), and have been successfully applied in many fields to study intracellular structures and gene expression in the native *in vivo* environment of intact tissue [27, 30, 130]. This method can potentially provide results that will pave the way toward high-throughput profiling of tissue-specific gene expression using Gene Chips arrays, elucidating molecular pathways to study repair of genetic or metabolic diseases [30].

In the area of single cell bioanalytics, the Allbritton group has developed the laser micropipet system (LMS) for measurement of enzyme activity within single cells [73, 104, 106]. In this technique, a Q-switched (Q-sw) Nd:YAG laser at $\lambda = 532$ nm is used to both lyse a single cell and mix the cellular contents with the surrounding medium. The cell contents are subsequently taken up by a glass capillary positioned

above the cell, wherein they are electrophoretically separated and subsequently analyzed using laser-induced fluorescence. This technique shows great promise for analyzing the activity of biomolecules involved in signalling pathways with nanomolar sensitivity [105]. A particular advantage is the fast time-scale of the lysis process that rapidly stops all biochemical reactions by disrupting the cell and mixing its contents. The non-contact means of laser-based cell lysis is also attractive for integration with microfluidic chip based devices [42]. Laser microbeams are ideal for coupling with microfluidic devices, offering great portability and flexibility in the location of laser microbeam irradiation and subsequent cellular perturbation. The mechanisms underlying pulsed laser microbeam-induced cell lysis, as well as applications for integrating laser microbeams and microfluidic devices will be addressed in this dissertation.

1.3   Goals of the Dissertation

Despite the innovative utilization of laser microbeams in cell biology and biotechnology, only recently have studies been able to provide insight regarding the mechanisms that mediate the interactions of highly focused pulsed laser beams with cells [92-94, 126, 128, 133, 136]. Laser-cell interaction mechanisms can be complex involving photothermal, photochemical, and photomechanical processes [133, 136]. The relative contributions of these processes in a given laser-cell interaction is governed by many factors including irradiation wavelength, pulse duration, pulse energy and microbeam diameter. A deeper understanding of the relationship between the selected

laser parameters and the resulting cellular manipulation is necessary for their continued development as research tools as well as implementation for practical application.

The objectives of this dissertation are four-fold. First, we aim to characterize the mechanisms governing laser microbeam-induced cellular injury, namely cell lysis and molecular delivery, as a function of the selected laser parameters. We will image and measure the physical perturbation applied to the cells, which is mediated by the nonlinear optical processes and subsequent mechanical/thermal dissipation, as a function of pulse energy and pulse duration. Second, we will assess the cellular response to these perturbations to understand the biological effects of the pulsed laser microbeam irradiation. Third, we will develop appropriate biophysical models in an attempt to establish a connection between specific physical characteristics and the resulting cellular effect. Finally, we will demonstrate the use of laser microbeams for applications in cellular analytics and microfluidic devices.

The overall scheme of this thesis is depicted in Figure 1.1. In Chapter 2, I provide a review of the physics of non-linear optical processes that mediate many laser microbeam-cell interactions and describe the impact of laser pulse duration, wavelength, energy, and focusing angle. In Chapter 3, I present our results on the physical mechanisms of laser microbeam cell lysis using 6 nanosecond (ns) pulses using time-resolved imaging. I also introduce a hydrodynamic model that connects the physics of the process to the observed cellular damage. In Chapter 4, I use fluorescence microscopy techniques to relate the physical effects measured in Chapter 3 to the biological response of cells exposed to 6 ns pulses by evaluating the extent of cell lysis, necrosis, and molecular delivery as a function of pulse energy. In Chapter 5, I

investigate the effect of pulse duration (picosecond to nanosecond) on cell lysis and molecular delivery using time-resolved imaging and fluorescence assays. These detailed studies provide a basis for the informed selection of specific laser parameters (i.e. pulse duration and energy) to achieve a desired cellular outcome, with controllable degrees of collateral damage. In Chapters 6 and 7, I provide demonstrations of three different applications in which the laser parameters are well matched to the resulting desired cellular perturbations. In Chapter 6 I will demonstrate the utilization of laser microbeams as a non-contact means to stimulate a biochemical mechanotransduction stress response in cells for potential applications in molecular imaging, disease diagnostics, and therapeutics. In Chapter 7, we explore the integration of laser microbeams with microfluidics, and demonstrate the ability to achieve targeted cell lysis within a microfluidic device. Also in Chapter 7, we utilize picosecond pulses to provide precise localized damage of neuronal axons for the study of central nervous system neuronal injury and regeneration in a microfluidic device. Lastly, I discuss the ability of laser microbeams to provide localized mixing of two fluid streams within the confines of a microfluidic device that might provide a means to subject cells to a transient or repeated exposure of a chemical agonist.
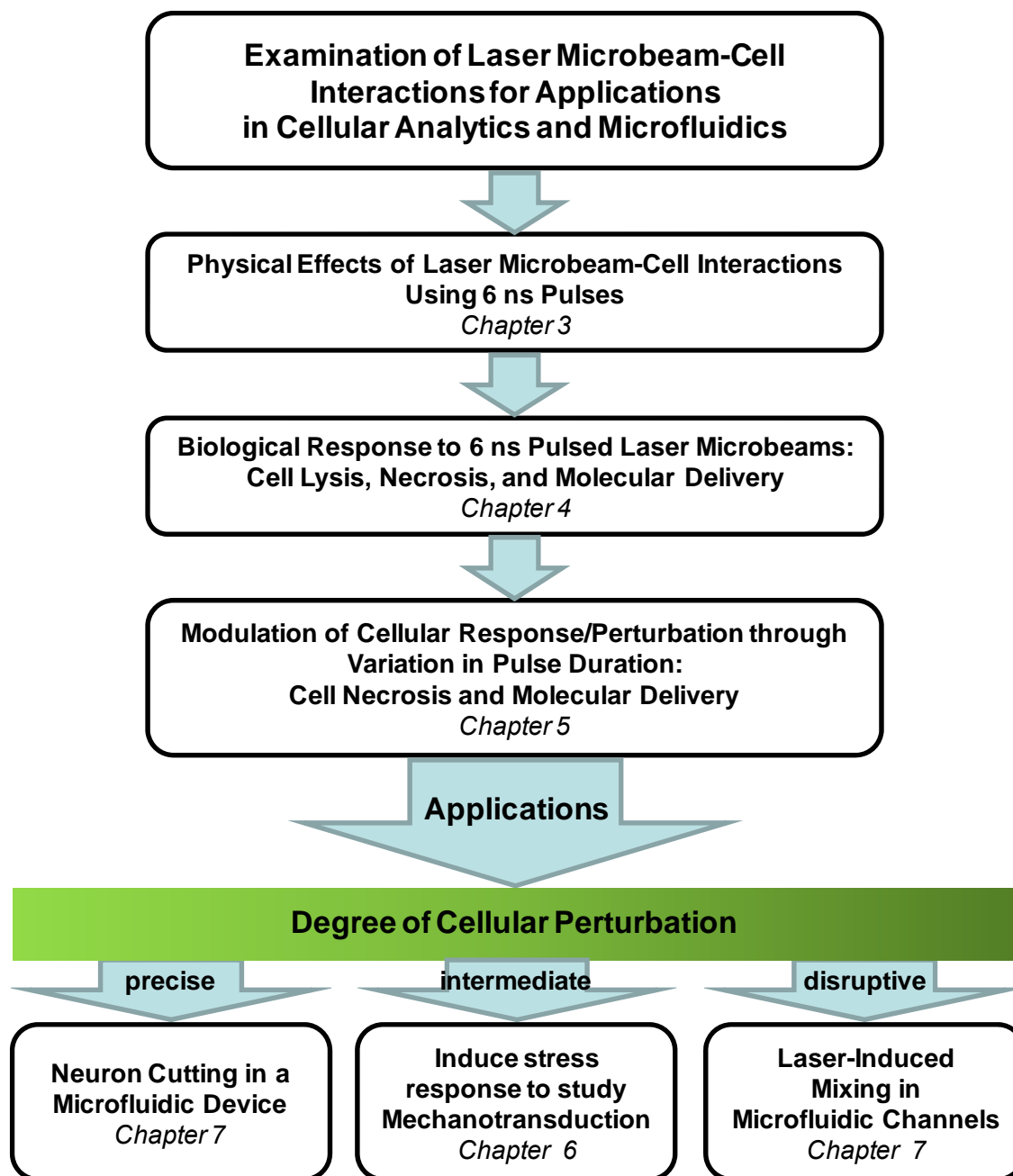
Figure 1.1: Schematic providing outline and objectives of dissertation.

Chapter 2

PHYSICS OF OPTICAL BREAKDOWN

2.1 Introduction

Early in the application of laser microbeams in cell biology, Berns and co-workers noted that non-linear optical processes such as multiphoton absorption may be operative mechanisms for cell damage [11, 12, 19]. Recent work from our group [93, 126] has demonstrated that laser pulse energies and irradiances necessary to achieve the non-linear process of optical breakdown in water using nanosecond laser pulses at $\lambda = 532$ or 1064 nm focused at high numerical aperture are similar to those used in nanosecond pulsed laser microbeam cell lysis and optoinjection [61], and implicate plasma formation as the initiating event for these processes.

In this chapter, we provide an overview of the physical processes involved in the formation of laser-induced plasmas and the role of the resulting thermal and mechanical effects. The dependence of optical breakdown on pulse duration and wavelength will be discussed.

2.2 Nonlinear Absorption: Multiphoton and Avalanche Ionization

In this section, we examine the nonlinear process of optical breakdown in liquids. We are interested in nonlinear absorption processes because at visible and near-

infrared (IR) wavelengths, there is minimal absorption by cellular media [92]. Linear absorption alone is unlikely to provide a sufficient energy density within the focal volume for cellular modification and nonlinear processes must be operative to have the additional advantage of providing a high degree of spatial precision for energy deposition.

Nonlinear absorption means that the absorption coefficient of a medium depends on the intensity of the incident light, and can play an important role in the interactions of high-power laser beams with matter [127]. Figure 2.1 illustrates the process by which plasma formation through laser-induced breakdown occurs in dielectric, non-absorbing media. Essentially, it consists of the formation of quasi-free electrons by an interplay of photoionization and avalanche ionization [133]. For nanosecond laser pulses, the generation of one or a few free electrons results in ionization, leading to plasma formation once a free electron density of $\sim 10^{18}$ e^-/cm^3 is achieved [78]. Because a plasma is an ionized gas, plasma formation always results in bubble formation and in most cases, is accompanied by visible luminescence.

In the absence of linear absorption, both avalanche ionization and multiphoton absorption processes can contribute significantly to plasma formation. Regardless of the dominant mechanism, the initiation of plasma formation when using laser microbeams requires the generation of a free electron which invariably occurs through multiphoton absorption. Water can be modeled as an amorphous semi-conductor with a band gap energy of $\Delta E = 6.5$ eV. Promotion of an electron to the conduction band therefore requires simultaneous absorption of 3 photons at 532 nm (each photon having an energy of 2.34 eV). Once the seed electron is formed, it can absorb photons via a

non-resonant process called 'inverse Bremsstrahlung absorption' (IBA). Absorption of photons increases the kinetic energy of the free electron. Once the kinetic energy of the electron has exceeded the band gap energy, it can produce another free electron via impact ionization. After impact ionization, there are two free electrons with low kinetic energies which can then absorb multiple photons through IBA. This process results in a rapid increase in the number of free electrons, thus the term 'avalanche' ionization. However, the development of an electron 'avalanche' takes time as it requires many 'cycles' of several IBA events followed by impact ionization. As a result, avalanche ionization contributes to laser induced plasma formation only for pulse durations $t_p \geq 10$ ps. It is important to note that the rate of free electron generation using multiphoton ionization scales as $\eta_{MPI} \sim I^k$, with k being the number of photons that must be absorbed simultaneously, while the rate for avalanche ionization scales as $\eta_{AI} \sim I$. As a result, the contribution of multiphoton ionization becomes more substantial as the pulse duration decreases. Moreover, while multiphoton ionization occurs coincident with the absorption event, avalanche ionization takes more time and is unable to contribute to the population of free electrons as the pulse duration decreases. This concept will be discussed in more detail in the following section.
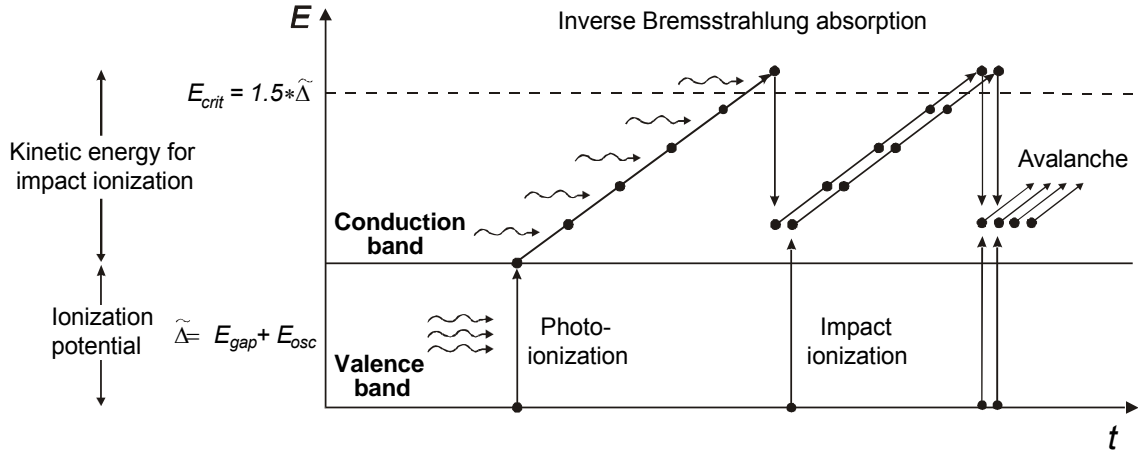
Figure 2.1: Interplay of multiphoton and avalanche ionization in the process of plasma formation. Adapted from Vogel et al., *Applied Physics B*, 2005 [133].

2.3 Impact of Pulse Duration on Optical Breakdown

Table 2.1 lists the irradiance and radiant exposure values required for optical breakdown in water at various pulse durations, as well as the mechanisms dominating the breakdown process. As the pulse duration shortens beyond the order of tens of picoseconds, there is less time to generate additional free electrons through avalanche ionization. Therefore as the laser pulse duration decreases, plasma formation relies increasingly on the generation of free electrons from multiphoton ionization. Even though higher irradiances are reached at shorter pulse durations, the radiant exposure required for optical breakdown still decreases. This provides the opportunity to deposit smaller amounts of energy in the focal volume at shorter pulse durations and enable cellular manipulations of increasing precision.

Table 2.1: Experimental optical breakdown mechanisms for water, breakdown mechanism (AI = avalanche ionization, MPI = Multiphoton ionization), wavelength, focusing angle, breakdown criterion, radiant exposure, and threshold irradiance [133].

Pulse Duration	Breakdown Mechanism	Wave-length [nm]	Focusing Angle	Spot Size [µm]	Breakdown criterion Bubble (B) Luminescence (L)	Radiant Exposure [J/cm^2]	Irradiance x 10^{11} [W/cm^2]
6 ns	AI	532	22°	5.3	L	174	0.29
30 ps	AI/MPI	532	22°	3.4	L	11.3	3.75
100 fs	MPI	580	16°	4.4	B	1.1	111.0

For nanosecond pulses, plasma formation has been observed to occur in aqueous media when the irradiance in the focal spot is in the range of 10^8-10^{10} W/mm^2. The high temperature and pressure associated with the plasma leads to its rapid expansion, thereby compressing the surrounding medium and leading to the emission of a shock wave. The plasma expansion results in cooling, resulting in electron-ion recombination and the formation of a cavitation bubble that expands and collapses on a microsecond timescale [127, 129]. The cavitation bubble size is strongly dependent on laser pulse energy. Because plasma formation is driven by a critical irradiance intensity (power/area) as opposed to a critical radiant exposure (energy/unit area), plasmas can be formed using much smaller laser pulse energies when picosecond laser pulses are used. It has been shown that the pulse energy to produce plasma formation can be reduced 50-fold if the laser pulse duration is reduced from 5 ns to ~50 picoseconds [1, 134, 136]. Therefore, picosecond pulses may provide cell lysis that is much more spatially precise, thus enabling more subtle perturbations such as cell microsurgery and optoinjection. Because the requirement for pulse energy is dramatically reduced, rapid advances in laser development makes it likely that pulse energies available from affordable,

compact, commercially available lasers may be sufficient to produce cell lysis in the near future [52, 147, 148].

2.4   Impact of Wavelength on Optical Breakdown

As discussed in Section 2.2, the initiation of plasma formation requires the generation of a free electron through multiphoton absorption. The band gap energy for water is 6.5 eV, corresponding to a photon with wavelength $\lambda = 190$ nm. Nd:YAG lasers in our laboratory are capable of emitting pulses at three wavelengths: the 1064 nm fundamental wavelength, the second harmonic at 532 nm, and the third harmonic at 355 nm. The photon energies at wavelengths of 1064 nm, 532 nm, and 355 nm are 1.17 eV, 2.34 eV, and 3.51 eV, respectively. Therefore, multiphoton absorption requires the energy from simultaneous absorption of six, three, and two photons, respectively, to overcome the band gap energy of 6.5 eV. As a result, laser pulses at shorter wavelengths can initiate optical breakdown at smaller pulse energies.

We have chosen to use 532 nm wavelength for our studies for several reasons. First, the laser technology at 532 nm is robust, mature, and relatively inexpensive. Second, this visible wavelength makes alignment relatively easy, compared to wavelengths in the IR and UV. Furthermore, microscope optics are optimized for visible wavelength and visible wavelength optics are both economical and readily available. Lastly, at 532 nm there are no endogenous absorbers to provide deposition of laser energy, minimizing the potential of damage outside of the focal volume.

Chapter 3

PULSED LASER MICROBEAM-INDUCED CELL LYSIS

USING 6 NS PULSES

3.1   Abstract

In this chapter, we study the physical interaction of 6 ns pulses with cell monolayers as a function of pulse energy and cell surface density[1].   Lysis was accomplished through the delivery of 6 ns, $\lambda = 532$ nm laser pulses via a 40x, 0.8 NA microscope objective to a location 10 μm above confluent monolayers of PtK_2 cells. The process dynamics were examined at cell surface densities of 600 and 1000 cells/mm^2 and pulse energies corresponding to 0.7x, 1x, 2x, and 3x the threshold for plasma formation.   The cell lysis process was imaged at times of 0.5 ns $-$ 50 μs following laser pulse delivery and revealed the processes of plasma formation, pressure wave propagation, and cavitation bubble dynamics.   Cavitation bubble expansion was the primary agent of cell lysis with the zone of lysed cells fully established within

---

[1] Portions of this chapter have appeared in *Biophysical Journal*, reference 94.   Rau K, Quinto-Su P, Hellman A, Venugopalan V: Pulsed laser microbeam-induced cell lysis: Time-resolved imaging and analysis of hydrodynamic effects. *Biophysical Journal* 91:317-329, 2006.

600 ns of laser pulse delivery. The spatial extent of cell lysis increased with pulse energy but decreased with cell surface density. Hydrodynamic analysis indicated that cells subject to transient shear stresses in excess of a critical value were lysed while cells exposed to lower shear stresses remained adherent and viable. This critical shear stress is independent of laser pulse energy and varied from 60 - 85 kPa for cell monolayers cultured at a density of 600 cells/mm^2 to 180 - 220 kPa for a surface density of 1000 cells/mm^2. The implications for single cell lysis and microsurgery are discussed.

3.2   Introduction

In this chapter, we will examine the physical mechanisms of laser microbeam-induced cell lysis as a function of pulse energy using 6 ns pulses. As discussed in Chapter 2, laser-induced plasma formation is the process that mediates many laser-microbeam-cell interactions. Examination of the dynamics of laser induced plasma formation can be difficult because the spatial and temporal scales involved span several orders of magnitude. To overcome these challenges, the Venugopalan group at the University of California, Irvine has developed a time-resolved imaging system with ~1 µm spatial resolution and 0.5 ns temporal resolution to study laser microbeam-induced cell lysis in adherent cells [93]. This system provides a detailed visualization of the cellular injury process, including plasma formation, shock wave propagation, and cavitation bubble formation, expansion, and collapse. Previous studies in our laboratory revealed cavitation bubble expansion as the principal contributor to cell lysis and the maximum cavitation bubble size to be much larger than the zone of cell lysis [93]. This is an important and unexpected result since it had long been thought that cavitation

bubble collapse was the principal mechanism for mechanical damage produced by laser-induced plasma formation [135]. This initial study provided the first exposition of the sequence of events produced by pulsed laser microbeam cell lysis and identified cavitation bubble expansion as the primary agent of the damage process. However, these observations were not supported with substantial modeling or analysis to establish relationships between the laser parameters and cavitation bubble characteristics to the spatial extent of cellular damage.

In this chapter, we will support these observations through the visualization and measurement of both the dynamics of the cell lysis process and the spatial extent of resulting cellular injury at four pulse energies corresponding to 0.7x, 1x, 2x, and 3x the threshold for plasma formation. These dynamics have been measured when focusing the laser pulses at high numerical apertures at a 10 μm distance of above fully confluent PtK$_2$ cell cultures with cell surface densities of 600 and 1000 cells/mm^2. Furthermore, we present a hydrodynamic model to predict the dynamic shear stresses experienced by adherent cells due to the displacement of fluid produced by the cavitation bubble expansion. The model provides estimates of the time-resolved shear stresses experienced by adherent cells as a function of both radial position and time following delivery the laser pulse.

3.3   Materials and Methods

3.3.1   Cell Irradiation

An inverted microscope (Zeiss Axiovert S100, Jena, Germany) was used as the experimental platform. A Q-switched, frequency-doubled Nd:YAG laser (INDI 20,

Spectra Physics, Mountain View, CA) emitting 6 ns duration pulses at $\lambda = 532$ nm was used for cell irradiation. As shown in Figure 3.1 the laser output was split into two beam lines using a $\lambda/2$ plate and polarization sensitive beam splitter. The beam line formed by the reflection off the beam splitter was used for image illumination as described in Section 3.3.2 below. The beam that passed through the beam splitter was expanded and re-collimated using a 5x beam expander, followed by an iris to select the central portion of the laser beam. The beam emerging from the iris was introduced into the microscope epifluorescence port and reflected upward into the rear entrance aperture of the objective by a dichroic mirror placed in the microscope filter cube. The laser pulse energy was adjusted by rotating a linear polarizer inserted into the beam path. The laser pulse energy entering the rear entrance aperture of the objective was measured by removing the objective from the microscope turret and allowing the unobstructed beam to illuminate an energy detector (J3-05, Molectron Inc., Santa Clara, CA) set on the microscope stage. Pulse-to-pulse energy variation was found to be $\pm 3\%$. A brightfield objective (40x, 0.8 NA, Zeiss Achroplan) was used for cell irradiation and visualization. Unless stated otherwise, the focal plane of the pulsed laser microbeam was positioned at a separation distance of $s = 10$ μm above the cell monolayer.
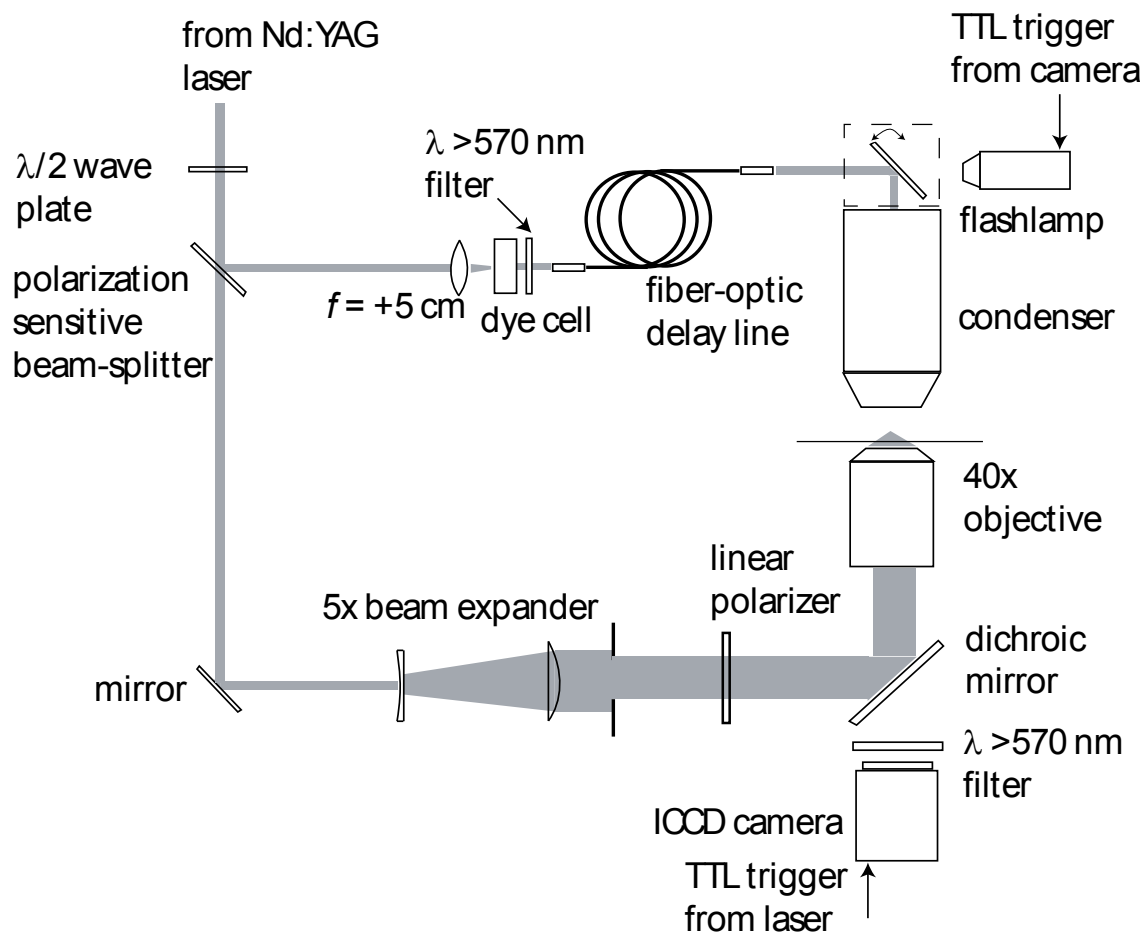
Figure 3.1: Schematic of laser-microscope setup for cell lysis and time-resolved imaging.

3.3.2 Time-Resolved Imaging System

As depicted in Figure 3.1, illumination for the time-resolved images was provided by delivering a short light pulse at the desired time delay following the arrival of the Nd:YAG laser pulse at the sample. At time delays shorter than 1.2 μs, illumination was provided by the fluorescence emission of a dye cell that was pumped by the beam line formed by the portion of the Nd:YAG laser beam that is reflected by the polarization sensitive beam splitter. The dye fluorescence (LDS 698, Exciton Inc., Dayton, OH) was

coupled into a 600-μm-diameter multimode optical fiber (UMT 600, 0.39 NA, Thor Labs, Newton, NJ) with the fiber output being directed into the microscope condenser. Optical fibers of different length were used to provide the desired time delay between delivery of the pulsed laser microbeam to the target and the image illumination. The fluorescence emission from the dye cell provided illumination at $\lambda = 698 \pm 20$ nm with full width at half maximum (FWHM) duration of 15 ns. The broad spectral width of the fluorescence emission provided images free from speckle artifact. At longer time delays, illumination was provided by an ultrashort duration flash lamp (Nanolite KL-L, High-Speed Photo Systeme, Wedel, Germany) that was electronically triggered from the camera. The flash lamp emission provided a broad spectral output ($\lambda = 400 - 700$ nm) with a FWHM duration of 40ns.

Images were acquired using a gated intensified CCD camera (PI-MAX, Roper Scientific, Trenton, NJ) that was triggered by a TTL pulse from the laser Q-switch. The camera operation and image acquisition was performed using WinView32 imaging software (Princeton Instruments, Trenton, NJ). The camera gate duration was set to 0.5 ns when using the fluorescent dye cell for illumination and to 200 ns when using flash lamp illumination due to electronic jitter in the flash lamp triggering. Thus for time delays shorter than 1.2 μs the exposure duration was governed by the 0.5 ns camera gate width, while at longer time delays the exposure duration was governed by the 40 ns duration of the flash lamp. A long pass filter (LP 570, Edmund Optics, Barrington, NJ) was used to prevent scattered laser radiation from reaching the camera. This system allowed us to irradiate and image the sample at time delays of 0.5 ns to 50 μs required to capture the full dynamics of the process.

3.3.3 PtK$_2$ Cell Culture

Potorous rad kidney epithelial (PtK$_2$) cells were grown in polystyrene culture dishes with glass bottoms (P35G-1.5-7-C, MatTek Corp., Ashland, MA) in minimum essential medium (MEM, Gibco, Carlsbad, CA) supplemented with 10% fetal calf serum, L-glutamine, essential amino acids, sodium pyruvate, penicillin and streptomycin. The culture medium was prepared free of phenol red to ensure its transparency to $\lambda = 532$ nm radiation. Culture dishes with cells at 100% confluency were used in each experiment. These cells did not exhibit contact inhibition and thus the surface density of cells (cells/mm^2) was measured and controlled. The results below are provided for cell monolayers cultured at surface densities of 600 and 1000 cells/mm^2. Cell surface densities were determined by counting the number of cells in a square 0.5 mm x 0.5 mm region centered at the site of cell lysis. For a given cell surface density, the site-to-site variation was kept below 10%.

3.4 Results

3.4.1 Plasma Threshold Measurement

Prior to conducting the cell lysis experiments, we determined the threshold for plasma formation in our experimental system. This was achieved by delivering a Nd:YAG laser pulse via the 40x, 0.8 NA brightfield objective into a Petri dish filled with culture medium. Plasma formation in the culture medium was observed visually in a dark room and its incidence for 50 pulses at discrete pulse energies was recorded. The probability of plasma formation p as a function of pulse energy E_p for each pulse duration was fit to a Gaussian error function in the form:

$$p(E_p) = 0.5[1 + \text{erf} \, [S(E_p + E_{th})]],$$ (3.1)

where S is the 'sharpness' of the error function and E_{th} is the threshold for plasma formation defined as the pulse energy that results in a 50% probability of plasma formation. This equation describes accurately the stochastic nature of the plasma formation process [132]. The result of one such experiment along with the model fit are shown in Figure 3.2. Using the setup described earlier in this chapter resulted in a plasma threshold value of $8.0 \pm 0.3 \, \mu\text{J}$.
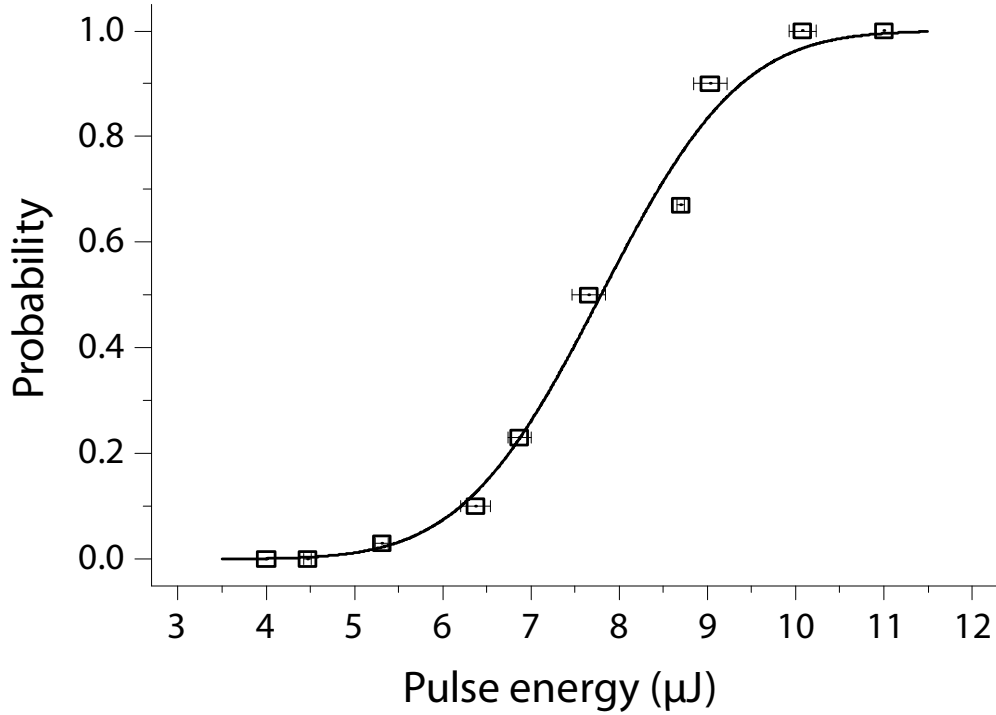
Figure 3.2: Probability of plasma incidence as a function of laser pulse energy with Gaussian error function fit.

Earlier experiments by Venugopalan and co-workers that delivered 6 ns pulses from a Q sw Nd:YAG laser via a 0.9 NA objective into an open cuvette filled with

distilled water yielded a breakdown threshold of 1.9 μJ [126]. These experiments were performed using a externally-seeded laser whose output beam possessed a M^2 beam propagation factor of ~1.4 (personal communication, Alfred Vogel, Institute of Biomedical Optics, University of Luebeck, Germany). This resulted in a threshold irradiance (I_{th}) of 7.8 x 10^{10} W/cm^2, when assuming a diffraction limited spot size for a 0.9 NA objective at λ = 532 nm. While our system employs a microscope objective with slightly lower numerical aperture and the coverslip on which the cells are plated introduces some optical aberrations [93], we believe the higher thresholds measured on the microscope setup described here are primarily due to the poor spatial beam quality of the Q-sw Nd:YAG laser. Q-sw Nd:YAG lasers with a Gaussian coupled resonator typically produce output beams that are multi-mode in nature ($M^2 > 2$) and prevents us from achieving diffraction-limited spot sizes in the focal plane [21]. As a result higher pulse energies are required to achieve the irradiances necessary for optical breakdown. In our system, we have a measured plasma threshold of 8 μJ. An assumed threshold irradiance of I_{th} = 7.8 x 10^{10} W/cm^2 [126] implies that the laser beam radius in the focal plane is 0.738 μm for λ = 532 nm. This exceeds by nearly a factor of two the diffraction limited spot size of 0.405 μm for a 0.8 NA objective. To further confirm that our threshold values were not due to a system error we performed these measurements using an identical objective on a second laser-microscope system that utilized a Q-sw Continuum Surelite Nd:YAG laser [56, 61] and obtained similar values for the plasma threshold.

3.4.2   Time-Resolved Imaging

Figure 3.3 is a series of time-resolved images of the cell lysis process in a culture with surface density of 1000 cells/mm^2 produced at a pulse energy of 24 μJ corresponding to 3x the plasma threshold. Our image series follows the well-known evolution of an optical breakdown process starting with plasma formation, followed by shock wave propagation and finally cavitation bubble formation, expansion, and collapse [129]. The plasma initiation, growth, and decay were complete within 25 – 30 ns after the arrival of the laser pulse. Close examination of Figure 3.3 (a) reveals the formation of a shock wave resulting from the rapid plasma expansion. The shock wave propagation was followed until it passed outside the field of view [Figure 3.3 (a) - (e)]. Although the pressure amplitudes are considerable, approaching 480 MPa close to the irradiation site [93], the passage of the shock wave did not produce any visible disruption of the cell monolayer.
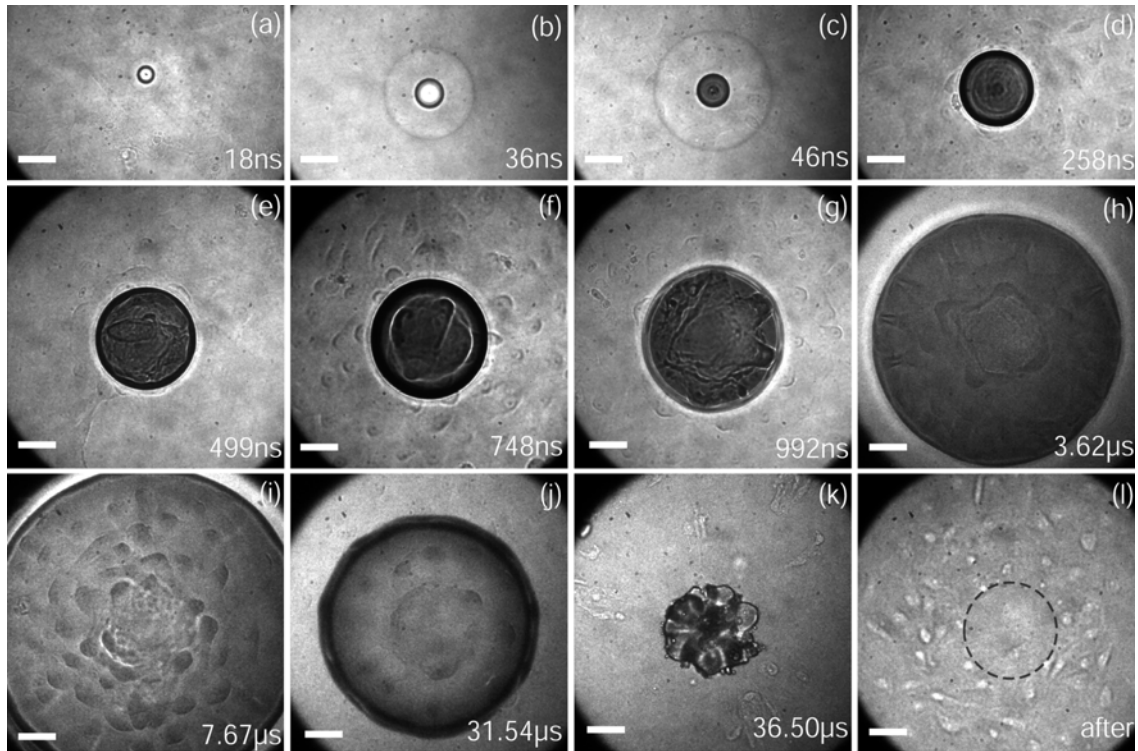
Figure 3.3: Time-resolved image series of the cell lysis process with cell surface density of 1000 cells/mm^2 at a pulse energy corresponding to 3x the threshold for plasma formation. Plasma formation, shock wave propagation, cavitation bubble dynamics, and development of the injury process are all clearly seen. Image times are as marked. Panel *l* is a phase contrast image and shows the cell sample post irradiation. Scale bar = 50 μm.

The plasma expansion resulted in cooling and ion-recombination leading to the formation of a cavitation bubble within 40 ns following the laser pulse. The outer portions of the bubble appear dark due to the oblique angle of incidence of the illumination on the bubble surface that prevented transillumination. Figure 3.3 (c)-(i) reveal that cavitation bubble expansion is the primary mechanism of cell lysis and several interesting features of this process can be seen in these images. At early times (35 – 200 ns) during the expansion of the cavitation bubble, cell injury is clearly visible within the central region of the bubble [Figure 3.3 (d)-(e)]. During this early expansion

phase, cells that lie outside the bubble are lysed immediately upon arrival of the bubble wall. However, at some time point, (approximately 200 ns at 3x plasma threshold for a surface density of 1000 cells/mm^2), arrival of the bubble wall does not result in additional cell lysis. Rather, further bubble expansion encompasses the cells without lysing them [Figure 3.3 (h)]. Another interesting feature is the transient deformation of the cells produced by the bubble expansion, evident in regions both inside and outside the bubble [Figure 3.3 (g)-(i)]. Remarkably, these cells appear to withstand this severe deformation without gross disruption. After reaching its maximum size, the bubble collapses quite rapidly, within 1 - 2 μs as seen in Figure 3.3 (j). Figure 3.3 (k) shows the break up of the bubble upon collapse. Close examination reveals that the cells surrounding the site of bubble collapse are deformed in a direction away from the center of the bubble. This may indicate the presence of radial fluid flow away from the center of the bubble collapse. The bubble collapse did not extend the zone of cell lysis but did clear any cellular debris present within the lysis zone. As a result, the lysis process results in a well-defined area around the irradiation site that is cleared of both cells and cellular debris [Figure 3.3 (l)] that we define as the zone of cellular injury.

To examine if the distance between the focal volume of the pulsed laser microbeam and the cell monolayer would affect the dynamics of the cell lysis process, we performed time-resolved imaging with a separation distance $s = 400$ μm, as opposed to $s = 10$ μm, between the focal plane of the laser microbeam and the cell monolayer. Figure 3.4 shows the results of one such experiment at a pulse energy of 24 μJ corresponding to 3x threshold. Figure 3.4 (a), taken 14.4 μs following the laser pulse delivery shows clearly that while bubble expansion produces significant cell

deformation it does not produce cell lysis. However in Figure 3.4 (b) and (c), taken at delay times of 29.4 µs and 32.4 µs, respectively, we see that cavitation bubble collapse, jet formation, and subsequent radial outflow of fluid results in the lysis of cells in the central region. Moreover, in Figure 3.4 (c) cell lysis can be observed in regions outside the collapsing bubble due presumably to mechanical effects produced by the hydrodynamics associated with bubble collapse and jet formation.
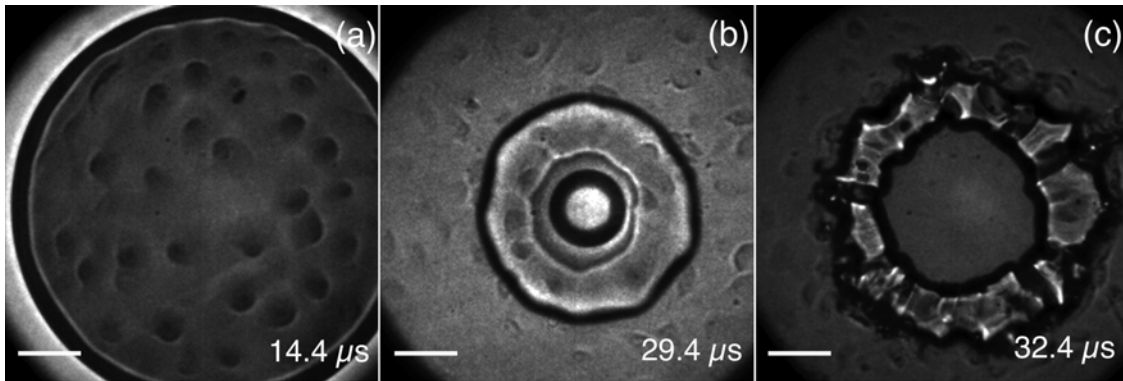
Figure 3.4: Cell lysis produced by cavitation bubble formation at distances equal to 400 µm above a cell monolayer with a surface density of 1000 cells/mm^2. (a) Image of an expanding cavitation bubble at 14.4 µs showing deformed, but intact, cells below the bubble. Images of bubble collapse at (b) 29.4 µs and (c) 32.4 µs, respectively, show cell lysis due to jet formation and radial outflow. The central region below the bubble has been cleared of cells. In panel c, cell lysis can also be observed outside the bubble. Scale bar = 50 µm.

3.4.3 Cavitation Bubble Dynamics

The temporal evolution of the cavitation bubble size was measured from a sequence of time-resolved images and shown in Figure 3.5 for pulse energies corresponding to 0.7x, 1x, 2x, and 3x the threshold for plasma formation. A minimum of three images were used to calculate the average and standard deviation for each data

point shown.   It is important to note that the cavitation bubble dynamics are not influenced by the cell surface density.
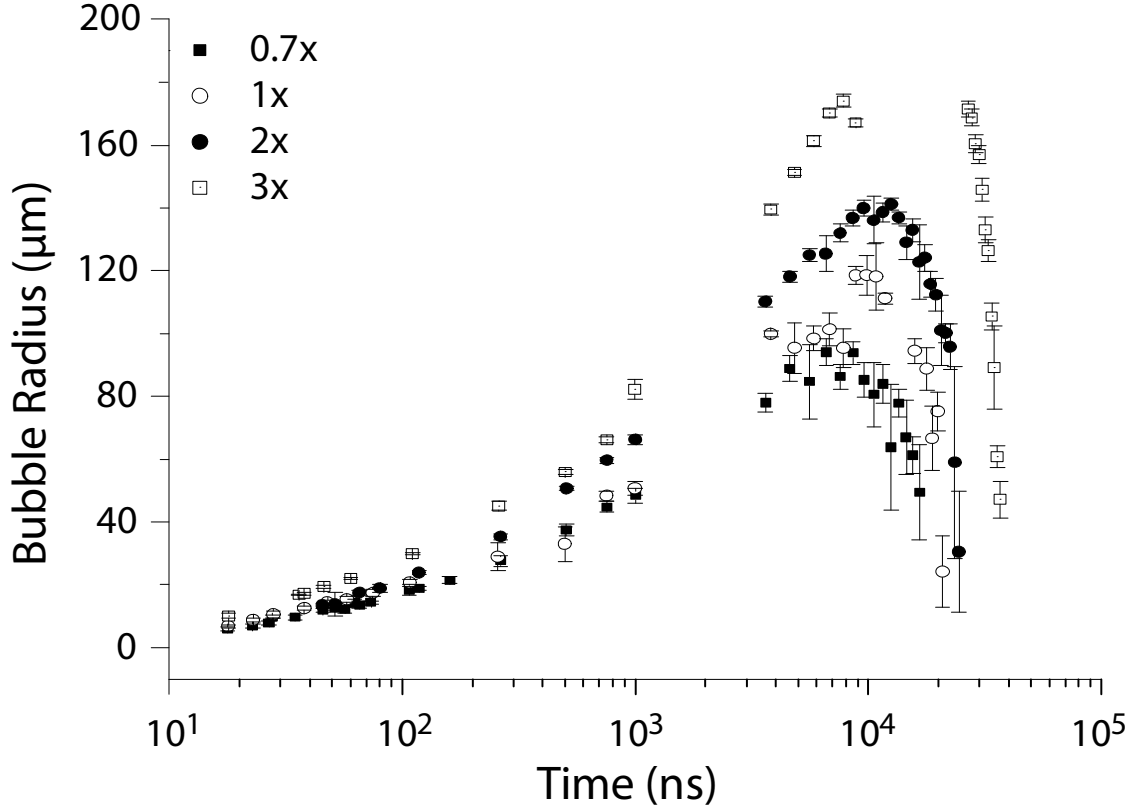
Figure 3.5: Cavitation bubble dynamics for pulse energies corresponding to 0.7x, 1x, 2x, and 3x the threshold for plasma formation. Each data point represents the average of three images.

The values for maximum bubble radius R_{max} and bubble oscillation time T_{osc} are of particular interest and are presented in Table 3.1. This case of inertially-controlled bubble growth was considered by Lord Rayleigh who derived the following expression relating the maximum cavitation bubble radius to the collapse time T_{col} as [18]:

$$R_{max} = \frac{T_{col}}{0.915}\left[\frac{(p_\infty - p_v)}{\rho}\right]^{1/2}$$

(3.2)

where ρ is the density of the liquid (1000 kg/m^3), p_∞ is the static pressure of the surrounding liquid, and p_v is the vapor pressure of the liquid (2330 Pa at 20°C). Our experimentally obtained values for R_{max} and T_{col} ($T_{col} = T_{osc}/2$) are consistent with the Rayleigh equation listed above. The energy of a hemispherical bubble E_B is given by:

$$E_B = \frac{2}{3}\pi \ (p_\infty - p_v)R_{max}^3 \tag{3.3}$$

Substitution of Eq. 3.2 into Eq. 3.3 allows the bubble energy to be expressed in terms of the cavitation bubble parameters as:

$$E_B = \frac{2}{3}\pi\rho \left(\frac{0.915}{T_{col}}\right)^2 R_{max}^5 \tag{3.4}$$

The bubble energy calculated using Eq. 3.4, as well as the percentage of the laser pulse energy transduced into bubble energy [(E_B/E_p) x 100], are also presented in Table 3.1.

Table 3.1: Laser pulse energy (E_p), maximum cavitation bubble radius (R_{max}), oscillation time (T_{osc}), mechanical bubble energy (E_B), mechanical transduction efficiency (E_B/E_P), and radius of cell lysis (R_{lys}) for cultures with a cell surface density of 1000 cells/mm^2 and 600 cells/mm^2 when using energies corresponding to 0.7x, 1x, 2x, and 3x the threshold for plasma formation.

	E_p [μJ]	R_{max} [μm]	T_{osc} [μs]	E_B [μJ]	E_B/E_p [%]	R_{lys}^{1000} [μm]	R_{lys}^{600} [μm]
0.7 x Threshold	5.6	95	17	0.18	3.2	19 ± 3	29 ± 2
1 x Threshold	8	118	21	0.34	4.3	23 ± 4	40 ± 4
2 x Threshold	16	140	25	0.57	3.6	30 ± 4	45 ± 5
3 x Threshold	24	200	37	1.66	6.9	36 ± 2	63 ± 6

The radial position of the bubble wall during the initial cavitation bubble expansion was fit to the function $R_B(t) = [a + (b/\ln t)]^2$ with $R_B(t)$ being the bubble radius as a function of time and a and b being the fit parameters. This analytic expression was found to fit all the data series with regression coefficients > 0.99 (Table Curve, Systat Software, Richmond, CA). An example of the raw data and curve fit for pulse energies of 5.6 and 24 μJ (0.7x and 3x threshold) is shown in Figure 3.6 (a) over the time interval of 0 - 10 μs.
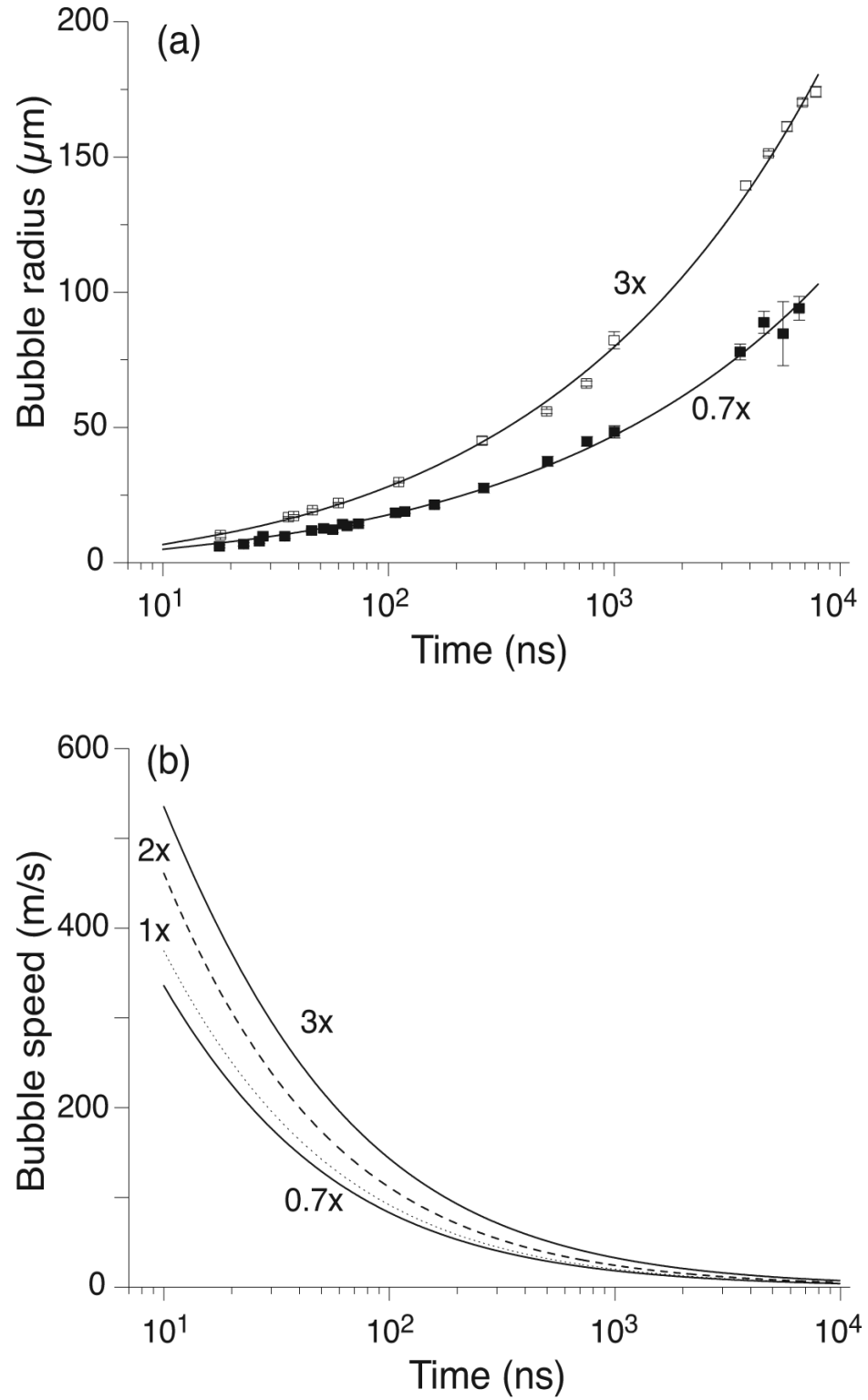
Figure 3.6: (a) Bubble expansion for 0.7x and 3x threshold pulse energy with curve fit. (b) Bubble velocities for pulse energies corresponding to 0.7x, 1x, 2x, and 3x the threshold for plasma formation as derived from curve fits.

The cavitation bubble expansion velocity, as determined by differentiation of the analytic curve fits, are shown for all pulse energies in Figure 3.6 (b). It is seen that the maximum bubble expansion velocities increased with the laser pulse energy. While the bubble expansion velocities are initially high, ranging between 320 – 510 m/s, they rapidly decrease to 18 - 32 m/s at 1 μs. The zone of cellular injury shown in

Figure 3.3 (l) is defined by the region around the irradiation site that was denuded of cells. We determined the average size of the injury zone by measuring the radius of the cellular injury zones produced at 8-10 irradiation sites. In some instances the zone of cell lysis was elliptical and the radius of a circle of equivalent area was used instead. These results revealed that although the cavitation bubble dynamics are not affected by the cell surface density in the cell culture, the size of the resulting zone of cell lysis is. The radial size of cellular injury as a function of pulse energy is shown in Table 3.1 for cell surface densities of 600 and 1000 cells/mm^2. For both cell surface densities, the zone of cellular injury was much smaller than the maximum cavitation bubble size. Specifically, cell cultures with a surface density of 600 cells/mm^2 had lysis zones that were consistently larger than cultures of 1000 cells/mm^2 with average radii of 29, 40, 45, and 63 μm for 0.7x, 1x, 2x, and 3x threshold, respectively. The corresponding maximum cavitation bubble radii at these pulse energies were 80, 120, 140, and 200 μm.

3.4.4 Hydrodynamic Modeling: Velocity and Shear Stress Distributions Produced by Bubble Expansion

The time-resolved images provide compelling evidence for the hypothesis that when the pulsed laser microbeam is focused immediately above the cell monolayer ($s = 10$ μm), the primary agent for cell lysis and deformation is the dynamic shear stress produced by the fluid displacement associated with cavitation bubble expansion. To analyze these hydrodynamics we consider the model problem depicted in Figure 3.7. We assume that the cell monolayer acts as a boundary and that the cells are subject to shear stress due to movement of fluid parallel to this boundary.
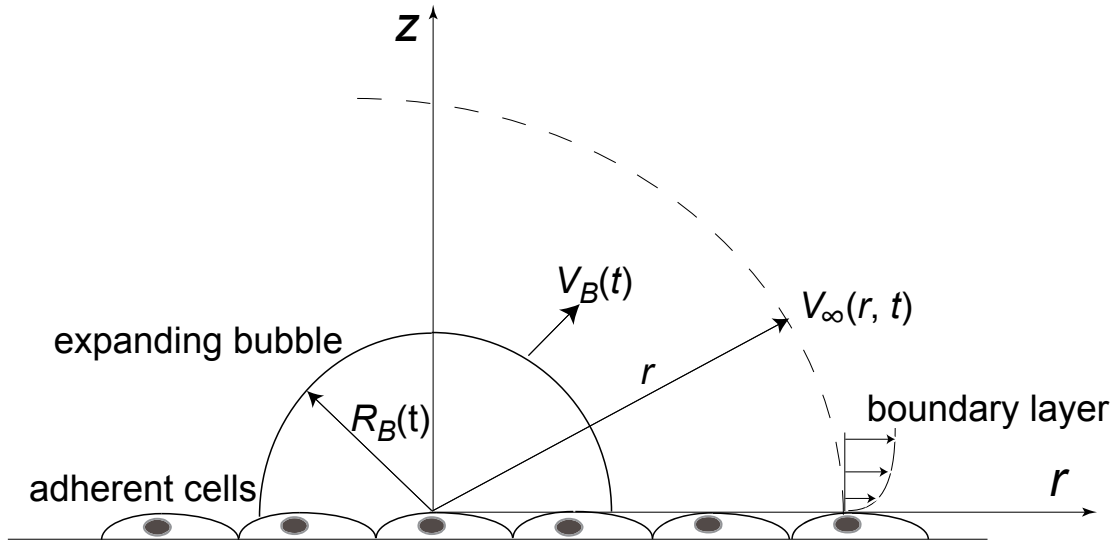
Figure 3.7: Schematic of model problem for hydrodynamic analysis.

We consider the fluid motion at locations outside the expanding bubble and define a geometry in which the origin is located at the site of the laser focus immediately above the cell monolayer with z and r being the vertical and radial axes, respectively. The transient external fluid velocity V_∞ produced by the cavitation bubble

expansion is determined by applying conservation of mass for an incompressible fluid in spherical coordinates as:

$$V_\infty(r,t) = V_B(t)\left[\frac{R_B(t)}{r}\right]^2 \tag{3.5}$$

where $R_B(t)$ and $V_B(t)$ are the time varying position and velocity of the hemispherical bubble wall, respectively. Thus by using experimental data for both $R_B(t)$ and $V_B(t)$, samples of which were shown in Figure 3.6 (b), we can obtain $V_\infty(r,t)$ at any desired radial location prior to the arrival of the bubble wall.

Of course, Eq. 3.5 is valid only at locations sufficiently removed from the boundary presented by the cell monolayer (and underlying glass coverslip) because the standard `no-slip' boundary applies at the boundary ($z = 0$). This results in the formation of a thin fluid layer proximal to the cell monolayer in which the fluid velocity varies as a function of both z and t. To examine the velocity distribution within this boundary layer, we first consider the results of Stokes' first problem for 1-D planar impulsive flow with a constant external velocity V_∞ [100]. This translates to a boundary layer problem with the initial condition $V_\infty(z, t \leq 0) = 0$ and boundary conditions $V(z = 0, t) = 0$ and $V(z \to \infty, t) = V_\infty$. The solution to this problem is given by [100]:

$$V(z,t) = V_\infty erf\left(\frac{z}{2\sqrt{vt}}\right), \tag{3.6}$$

where $erf(x)$ is the error function defined earlier in connection with Eq. (3.1) and v is the kinematic viscosity of the culture medium ($0.896 \times 10^{-6} m^2/s$).

In contrast to Stokes' first problem where V_∞ is constant in both space and time, in our problem V_∞ varies with both radial position and time, that is, $V_\infty = V_\infty(r,t)$.

Moreover, we have boundary layer flow in a spherical rather a 1-D planar geometry. This latter issue regarding boundary layer curvature can be ignored so long as we consider radial positions much larger than the boundary layer thickness i.e. $r \gg \delta$. The case of a external velocity that varies with both space and time changes the boundary condition at $z \to \infty$ to $V(r, z \to \infty, t) = V_\infty(r,t)$. For this case, the velocity distribution in the boundary layer can be determined by temporally convolving the result of Stokes' first problem given by Eq. (3.6) with the temporal variation of $V_\infty(r,t)$ given by the experimental data via Eq. (3.5). This approach to constructing the solution to a problem possessing a boundary condition that varies with both space and time from the response of the system to a step function is known as Duhamel's integral [29]. This situation has been considered previously by several investigators including Lokhandwalla and Sturtevant who provide the result [69]:

$$V(r,z,t) = \int_0^t \frac{\partial V_\infty(r,t')}{\partial t'} erf\left[\frac{z}{2\sqrt{v(t-t')}}\right] dt' . \qquad (3.7)$$

From Eq. (3.7), the wall shear stress experienced by the cells $\tau_w (r, z = 0, t)$ can be obtained at any radial position r for the time interval $0 \leq t \leq t^*$, where t^* is the time of arrival of the bubble wall at position r using:

$$\tau_w(r,t) = \rho v \left(\frac{\partial V}{\partial t}\right)\bigg|_{z=0} = \rho \sqrt{\frac{v}{\pi}} \int_0^t \frac{\partial V_\infty(r,t')}{\partial t'} \frac{dt'}{\sqrt{t-t'}} \qquad (3.8)$$

where ρ is the density of the culture medium (1000 kg/m^3). Equations (3.7) and (3.8) provide a complete description of the velocity field and wall shear stress at any location prior to the arrival of the bubble wall. It is important to realize that the predictions

given by these equations result simply from the application of the conservation of mass and momentum to the experimental data and contain no adjustable parameters.

Given the availability of these modeling results, we are interested in examining possible correlations between the characteristics of the fluid field and the resulting zone of cell lysis. The natural place to look are the velocity profiles and wall shear stresses experienced at the radial positions corresponding to the edge of the injury zone $r = R_{\text{lys}}$ at the time of arrival of the cavitation bubble wall t^*. Figure 3.8 presents velocity profiles within the boundary layer at the time of arrival of the bubble wall at the radial location corresponding to the edge of the zone of cellular injury for pulse energies corresponding to 0.7x, 1x, 2x, and 3x threshold within a cell culture with surface density of 1000 cells/mm^2 i.e., $V(r = R_{\text{lys}}, z, t = t^*)$. The distance at which the fluid velocity is equal to 99% of the external fluid velocity is known as the boundary layer thickness and for the cases shown in Figure 3.8, ranges from 1.04 - 1.25 μm. A summary of hydrodynamic data and model results data are summarized in Table 3.2 for cell densities of 1000 and 600 cells/mm^2. Due to only small differences in bubble velocities for 0.7x and 1x threshold (see Figure 3.6 b) the boundary layer velocity profile for both is also fairly similar with the external fluid velocity being slightly less for 1x threshold at $r = R_{\text{lys}}$. This is due to the larger value of $R_{\text{lys}} = 23$ μm at 1x threshold vs. 19 μm for 0.7x threshold.
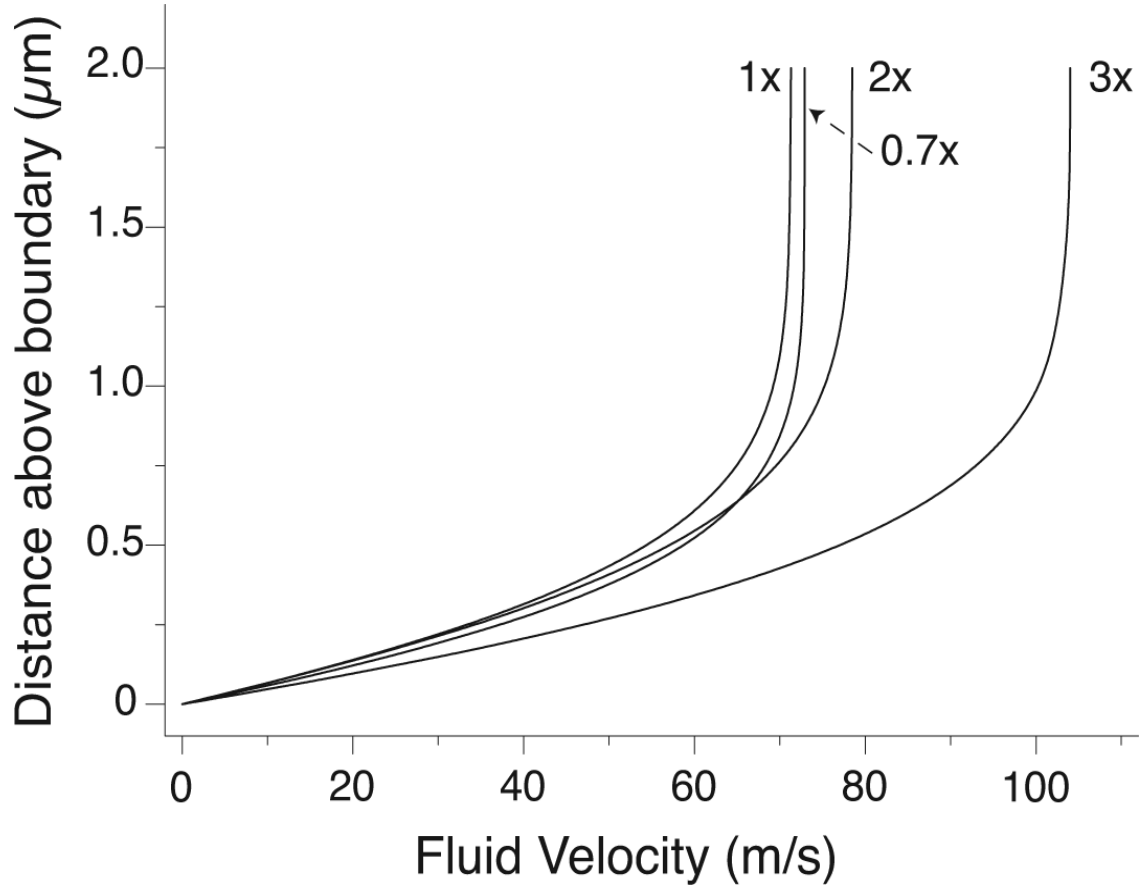
Figure 3.8: Velocity profile as a function of distance above the cell monolayer at $r = R_{lys}$ of 19, 23, 30, and 36 μm for pulse energies corresponding to 0.7x, 1x, 2x, and 3x the threshold for plasma formation, respectively.

Table 3.2: Summary of hydrodynamic data and analysis providing the radius of cell lysis (R_{lys}), bubble arrival time at R_{lys} (t^*), the external fluid velocity (V_∞) and boundary layer thickness (δ) at $r = R_{lys}$ and $t = t^*$, and the peak wall shear stress $\tau_{w, peak}$ for pulse energies corresponding to 0.7 x, 1x, 2x, and 3x the threshold for plasma formation.

Cell density [#/mm^2]	E_p [µJ]	Zone of cell lysis R_{lys} [µm]	Bubble arrival time t^* [ns]	External fluid velocity $V_\infty(R_{lys}, t^*)$ [m/s]	Boundary layer thickness $\delta(R_{lys}, t^*)$ [µm]	Peak wall shear stress $\tau_{w, peak}$ [kPa]
		Experimental Data		**Model Predictions**		
1000	5.6	19 ± 3	115	73	1.04	189 ± 61
	8	23 ± 4	139	71	1.16	180 ± 64
	16	30 ± 4	159	79	1.25	198 ± 54
	24	36 ± 2	164	104	1.23	219 ± 24
600	5.6	29 ± 2	303	40	1.74	81 ± 13
	8	40 ± 4	513	31	2.30	60 ± 14
	16	45 ± 5	418	44	2.08	84 ± 23
	24	63 ± 6	568	47	2.38	72 ± 16

In Figure 3.9 we provide the temporal profile of the wall shear stress $\tau_w(t)$ at different radial positions for a pulse energies corresponding to 1x and 2x the threshold for plasma formation. The temporal shape of the shear stress is similar regardless of location; that is, the peak shear stress is reached after a relatively rapid rise followed by a more gradual decline. The time intervals over which the shear stress is provided increases with radial position and simply reflects the longer time necessary for the bubble front to arrive at that location, after which time the model provides no prediction. As expected, the peak shear stress decreases with increasing radial position.
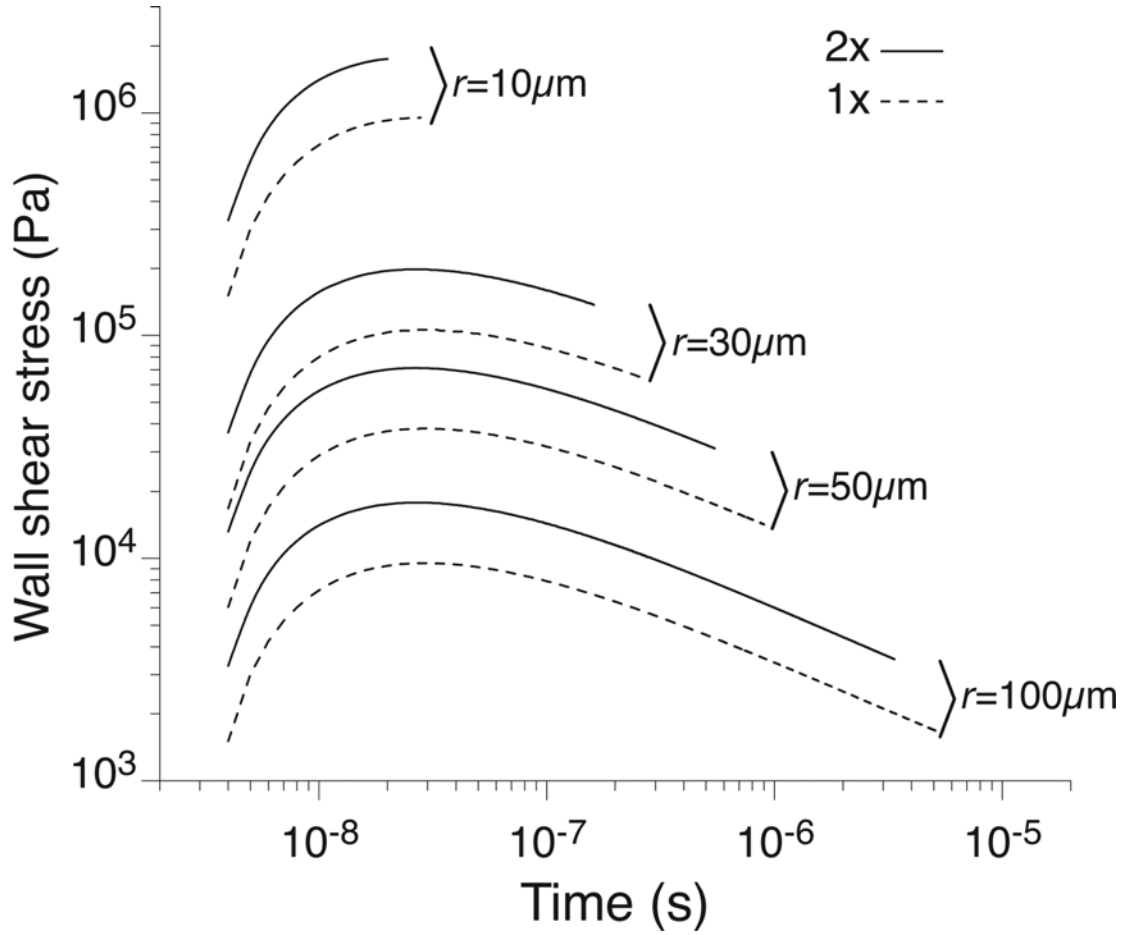
Figure 3.9: Temporal shear stress profile as a function of radial position at 1x and 2x threshold. The shear stress is calculated until the time of arrival of the bubble rim at that radial position.

In Figure 3.10 (a) and (b) we plot the wall shear stress as a function of time at the radial location demarcating the zone of cell lysis $\tau_w(r = R_{lys}, t)$ for pulse energies corresponding to 0.7x, 1x, 2x, and 3x threshold for cell surface density of 1000 and 600 cells/mm^2, respectively. For a given cell density, the similarity of the temporal profiles of the wall shear stress at R_{lys} is truly remarkable especially given the more than 4-fold variation in laser pulse energy. Moreover, the peak wall shear stress necessary to cause lysis does not appear to vary systematically with the laser pulse energy.

Specifically, the peak wall shear stress at the rim of the zone of cell lysis ($r = R_{lys}$) lies in a narrow range of 180 - 220 kPa for a cell density of 1000 cells/mm^2 [Figure 3.10 (a)], and 60 - 84 kPa for a cell density of 600 cells/mm^2 [Figure 3.10 (b)]. Thus the minimum peak shear stress necessary to cause lysis for the cell density of 1000 cells/mm^2 is approximately 3x higher compared to 600 cells/mm^2.
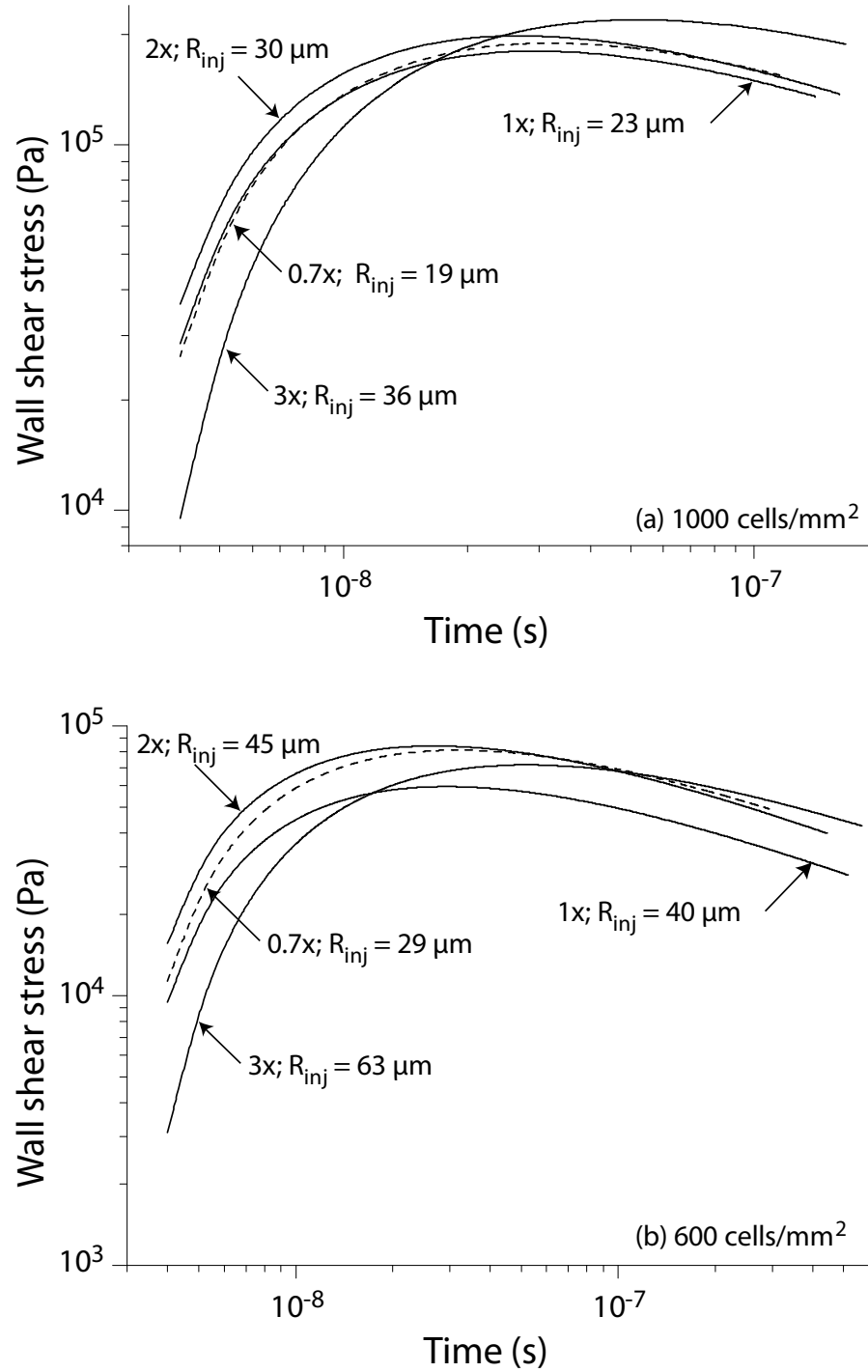
Figure 3.10: (a) Temporal profiles of the wall shear stress at $r = R_{lys}$ of 19, 23, 30, and 36 μm corresponding to irradiation at pulse energies of 0.7x, 1x, 2x, and 3x the threshold for plasma formation, respectively, for a cell surface density of 1000 cells/mm^2. (b) Temporal profiles of the wall shear stress at $r = R_{lys}$ of 29, 40, 45, and 63 μm corresponding to irradiation at 0.7x, 1x, 2x, and 3x the threshold for plasma formation, respectively, for a cell surface density of 600 cells/mm^2.

The above hydrodynamic analysis of our experimental results strongly supports the hypothesis that for a specific cell surface density the spatial extent of cellular injury is determined by the maximum shear stress produced by the cavitation bubble expansion. To aid in examining this hypothesis for both cell surface densities examined, we provide in Figure 3.11 the spatial distribution of the peak shear stress generated by the cavitation bubble expansion at pulse energies corresponding to 0.7x, 1x, 2x, and 3x threshold. Note that the shear stress predictions are based on the experimental measurements of the cavitation bubble dynamics $R_B(t)$ that are known to greater precision than the measured experimental variation in R_{lys}. As a result, the uncertainty in the peak shear stress experienced by the cells is dictated by the observed variation in the radial size of the zone of cell lysis R_{lys} rather than the uncertainties inherent in the measurement of the bubble dynamics $R_B(t)$. Given the steep variation in the peak shear stress with radial location, a small uncertainty in the measurement of R_{lys} leads to a rather large uncertainty in the peak shear stress. This is shown in Table 3.2 where the zones of cellular injury for each cell surface density is listed along with the peak wall shear stress as a function of pulse energy. We also present the corresponding external fluid velocity $V_\infty(r = R_{lys}, t = t^*)$ and boundary layer thickness δ at the edge of the zone of cell injury at the time of bubble arrival.
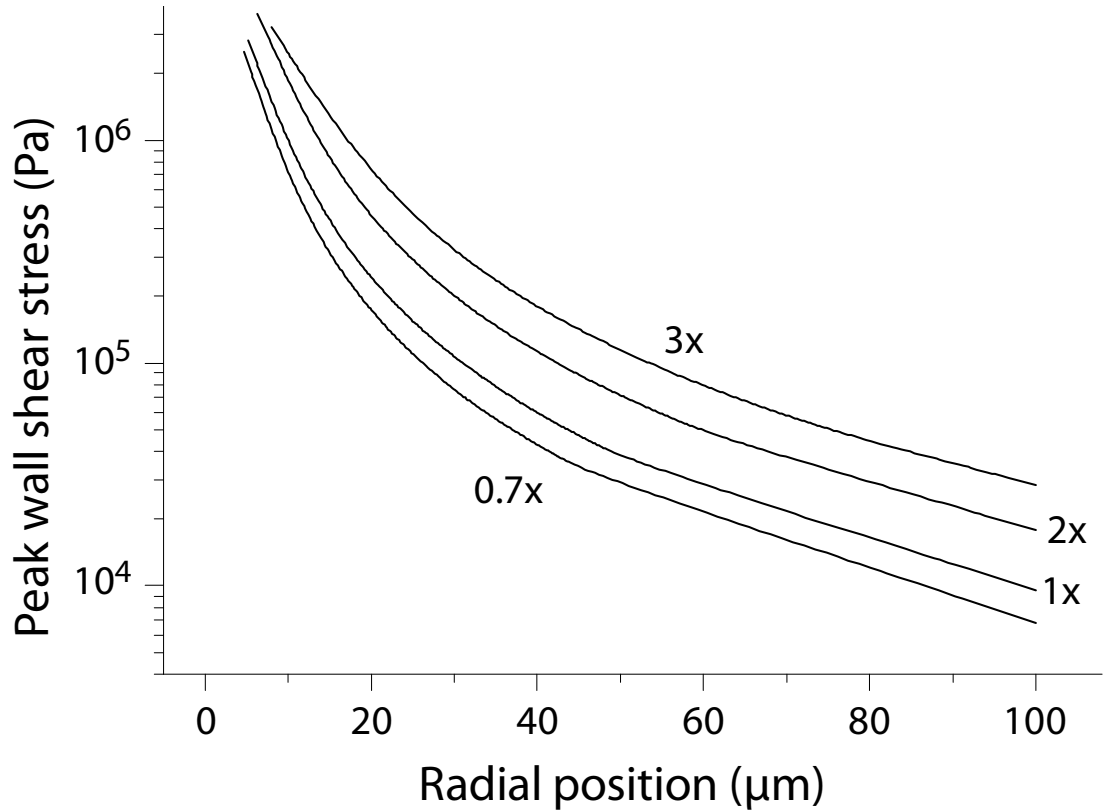
Figure 3.11: Peak wall shear stress $\tau_{w,max}$ as a function of radial position at pulse energies 0.7x, 1x, 2x, and 3x the threshold for plasma formation.

3.5 Discussion

3.5.1 Role of Plasma Formation and Shock Wave Propagation on Cell Injury

Time-resolved imaging provides a precise means to visualize and quantify the effects of optical breakdown on adherent cells. Our microscope setup provides an image resolution of ~1 μm while the ICCD camera provides a maximum temporal resolution of 0.5 ns. This combination of high spatial and temporal resolutions enables accurate, high-speed imaging of the cell lysis process. The plasma is visible at the earliest time point of 0.5 ns and its evolution could be followed until the plasma luminescence ceased (35 – 40 ns). While the high temperature plasma and its explosive

expansion can cause cell vaporization, we could not visualize this process due to the plasma luminescence. The plasma expansion results in the radiation of a shock wave with pressure amplitudes approaching 480 MPa [93]. However, no cellular injury resulting from the shock wave propagation through the cell layer is observed and highlights the ability of these cells to withstand shock. This finding is consistent with other studies that found no evidence of cellular injury by laser-induced pressure waves alone [108, 135].

3.5.2 Role of Cavitation Bubble Expansion and Shear Stress on Cell Injury

Time-resolved imaging provides evidence that the fluid flow resulting from cavitation bubble expansion is the primary agent of cellular injury. Cell lysis is initiated at the site of plasma formation and propagates outwards with the bubble expansion. We can infer that cavitation bubble expansion produces cell membrane disruption and cell lysis rather than merely cell detachment due to the fact that cellular debris was consistently observed proximal to the irradiation site and intact cells were never observed to be floating in the culture medium following laser pulse delivery. Previous work by the Allbritton group has also shown that laser-induced plasma formation with pulse energies similar to those used here cause cell membrane disruption [73, 104].

The production of laser-induced breakdown at a separation distance $s = 10$ μm above the cell monolayer led to cavitation bubble formation whose proximity to the monolayer enhanced the damage potential of the resulting hydrodynamic flow. Cell lysis occurred rapidly and the zone of cell lysis was fully developed within 200 ns for 1000 cells/mm^2 and within 600 ns for 600 cells/mm^2 at 3x threshold pulse energy.

Thereafter bubble expansion did not result in cell lysis. The bubble velocity as determined from the time-resolved images revealed velocities in the range of 320 – 510 m/s at early times that rapidly decreased to 31 – 104 m/s at the edge of the injury zone as shown in Figure 3.6 (b) and Table 3.2. Adherent cells at the border of the zone of cell lysis remained intact but underwent significant transient deformation from the large shear stresses associated with the cavitation bubble dynamics. Thus, depending on the location of the cell, the shear stresses could either cause lysis or, for larger radial locations, transient deformation of the cell body.

These results are consistent with those of Wolfrum and co-workers who examined the effect of pressure wave excited contrast agent bubbles on rat kidney fibroblast cell [142]. Using time-resolved imaging, the authors observed that under the action of pressure waves, contrast agent bubbles in the vicinity of cells expanded from a diameter of 2 μm to 62 μm within 3 μs. While the bubbles did not cause cell lysis during expansion they were observed to produce transient deformation of the cells. Cell lysis or rupture was only observed upon bubble collapse. The characteristic bubble expansion velocities (< 10 m/s; determined from Figure 2 of Wolfrum) and bubble diameters (< 60 μm) were significantly smaller than those produced in our study. These factors limited the damage potential of the bubble expansion in the Wolfrum study.

Our hydrodynamic model provides a means to determine the spatio-temporal evolution of both the fluid velocity and wall shear stress. This enables a correlation between the observed cellular effects and the fluid flow characteristics. We assume that the bubble-cell interactions were mediated by a thin fluid layer between the expanding

bubble and the cell monolayer at all times [14, 28]. This assumption is borne out by the fact that even cells that were encompassed by the bubble [Figure 3.3 (h)] underwent significant deformation, a result only possible due to the presence of a thin fluid layer between the bubble and cells. It was also seen that regardless of the laser pulse energy, PtK$_2$ cells cultured at a surface density of 1000 cells/mm^2, remained adherent even when subject to transient wall shear stresses approaching $180 - 220$ kPa while those cultured at a surface density of 600 cells/mm^2 only withstood transient wall shear stresses approaching $60 - 84$ kPa. The fact that this range of wall shear stress does not vary systematically with laser pulse energy but with cell surface density suggests the presence of a critical wall shear stress for cell lysis on the nanosecond time-scale. Moreover, the finding that the critical shear stress increases with increasing cell surface density suggests that the higher cell surface density may promote changes in cell-cell or cell-substratum interactions that provide for greater mechanical resilience [15, 23, 97].

In addition, we observed that adherent cells had the ability to withstand large shear stresses without visible damage. Even though the peak wall shear stress experienced by cells at $r = 100$ μm were much lower than those on the border of the lysis zone, they were still in the 7 - 28 kPa range (Figure 3.11). Visual examination of the cells surrounding the lysis zone 24 hours post irradiation revealed their continued viability and proliferation. Recent work modeling fluid flow during hemolysis of red blood cells in suspension when exposed to shock wave lithotripsy revealed that cells can withstand high spatial velocity gradients if exposures were limited to nanosecond time scales [69]. Our imaging results and hydrodynamic analysis show that interactions between laser-generated cavitation bubbles and adherent cells are governed by similar

considerations with cells capable of sustaining large shear stresses over short time exposures. It is possible that these high shear stresses cause other physiological changes within cells including transient membrane permeabilization [44], spikes in Ca^{2+} signaling [48, 107], detachment of focal adhesion sites, disruption of cytoskeleton, activation of biochemical pathways etc. Investigation of such changes using fluorescence assays is currently underway and will be discussed in Chapters 4, 5, and 6.

3.5.3 Role of Bubble Collapse on Cell Injury

We found no significant contribution of the bubble collapse to cellular injury when focusing the pulsed laser microbeam at a separation distance of $s = 10$ μm above the cell monolayer. This is an interesting observation since cavitation bubble collapse is a well-known damage mechanism ranging from the pitting of ship propellers and vacuum pumps to the breakup of kidney stones in shock wave lithotripsy [18, 96]. In an extensive study examining the mechanisms of intraocular surgery using Nd:YAG laser pulses, Vogel and co-workers studied several different irradiation geometries, all using relatively low numerical apertures, to determine the specific contributions of plasma formation and cavitation bubble dynamics to the injury process [135]. For cases where the laser was focused above an *ex-vivo* sample of corneal tissue (an irradiation geometry similar to our experiments), it was shown that for a constant laser pulse energy the extent of damage was dependent upon the parameter γ, defined as the ratio between the separation distance s and the maximum cavitation bubble radius R_{max}. In these cases, images taken after the laser-tissue interaction revealed the corneal surface to be

punctured with a region surrounding the puncture site denuded of corneal endothelial cells. This latter feature is similar to the zone of cell lysis observed in our study.

Vogel and co-workers implicated the impact of a liquid jet during cavitation bubble collapse as the cause for puncture of the corneal endothelium and stroma while the region of denuded cells was attributed to the radial outflow of the jet following impact [135]. This is in contrast with our results obtained at a separation distance s = 10 µm that clearly demonstrate cell lysis to occur during the cavitation bubble expansion and not during the bubble collapse. In the Vogel study, the smallest value of γ (= s/R_{max}) tested was 0.15. Due to the large pulse energies and low focusing angles used, this small γ value was accomplished with a 100 µm separation distance between the focal plane of the laser beam and the tissue boundary. This significant distance from the surface of the cells reduces both the fluid velocity and the shear stress to which the cells are exposed upon the cavitation bubble expansion. Moreover this greater distance allows for coherent and focused jet formation upon bubble collapse.

By contrast, in our experiments the site of plasma formation was 10 µm above the cell monolayer. This not only results in smaller values of γ = 0.06 - 0.13 but also exposes the cells to the maximal effects of the shear stresses produced by the rapid bubble expansion resulting in cell lysis. Once the cells were lysed, nothing viable remained in the central region that would be susceptible to the jet impact and radial outflow produced upon bubble collapse. Moreover, the small γ value results in the production of a hemispherical bubble and results in a bubble collapse and break up that likely reduces the effects of liquid jet impact [131].

Of related importance are studies of shock wave lithotripsy that have shown bubble collapse to be the mechanism of cell injury. A time-resolved study by Ohl and Wolfrum on the effects of shock-wave excited cavitation bubbles on adherent cells demonstrated that bubble collapse caused cell detachment and membrane permeabilization [81]. Bubble sizes and collapse times in the Ohl study are comparable to those produced by irradiation at 3x threshold in our study. However, since bubble generation in the Ohl study is shock wave induced, the time and location of bubble formation could not be controlled. This may have led to the production of fewer bubbles in the immediate proximity of the cells thereby reducing their exposure to the hydrodynamic effects during bubble expansion and increasing cell survival.

Taken together, the results of these earlier studies and our findings provide strong evidence that the site of bubble generation is a critical factor determining whether cell injury occurs during the expansion or collapse phase of the cavitation bubble dynamics. Our studies of optical breakdown produced at larger separation distances from the boundary confirm this. Plasma formation at a pulse energy 3x plasma threshold using a separation distance of $s = 400$ μm resulted in $\gamma = 1.6$. In this case the fluid flow generated during bubble expansion produced cell deformation but not cell lysis [Figure 3.4 (a)]. Instead, the asymmetric bubble collapse produced a coherent jet directed towards the cells that concentrated energy away from the bubble. Cell lysis resulted from the jet impact and subsequent radial outflow of the fluid jet [Figure 3.4 (b) and (c)]. These experiments resulted in zones of cell injury significantly larger than those produced by the bubble expansion when smaller γ values were used. This increased damage zone is most similar to the conditions used in studies of

intraocular laser surgery and shock wave lithotripsy induced injury, described by both Vogel and Ohl [81, 135].

3.5.4 Effect of Pulse Energy on Cell Injury

The delivery of sub-threshold pulse energies also allowed the investigation of the potential use of low energy pulses for single cell lysis. Our results show that both bubble size and bubble energy are reduced significantly when using sub-threshold pulse energies. As shown in Table 3.1, a 30% reduction in pulse energy from 1x to 0.7x threshold results in a 20% reduction in bubble size and a 50% reduction in bubble energy. For the cultures with a surface density of 1000 cells/mm^2 this resulted in the lysis of only 2 - 3 cells. It should be noted that our use of a multimode laser beam resulted in higher plasma threshold energies than in cases where laser beams of better spatial quality were used [126]. Reductions in plasma threshold energy can also be accomplished using a multimode beam in conjunction with a spatial filter [47], microscope objectives with higher numerical aperture, or shorter laser pulse durations. The use of laser parameters that result in lower plasma threshold energies will provide for further increases in precision by accomplishing further reductions in both the plasma and bubble energies.

These results are also suggestive of the injury mechanism during cell microsurgery wherein intra-cellular organelles are irradiated with sub-threshold ns laser pulses focused through a 1.3 NA objective [53, 55, 56]. In these cases, the laser is operated at a 10 - 20 Hz repetition rate and the cell is typically exposed to tens to thousands of pulses. This procedure produces intracellular injury, even in the absence

of an endogenous absorption, without compromising cell survival. We believe that laser-induced breakdown provides a viable mechanism for injury in these cases. At sub-threshold pulse energies, plasma formation may only be induced by a small fraction of the delivered laser pulses. Also, when formed, the plasma energy density would be extremely low and result in a minimal transduction of incident laser pulse energy into bubble energy. Thus the bubble size would be small and the injury may be confined to the volume of the plasma itself thus providing for higher rates of cell survival.

3.6   Conclusion

Cell lysis produced by Q-sw pulsed laser microbeam irradiation at $\lambda = 532$ nm in cell monolayers cultured at densities of 600 and 1000 cells/mm^2 was investigated using time-resolved imaging and hydrodynamic analysis with pulse energies of 5.6 - 24 μJ. The well known sequence of plasma formation, shock wave propagation, and cavitation bubble formation, expansion and collapse was observed with high temporal and spatial resolution. Cavitation bubble expansion rather than bubble collapse was seen to be the primary agent of cell lysis when the pulsed laser microbeam was focused at a separation distance of $s = 10$ μm above the cell monolayer. The lysis process is extremely rapid, reaching completion within 200 and 600 ns at the highest pulse energy tested for cell monolayers with surface densities of 1000 and 600 cells/mm^2, respectively. Maximum bubble sizes were significantly larger than the cell injury zones indicating that as the bubble expansion slowed, the associated wall shear stresses were not sufficient to cause lysis. Images also revealed the ability of cells to remain adherent after being subject to strong transient deformation. We also confirmed that production

of cavitation bubbles at separation distances of $s = 400$ μm above the cell monolayer results in larger zones of cell injury that are produced upon cavitation bubble collapse and not expansion. Thus, with the proper selection of the laser microbeam pulse energy and focal volume location, it is possible to precisely control both the extent and temporal evolution of cellular injury.

Hydrodynamic analysis based on the measured time evolution of the cavitation bubble growth revealed that the time-resolved wall shear stress at a particular radial position increased rapidly to a maximum value followed by a more gentle decay. This analysis revealed that cell monolayers cultured at surface densities of 1000 cells/mm^2 can withstand transient shear stresses of 180 - 220 kPa without damage or detachment while peak shear stresses are in the range of 7 - 28 kPa at 100 μm from the site of irradiation. Cell lysis zones in monolayers cultured at a surface density of 600 cells/mm^2 were substantially larger and these cells were found capable of withstanding peak shear stresses of only 60 − 84 kPa. This finding suggests that reductions in the cell surface density may result in changes in cell-cell or cell-substratum interactions that make them more susceptible to lysis by the laser-generated shear stresses.

3.7   Acknowledgements

Chapter 4

CELLULAR RESPONSE TO PULSED LASER MICROBEAM

INDUCED CELL LYSIS AND MOLECULAR DELIVERY

4.1   Abstract

Cell lysis and molecular delivery in confluent monolayers of PtK_2 cells are achieved by the delivery of 6 ns, $\lambda = 532$ nm laser pulses via a 40x, 0.8 NA microscope objective[2]. With increasing distance from the point of laser focus we find regions of (a) immediate cell lysis, (b) necrotic cells that detach during the fluorescence assays, (c) permeabilized cells sufficient to facilitate the uptake of small (3 kDa) FITC-conjugated Dextran molecules in viable cells, and (d) unaffected, viable cells. The spatial extent of cell lysis, cell detachment, and molecular delivery increased with laser pulse energy. Hydrodynamic analysis from time-resolved imaging studies reveal that the maximum wall shear stress associated with the laser microbeam-induced cavitation

---

bubble expansion governs the location and spatial extent of each of these regions independent of laser pulse energy. Specifically, cells exposed to maximum wall shear stresses $\tau_{w,max} > 190 \pm 20$ kPa are immediately lysed while cells exposed to $\tau_{w,max} > 18 \pm 2$ kPa are necrotic and subsequently detach. Cells exposed to $\tau_{w,max}$ in the range of 8-18 kPa are viable and successfully optoporated with 3 kDa Dextran molecules. Cells exposed to $\tau_{w,max} < 8 \pm 1$ kPa remain viable without molecular delivery. These findings provide the first direct correlation between laser microbeam-induced shear stresses and subsequent cellular outcome.

4.2   Introduction

In the previous chapter, we provided a detailed characterization of the physical interaction of 6 ns laser microbeam pulses with cells. However, it is important to relate these physical effects to the cellular biological response. In this chapter, we determine the biological effects resulting from laser induced cellular injury and connect these effects with the physics of the laser microbeam irradiation process. An understanding of this interrelationship between the physical processes of pulsed laser microbeam irradiation and the biological response may enable the optimization of the laser parameters used in these procedures and motivate the development of new applications that utilize laser microbeams.

Here we provide a detailed examination of the biophysical effects resulting from pulsed laser microbeam irradiation of a confluent cell monolayer. This irradiation results in laser-induced plasma formation, shock wave propagation and cavitation

bubble formation, expansion and collapse. These phenomena collectively produce the observed cellular effect. Of particular interest is a hydrodynamic analysis of the cavitation bubble expansion that reveals the effects of fluid shear stress on cell lysis, viability, and transient membrane permeabilization (molecular delivery). In the previous chapter, time-resolved imaging verified that the cavitation bubble expansion is the primary agent of cell lysis when using nanosecond laser microbeams focused at a location 10 μm above the cell monolayer [93, 94]. Cell lysis is initiated at the site of plasma formation and propagates outwards with the bubble expansion [94]. A hydrodynamic model revealed that for cell monolayers cultured at surface densities of 1000 cells/mm^2, cell lysis occurred only at locations where transient shear stresses $\tau_{w,max} > 190 \pm 20$ kPa, independent of the laser pulse energy. Cells exposed to lower transient shear stresses remained intact and appeared viable even though they were subject to severe transient deformation during the cavitation bubble dynamics.

Here we investigate the biological response to the delivery of a single pulsed laser microbeam by assessing the cell viability and membrane permeabilization surrounding the site of irradiation as a function of laser microbeam pulse energy. We examine the biophysical implication of these results using quantitative data obtained from time-resolved imaging of the laser microbeam irradiation process and hydrodynamic analysis introduced in Chapter 3.

4.3   Materials and Methods

4.3.1   Cell Irradiation

An inverted microscope (Axiovert S100, Zeiss, Jena, Germany) was used as the experiment platform.   A Q-switched, frequency-doubled Nd:YAG laser (INDI 20, Spectra Physics, Mountain View, CA) emitting 6 ns pulses at $\lambda = 532$ nm was used for cell irradiation.   As shown in Figure 4.1 the laser output was directed through a $\lambda/2$ plate and polarization-sensitive beam splitter, followed by a linear polarizer to adjust the laser pulse energy.   The central portion of the laser beam was selected using an iris, directed into the rear microscope port, and reflected upward into the rear entrance aperture of the objective by a dichroic mirror placed in the microscope filter cube.   The laser pulse energy entering the rear entrance aperture of the objective was measured by removing the objective from the microscope turret and allowing the unobstructed beam to illuminate an energy detector (Model No. J5-09, Coherent, Santa Clara, CA) set on the microscope stage.   Pulse-to-pulse energy variation was found to be $\pm 3\%$. A bright-field objective [16] was used for cell irradiation.   The focal plane of the pulsed laser microbeam was positioned at a separation distance of 10 μm above the cell monolayer.
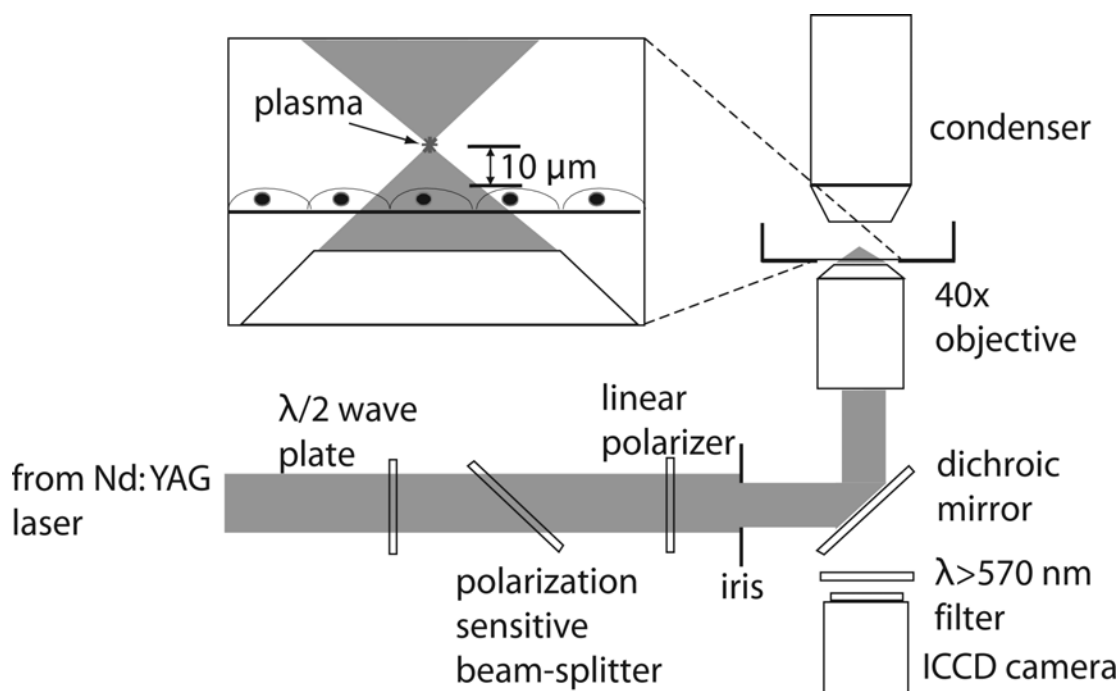
Figure 4.1: Schematic of laser-microscope setup for cell irradiation.

4.3.2 Fluorescence Imaging

A Quantix CCD camera (Photometrics, Roper Scientific, Trenton, NJ) was used for the fluorescence and phase contrast imaging, with 20x, 0.45 NA Phase 2 (Zeiss A Plan, Jena, Germany) and 10x, 0.3 NA Phase 1 (Zeiss Plan-NEOFLUAR, Jena, Germany) objectives. Camera operation and image acquisition was performed using V++ imaging software (Photometrics, Roper Scientific, Trenton, NJ). Image intensity levels were adjusted and images were compiled using Adobe Photoshop 7.0 (Adobe, San Jose, CA).

4.3.3 PtK$_2$ Cell culture

Potorous rat kidney epithelial (PtK$_2$) cells were grown in polystyrene culture dishes with glass bottoms (P35G-0-14-C, MatTek, Ashland, MA) in advanced

minimum essential medium (Advanced MEM, Invitrogen, Carlsbad, CA) supplemented in 1% fetal calf serum, L-glutamine, amphomycin, and gentamicin sulfate. The culture medium was prepared free of phenol red to ensure its transparency to λ = 532 nm radiation. Cells were cultured in a humidified incubator with a constant temperature of $37^{o}C$ and a CO_2 level of 5%. Culture dishes with cells at 100% confluency were used in each experiment. These cells did not exhibit contact inhibition and the surface density (cells/mm^2) was measured and controlled. The results provided are for cell monolayers cultured at a surface density of 1000 cells/mm^2. The cell surface density was determined by counting the number of cells in a square 0.5 mm x 0.5 mm region centered at the site of cell lysis. The site-to-site variation in cell surface density was kept below 10%.

4.3.4   Cell Viability Assay

Cell viability was assessed using Calcein AM (Invitrogen, Carlsbad, CA), a membrane permeant dye that readily passes through the cell membrane of viable cells and is hydrolyzed by esterases to form Calcein which remains inside the cell. Dead cells were identified by Propidium Iodide (Invitrogen, Carlsbad, CA), a DNA intercalating agent that stains the nuclei of dead cells. Cell culture dishes were incubated 30 minutes after laser irradiation and loaded with 2 μM Calcein AM and 5 μg/mL Propidium Iodide by incubation for 20 min. To remove the remaining dyes, cells were washed carefully with medium three times before imaging.

3.1.1   Molecular delivery Assay

Prior to laser irradiation, cells were placed in a 500 µM solution of Fluorescein isothiocyanate (FITC) conjugated dextran (Sigma, MW = 3 kDa). Cells were lysed and incubated for 30 minutes at 37°C, and a 5 µg/mL solution of Propidium Iodide (PI) was added. Cells were incubated for 20 minutes and washed with buffer three times before imaging.

4.4   Results

4.4.1   Plasma Threshold, Cell Viability, and Molecular Delivery

As stated in the previous chapter, the threshold energy for plasma formation in our experimental system is 8 µJ [94]. This was verified by delivering an Nd:YAG laser pulse via the 40x, 0.8 NA bright-field objective into a Petri dish filled with culture medium. Plasma formation in the culture medium was observed visually in a dark room and its incidence for 50 pulses at discrete pulse energies was recorded. The threshold for plasma formation is defined as the pulse energy that results in a 50% probability of plasma formation.

Cell cultures were irradiated with a single laser pulse at energies of 8, 16, 24, and 40 μJ, corresponding to 1x, 2x, 3x, and 5x the threshold energy for plasma formation. A minimum of 10 sites for each pulse energy were examined using fluorescence assays. The extent of cellular damage was confirmed by performing a standard live-dead fluorescence assay using Calecin AM and Propidium Iodide on the cell cultures after irradiation. Immediately after lysis, the irradiation sites were visualized using phase contrast imaging. In addition, we imaged the irradiation sites under both phase contrast and epifluorescence after the cell assays were carried out. In performing the cell assays, we observed that many cells surrounding the lysis zone that remained adherent immediately after laser microbeam irradiation detached and were flushed away during the wash process (Figure 4.2).
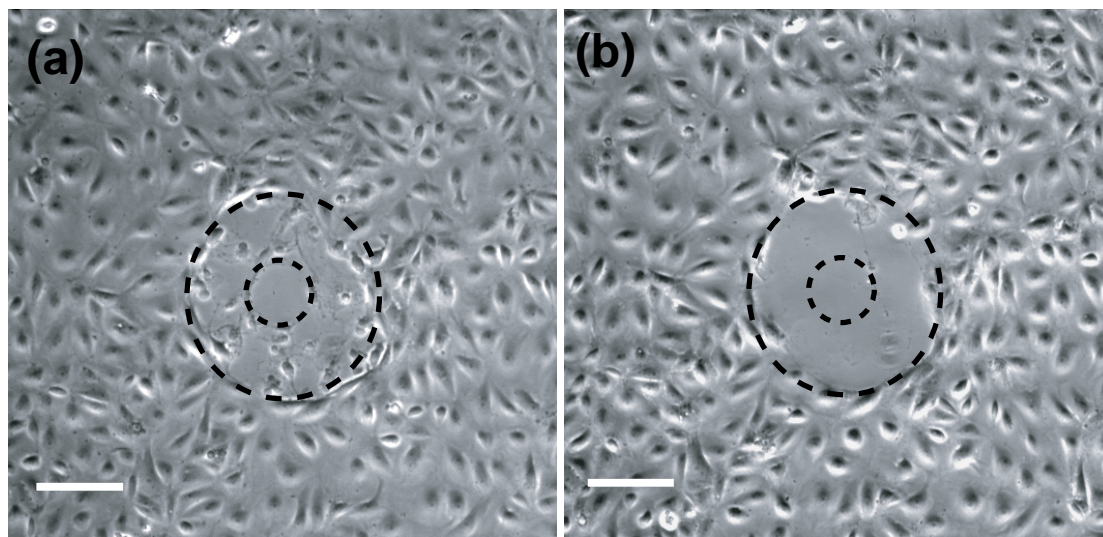
Figure 4.2: Phase contrast images of cells following irradiation by a 16 μJ pulse. Images were taken (a) immediately after lysis and (b) after the viability assay incubation and wash process. Scale bar = 100 μm.

Figure 4.3 provides phase contrast and fluorescence images of cells after viability staining for sites irradiated at pulse energies corresponding to 1x, 2x, 3x, and 5x the threshold energy for plasma formation, respectively. The majority of cells that remain attached after the fluorescence assay survive the laser irradiation, as seen by the presence of very few dead cells around laser irradiation site. Outside this region, the cells remain adherent and viable. The area cleared of cells increases with pulse energy. These cells were followed 24 hours post-irradiation to confirm their continued viability, proliferation, and migration to fill in the void areas created by the cell lysis event.
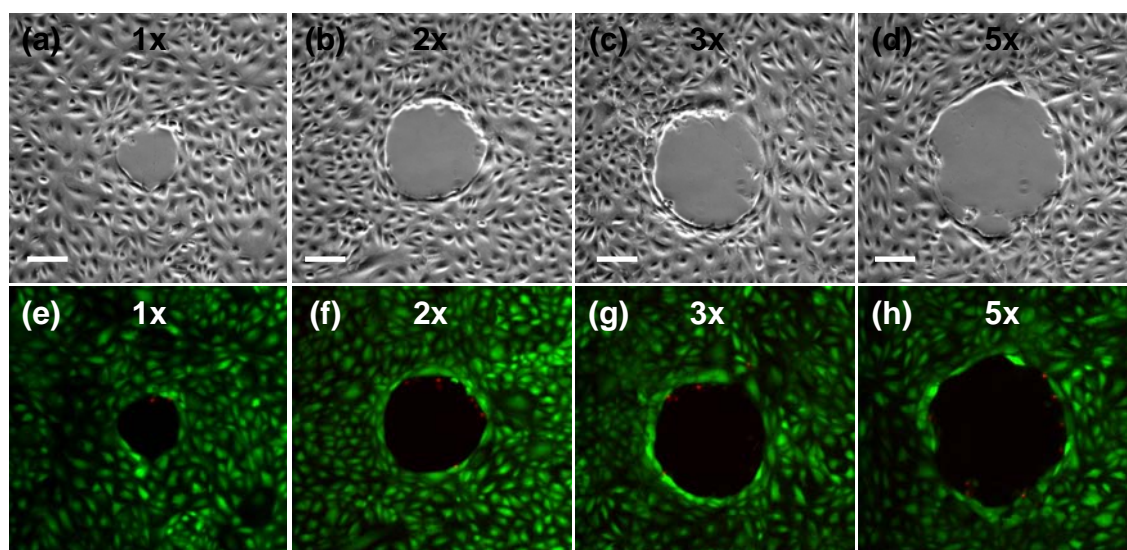
Figure 4.3: Cell viability assay after irradiation at energies corresponding to 1x (a,e), 2x (b,f), 3x (c, g) and 5x (d, h) the threshold energy for plasma formation: (a-d) phase contrast images showing the irradiation site and zone of cellular damage, (e-h) fluorescent images with Calcein AM (green) showing viable cells and propidium iodide (red) staining the nuclei of dead cells around the periphery of the irradiation site. Scale bar = 100 μm.

After confirmation that the vast majority of the adherent cells surrounding the irradiation site remain viable, we sought to assess the potential of using pulsed laser microbeam irradiation for molecular delivery. PtK$_2$ cell cultures were placed in a solution of FITC-conjugated Dextran (MW = 3 kDa) and exposed to a single 6 ns pulse from the Nd:YAG laser delivered via the 40x, 0.8 NA bright-field objective. The cells were washed with buffer and dead cells were identified by incubation with Propidium Iodide. Figure 4.4 shows phase contrast and fluorescent images demonstrating molecular uptake of Dextran after irradiation at all four laser microbeam energies examined. Three zones of cells were identified following molecular delivery. The first region is characterized by necrotic cells that detached during the viability assay. This resulted in only a few remaining adherent cells that showed staining with Propidium Iodide. The second region is occupied by viable cells surrounding the irradiation site in which molecular delivery was achieved as confirmed by uptake of the 3 kDa FITC-conjugated Dextran. In the third region, few cells were visibly loaded with the 3 kDa FITC-conjugated Dextran; and all of these cells remained viable (as demonstrated in the viability assay shown in Figure 4.3). Again, the zones of cellular damage and optoporation increase with pulse energy.
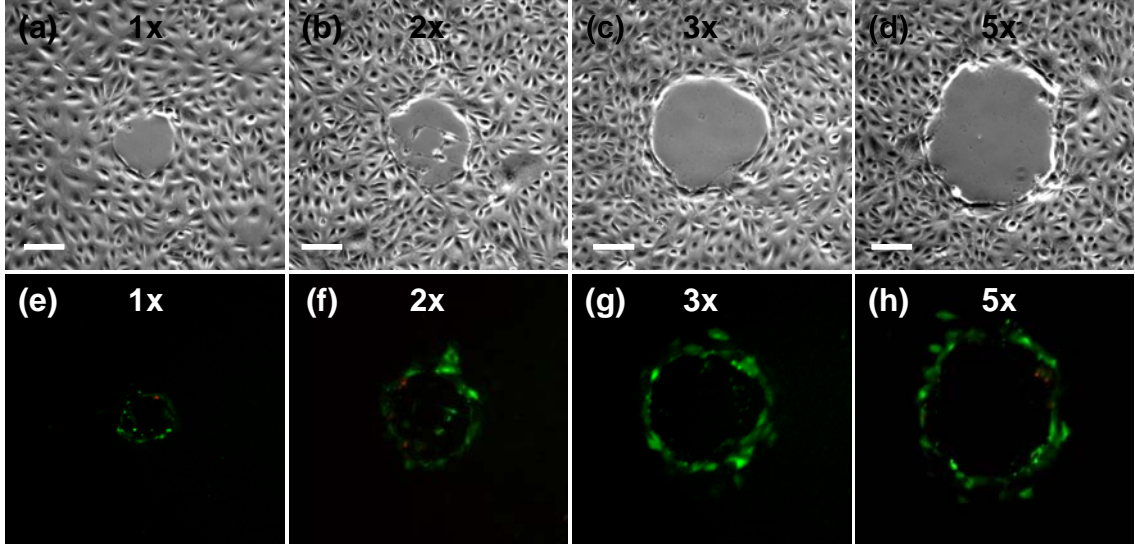
Figure 4.4: Membrane permeabilization after irradiation at energies corresponding to 1x (a,e), 2x (b,f), 3x (c, g) and 5x (d, h) the threshold energy for plasma formation: (a-d) phase contrast image showing the irradiation site and damage zone, (e-d) fluorescent image showing cells loaded with FITC-dextran (green) and propidium iodide (red) staining the nuclei of dead cells around the periphery of the irradiation site. Scale bar = 100 µm.

4.4.2 Characterization of the Zones of Cellular Modification

Collectively, the assays that evaluated the cellular response to laser-generated cavitation bubbles revealed four distinct zones of cellular modification. Previously, we identified the radius of cell lysis, R_{lys}, the radius of the region around the irradiation site that was denuded of cells immediately after laser irradiation [94]. Upon completion of the viability and membrane permeability assays, we found many cells beyond this region to be necrotic and, as mentioned previously and shown in Figure 4.2, detach during the wash process associated with the cell assays. Moreover, a few cells that remained adherent were also necrotic. Therefore, we have defined a second radial location, $r = R_{necr}$, that denotes the maximum radius at which cell necrosis is seen and beyond which cells remain adherent and viable. Beyond this region, we have identified

a radial location, R_{perm}, that characterizes the spatial extent of permeabilized cells i.e., cells that display uptake of the 3 kDa FITC-Dextran following laser irradiation as viewed through standard fluorescence microscopy. Beyond R_{perm} the cells are viable, show no uptake of the 3 kDa FITC-conjugated Dextran and appear to be unaffected by the laser microbeam irradiation. A schematic illustrating these regions is shown in Figure 4.5.
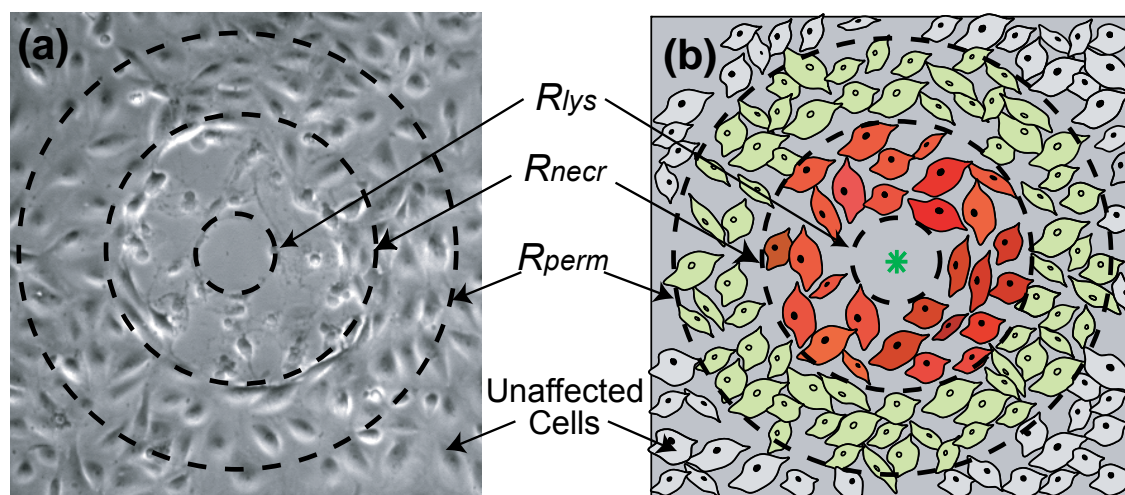
Figure 4.5: Zones of cellular injury. Shown is a phase contrast image (a) and a schematic drawing (b) illustrating the three measured zones of cellular injury. Some of the cells outside of the lysis zone, R_{lys}, have lost viability and wash away during the assay wash process, creating another damage zone, R_{viab}, beyond which cells remain viable. Beyond this region, we have cells that remained viable and showed molecular uptake of dextran, R_{perm}, beyond which the cells to not appear to be affected by the laser irradiation.

The average and standard deviation of the locations of each of these zones were determined by measuring the radius of cellular injury produced at 8-10 irradiation sites. In some instances the zone of cell lysis was slightly elliptical and the radius of a circle of equivalent area was used instead. The radial dimension defining the zones of cellular

injury as a function of pulse energy is shown in Table 4.1. As previously reported in

Chapter 3, we found the radius of cell lysis, $R_{lys,}$ to be 23, 30, 36, and 56 µm for pulse

energies corresponding to 1x, 2x, 3x, and 5x, threshold, respectively [94]. The viability

assays revealed values of R_{necr} to be 66, 105, 134 and 165 µm for pulse energies

corresponding to 1x, 2x, 3x, and 5x, threshold, respectively. The maximum radial

locations occupied by permeabilized cells, R_{perm}, were measured as 101, 162, 202, and

252 µm for pulse energies corresponding to 1x, 2x, 3x, and 5x threshold, respectively.

In Table 4.1 we also provide an estimate for the number of dead and optoporated cells

by taking the product of the area of cell permeabilization and the cell surface density of

1000 cells/mm^2. Collectively, the results demonstrate that increases in pulse energy

produce substantial increases in both the zones of cellular damage and the number of

permeabilized cells.

Table 4.1: Laser pulse energy (E_p), and radius of cell lysis (R_{lys}), radius of viable cells (R_{necr}), radius of permeabilized cells (R_{perm}), and the number of dead and permeabilized cells when using cell cultures with a cell surface density of 1000 cells/mm^2 and pulse energies corresponding to 1x, 2x, 3x, and 5x the threshold for plasma formation.

	E_p [µJ]	R_{lys} [µm]	R_{necr} [µm]	R_{perm} [µm]	# Necrotic Cells	# Permeabilized Cells
1 x Threshold	8	23 ± 4	66 ± 6	101 ± 8	14 ± 2	18 ± 6
2 x Threshold	16	30 ± 4	105 ± 9	162 ± 7	35 ± 6	48 ± 9
3 x Threshold	24	36 ± 2	134 ± 8	202 ± 8	56 ± 6	72 ± 12
5 x Threshold	40	56 ± 6	165 ± 7	252 ± 8	86 ± 7	114 ± 13

4.5   Analysis and Discussion

Our rich data set provides the opportunity to examine the experimental observations with respect to those of other investigators and to explore the possible connection between the zones of cell lysis, necrosis, and cell membrane permeabilization with the underlying physical mechanisms.   From a mechanistic standpoint, we examine the potential contributions of cavitation bubble-induced shear stress and shock wave pressure to cell lysis and cell membrane permeabilization. This is achieved through a quantitative assessment of time-resolved images and hydrodynamic modeling of cavitation bubble expansion generated by the delivery of pulsed laser microbeam irradiation to confluent PtK$_2$ cell cultures at the same pulse energies examined in the cellular assays.   Finally, we will discuss our laser-based molecular delivery results relative to those of other studies, as well as studies in acoustic cavitation literature that examine sonoporation as a means for molecular delivery.

4.5.1   Role of Cavitation Bubble Generated Shear Stress on Cell Lysis and Membrane Permeabilization

As discussed previously, our time-resolved imaging study of the pulsed laser microbeam cell lysis process provided evidence that primary agent for cell lysis and deformation is the dynamic shear stress produced by the cavitation bubble expansion [93, 94]. In Section 3.4.4, we introduced a hydrodynamic model to determine the spatio-temporal evolution of both the fluid velocity and wall shear stress provided by the cavitation bubble dynamics. This model revealed a direct relationship between the

maximum wall shear stress $\tau_{w,max}$ and the extent of cell lysis R_{lys}. A schematic of this model is shown again in Figure 4.6. In this model we assume that the cell monolayer acts as a boundary and that the cells are subject to shear stress due to movement of fluid parallel to this boundary. We consider the fluid motion at locations outside the expanding bubble and define a geometry in which the origin is located at the site of the laser focus immediately above the cell monolayer with z and r being the vertical and radial axes, respectively.
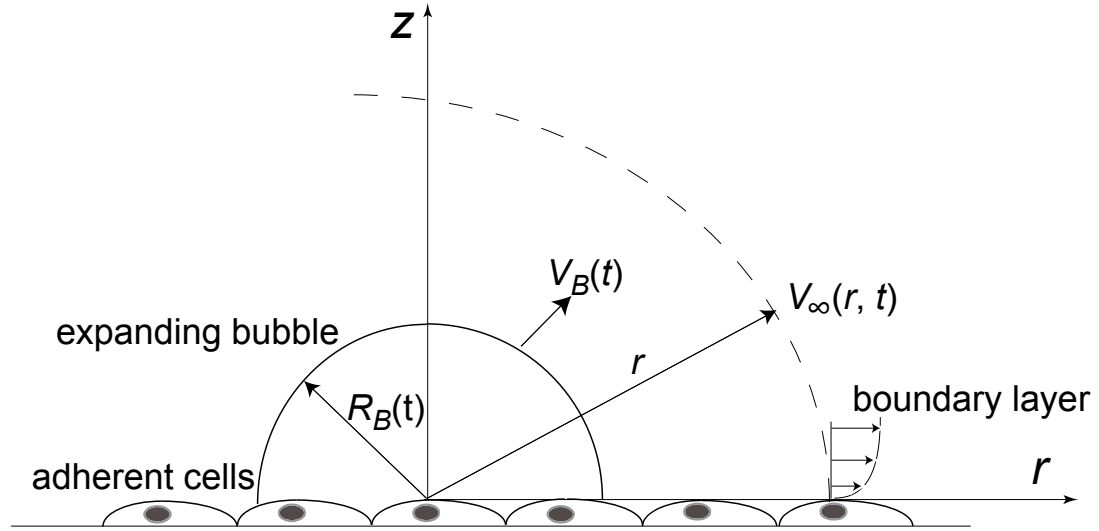
Figure 4.6: Schematic of model problem for hydrodynamic analysis. Figure not to scale.

Time-resolved imaging provided a means to quantify the spatial and temporal evolution of both the radial position $R_B(t)$ and velocity $V_B(t)$ of the bubble wall. Conservation of mass in this system provides the following relationship between the external fluid velocity $V_\infty(r,t)$ and the bubble dynamics as:

$$V_\infty(r,t) = V_B(t)\left[\frac{R_B(t)}{r}\right]^2.$$

(4.1)

Conservation of momentum was then applied to obtain the following expression for the wall shear stress $\tau_w(r,t)$ generated by the cavitation bubble expansion [94]:

$$\tau(r,t) = \rho \sqrt{\frac{\nu}{\pi}} \int_0^t \frac{\partial V_\infty(r,t')}{\partial x} \frac{dt'}{\sqrt{t-t'}} , \tag{4.2}$$

where ρ and ν are the density and kinematic viscosity of the fluid medium [94]. Equation (4.2) is valid at any radial position r and time $0 < t \leq t'$ where t' is the time of arrival of the bubble wall at position r.

The profiles of the temporal evolution of the wall shear stress are characterized generally by a rapid (≤ 30 ns) increase to a maximum value followed by a more gradual decay [94]. Of particular interest is the maximum shear stress at radial positions corresponding to the regions of cell lysis, cell necrosis, and cell membrane permeabilization. In Table 4.2 we provide the maximum wall shear stress predicted by our hydrodynamic analysis at each of these interfaces as described in Section 4.4, i.e. at $r = R_{lys}$, $r = R_{necr}$, and $r = R_{perm}$. This table encompasses pulse energies in the range 8 – 40 µJ, corresponding to energies of 1 – 5x the threshold for plasma formation. Remarkably, even with wide range of pulse energies examined, the range of shear stresses calculated at each zone of cellular injury is quite narrow; typically $\leq 10\%$. The location representing the maximum extent of immediate cell lysis ($r = R_{lys}$) is exposed to maximum wall shear stresses of $\tau_{w,max} > 190 \pm 20$ kPa, whereas the location representing the maximum extent of necrotic cells ($r = R_{necr}$) is exposed to shear stresses of $\tau_{w,max} > 18 \pm 2$ kPa. Finally, the analysis indicates that the molecular delivery to these cells with a 3 kDa FITC-conjugated Dextran through transient membrane permeabilization ($r = R_{perm}$) requires a maximum transient shear stress of

$\tau_{w,max} > 18 \pm 2$ kPa. Cells exposed to $\tau_{w,max} < 8 \pm 1$ kPa remain viable and appear unaffected by the pulsed laser microbeam irradiation.

Table 4.2: Summary of hydrodynamic data and analysis providing the peak wall shear stress $\tau_{w,\,max}$ computed at each zone of cellular injury for pulse energies corresponding to 1x, 2x, 3x, and 5x the threshold for plasma formation.

	E_p [µJ]	Peak wall shear stress $\tau_{w,peak}$ [kPa]		
		@ $r = R_{lys}$	@ $r = R_{necr}$	@ $r = R_{perm}$
1x Threshold	8	180 ± 60	22 ± 4	9.3 ± 1.5
2x Threshold	16	200 ± 50	16 ± 3	6.8 ± 0.6
3x Threshold	24	220 ± 20	16 ± 2	7.0 ± 0.6
5x Threshold	40	170 ± 40	19 ± 2	8.2 ± 0.5
Mean $\pm$ SD		**190 ± 20**	**18 ± 2**	**8.0 ± 1.0**

Figure 4.7 illustrates the interrelationship between the spatial region occupied by the lysed, necrotic, optoporated, and unaffected cells and the maximum transient shear stress for all four pulse energies tested. The curves represent the predictions of the hydrodynamic model for the maximum wall shear stress as a function of radial position for each laser microbeam pulse energy. The shaded regions are defined by the range of shear stresses necessary for the laser microbeam to produce the appropriate cellular effect. The intersection of an individual curve with each shaded region defines the range of maximum wall shear stress and radial positions in which the various cellular effects are achieved for the given pulse energy. The mean and standard deviation of the experimental results for R_{lys}, R_{necr}, and R_{perm} and the corresponding $\tau_{w,max}$ predicted by the hydrodynamic model at these locations are also shown. The location of the experimental data points is remarkably consistent with the boundaries of the shaded regions.
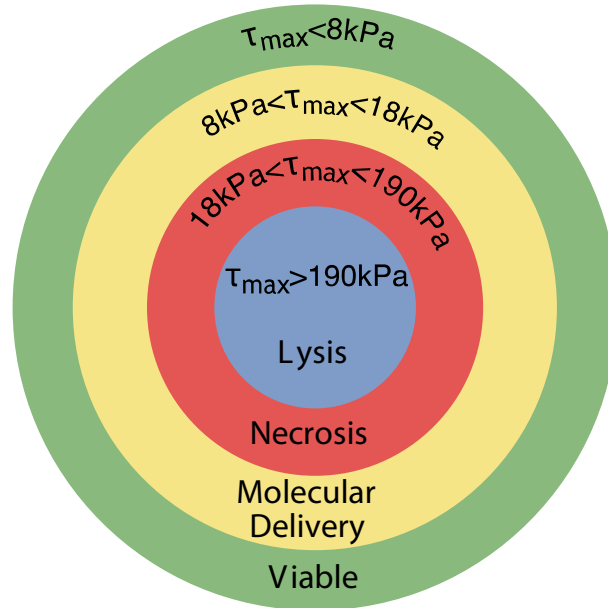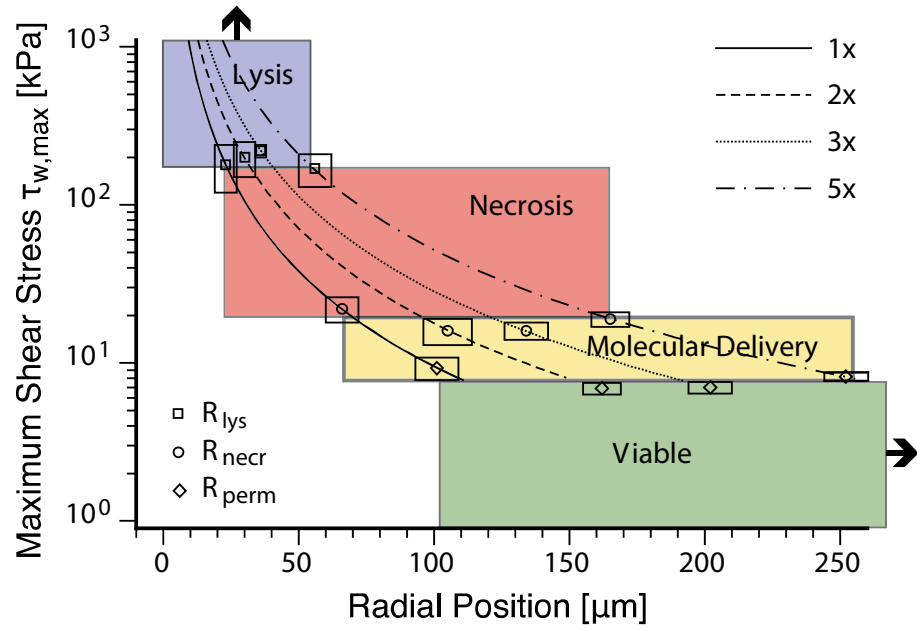
Figure 4.7: Composite diagram showing hydrodynamic model predictions of the maximum wall shear stress $\tau_{w,max}$ as a function of radial position at pulse energies 1x, 2x, 3x, and 5x the threshold for plasma formation. Colored regions indicate the resulting cellular effect. Experimental data points including error bars validate the hypothesis that the specific ranges of maximum shear stress effectively delimit the separation between regions. These shear stress regions and corresponding cellular effect are illustrated pictorially below the main plot.

The collective congruence between experimental results and hydrodynamic modeling identifies a well-defined range of maximum transient wall shear stress of 8 – 18 kPa required to achieve molecular delivery while maintaining cell viability of 3 kDa FITC-conjugated Dextran for PtK$_2$ cells cultured at a density of 1000 cells/mm^2. Transient wall shear stresses below 8 kPa do not achieve optoporation, while transient wall shear stresses above 18 kPa result in loss of cell viability through cell necrosis and detachment and, for $\tau_{w,max} > 190$ kPa, through immediate cell lysis. It is important to emphasize that previous experiments have shown that the maximum shear stresses necessary to produce cell lysis decreases with a reduction in the cell surface density [94]. Thus it is expected that cell surface densities < 1000 cells/mm^2 will result in a lower range of shear stresses to produce optoporation. Moreover, we expect that the specific values of the maximum transient wall shear stress necessary to achieve the observed cellular effects will change with cell type.

4.5.2 Potential Role of Shock/Stress Waves to Achieve Molecular Delivery

Thus far, we have not considered the potential contribution of the shock wave produced by plasma formation to the observed cellular effects. Our study detailed in Chapter 3 provided no evidence for the role of shock waves in the production of the observed cellular effects. Rather, this study implicated the cavitation bubble dynamics as the primary instigator of cellular damage and cell membrane permeabilization. Nevertheless, there have been extensive studies investigating the contribution of laser-generated stress/shock waves to cellular injury as well as molecular delivery [32, 58-60, 62, 63]. The study most relevant to our investigation is that of Kodama and co-workers

who investigated the efficacy of laser-generated and shock tube generated pressure waves to produce molecular delivery of Calcein (MW = 622 Da) and FITC-conjugated Dextran (MW = 71.4 kDa) into the cytoplasm of HL-60 human promyelocytic leukemia cells. They found that the efficacy of molecular delivery was not correlated with the maximum shock wave pressure but rather with the shock wave impulse as estimated by the product of the maximum pressure and the shock duration. They found that to achieve molecular delivery to roughly 45% of the cells requires an impulse of 50 Pa·s for Calcein and 150 Pa·s for the 71.4 kDa FITC-conjugated Dextran.

We have previously measured velocity of the shock waves produced by pulsed laser microbeam irradiation as a function of both pulse energy and radial position to determine the shock wave pressure [93]. This analysis reveals that the cells are successfully optoporated and receive maximum shock pressures not exceeding 50 MPa [93] with a characteristic duration of 40 ns [126]. This results in a maximum impulse of 2 Pa·s; 25 x below the impulse required to achieve molecular delivery as reported by Kodama and co-workers. We thus conclude that the shock wave associated with the cell microbeam irradiation are unlikely to provide a contribution to the observed molecular delivery of 3 kDa FITC-conjugated Dextran in our system. Nevertheless, there may be similarities in the underlying mechanism by which shock waves and transient fluid shear stress cause structural changes in the cell membrane to facilitate molecular delivery. Such structural changes in the phospholipid bilayer have been recently investigated via molecular dynamics simulations by Koshiyama and co-workers for the case of shock wave-generated molecular delivery [60]. Clearly the use of such computational methods to examine the impact of transient fluid shear stress on

the structure of the phospholipid bilayer would represent an important next step to elucidate the molecular mechanisms of this process.

4.5.3 Implications for Molecular Delivery and Acoustic Cavitation Studies

The characteristics of our molecular delivery results are similar to those reported by Soughayer and co-workers who investigated the molecular delivery of rat basophilic leukemia (RBL) cells using a single 5 ns, λ =532 nm laser pulse with 10 μJ pulse energy delivered via a 100x, 1.3 NA microscope objective [109]. The RBL cells were placed in a 170 μM solution of 3 kDa Texas Red-conjugated Dextran. Soughayer and co-workers identified three distinct zones of cellular response following the pulsed laser microbeam irradiation: (a) a region of dead and/or detached cells at distances of up to 30 μm from the laser irradiation site, (b) a region of optoporated, viable cells 31-60 μm from the irradiation site, and (c) seemingly unaffected, viable cells that showed little uptake of the Texas Red-conjugated Dextran at distances 60 μm from the irradiation site. Differences between the spatial extent of the three zones of cellular effects between the two studies are likely due to the different cell types, cell surface density, and microscope objective. Our results for 8 μJ pulse energy (1x threshold) provides a similar 30 μm range for immediately lysed cells and a similar 30 μm wide region of permeabilized cells.

Also of interest is a comparison of our results with the use of cavitation bubbles created by acoustic means for applications in cell lysis, cell detachment, and molecular delivery [60, 61, 81, 93, 94, 143]. Recently, much attention has been given to the use of ultrasonic techniques to achieve molecular delivery to cells and tissues for therapeutic

applications such as transdermal drug delivery, gene therapy, and delivery of chemotherapeutic drugs to tumors [77]. The use of low-amplitude ultrasound to achieve transient cell membrane permeabilization for molecular delivery is known as reparable sonoporation [139]. It has been found that sonoporation is enhanced significantly when cavitation bubbles are present during the acoustic exposure, suggesting that a fluid dynamic interaction between cavitation bubbles and cells is responsible for membrane poration [4, 80, 139]. The physical mechanism of sonoporation is not well understood and thus the dependence of membrane permeabilization on the cavitation parameters is not yet known [75, 115]. A better understanding of the physical mechanisms responsible for the poration of the cell membrane is crucial for the optimization of this technique. As a result many groups are examining ultrasound-generated cavitation bubble dynamics and the resulting fluid velocities to determine the shear stresses and exposure times required to achieve sonoporation, cell detachment, and cell lysis [51, 80, 81, 143, 144].

Wu and co-workers have examined acoustic cavitation by subjecting an erythrocyte suspension to an oscillating probe called a Mason horn set to a frequency of 20 kHz, a technique referred to as microstreaming [143, 144]. They developed a mathematical model to estimate the shear stress experienced by Jurkat leukocytes subject to microstreaming and concluded that the shear stress produced by the Mason horn was the primary mechanism for the cells demonstrating reparable sonoporation. This study determined that a threshold shear stress of 12 ± 4 Pa is required for reparable sonoporation for exposures of up to 7 minutes [143, 144]. Similar studies using microstreaming have also determined shear stress to be the mechanism of hemolysis of

erythrocytes, with a critical shear stress for hemoglobin release was found to be in the range of 300 - 450 Pa [140, 144]. Threshold shear stresses have not been determined for all cell types, but it has been shown that lysis of red blood cells by local shear has a strong dependence on cell volume [74, 76]. Extrapolation of these data to endothelial cells predicts lysis to occur at stresses of ~ 800 Pa [125]. Studies by Ohl and Wolfrum found a 100-160 Pa shear stress required for detachment of cultured HeLa cells using a lithotripter [81], and reparable sonoporation was observed at shear stresses below the 100 Pa required for cell detachment. In all of these studies, the reported shear stress values for molecular delivery and cell lysis are on the order of 100 Pa for exposure times on the order of minutes. By contrast, the shear stress values required for cell lysis and molecular delivery using pulsed laser microbeams are in the 10-100 kPa regime; stress magnitudes that are larger by two to three orders of magnitude! However, the duration of these stress transients are on the order of nanoseconds to microseconds. This strongly suggests that there exists a time-stress dependent mechanism for stress-mediated permeabilization and damage to the cell membrane.

The use of sonoporation for molecular delivery to cells and tissues holds promise for many therapeutic applications in medicine. However, typical sonoporation experiments result in the production of multiple cavitation bubbles whose exact size and location are not controlled. The use of pulsed laser microbeams offers the advantage of creating individual cavitation bubbles of specific size and location. This enables the generation of controlled and reproducible regions of cellular damage and/or molecular delivery. Moreover, with the potential development of laser microbeam platforms that offer multiple wavelengths ($\lambda = 355, 532, 1064$ nm) and a range of pulse durations (ns –

fs) that can provide for optical breakdown over a range of pulse energies [133, 136], one can easily conceive of a single platform that can provide for precise zones of cellular damage and molecular delivery over a broad range.

4.6 Conclusion

We have examined the cellular response of adherent PtK_2 cell monolayers to nanosecond pulsed laser microbeam irradiation. Cell viability and membrane permeability assays combined with microscopic examination have identified and quantified regions of (a) immediate cell lysis, (b) cell necrosis, and (c) molecular delivery in response to 6 ns pulsed laser microbeam irradiation at $\lambda = 532$ nm in cell monolayers cultured at a density of 1000 cells/mm^2. Hydrodynamic analysis of the cavitation bubble dynamics produced by the laser microbeam irradiation revealed that over a 5-fold variation in laser microbeam energy, the spatial extent of each of these regions is linked to the maximum transient shear stress produced by the fluid displaced by the cavitation bubble expansion. Specifically, cells immediately adjacent to the site of irradiation that experienced maximum transient wall shear stresses $\tau_{w,max} > 190 \pm 20$ kPa were immediately lysed. Cells situated further away that were exposed to $\tau_{w,max}$ 19 ± 2 kPa remained intact but were necrotic. Cells positioned more distant that received maximum shear stresses in the range $8 \pm 1 \leq \tau_{w,max} \leq 19 \pm 2$ kPa remained viable and were successfully optoporated with 3 kDa FITC-conjugated Dextran molecules. At all pulse energy, cells were transiently permeabilized up to 2 to 3 layers around the lysis zone, indicating that this range of shear stresses produce a transient, but repairable, disruption in the plasma cell membrane. Finally cells most

distant from the irradiation site that received $\tau_{w,max} < 8 \pm 1$ kPa remained intact, viable and free of molecular delivery.

Of interest is the fact that the ranges of maximum shear stresses necessary to produce cell lysis, necrosis and molecular delivery using laser microbeams are of the order of $10 - 100$ kPa; roughly 3 orders of magnitude larger than those typically utilized for cell lysis and molecular delivery by the ultrasonic community. The important difference is that the exposure to these stresses are typically of the order of $0.1 - 10$ μs when using pulsed laser microbeam irradiation and $1 - 100$ seconds when using ultrasonic sources. This strongly suggests a stress-time dependent mechanism for mechanical damage of the cell membrane that warrants further examination.

In this chapter, we have identified a well-defined range of maximum wall shear stress ($\sim 8 - 18$ kPa) required to achieve molecular delivery through optoporation. Through investigation of the damage zones and resulting shear stress caused by cavitation bubble expansion, this technique can be used to optimize optoporation of diverse molecules into varying cell types. In contrast to sonoporation, the use of pulsed laser microbeams offer the advantage of producing cavitation bubbles with reproducible size and specific location that, in turn, can produce well-defined, reproducible zones of cell lysis, optoporation, and cell viability. In Chapter 5, we will examine if a variation of laser microbeam pulse duration may allow modulation of the spatial extent of cellular modification in order to tailor the cellular perturbations and optimize specific applications for cell lysis, cell detachment, and/or molecular delivery.

4.7   Acknowledgements

Chapter 5

EFFECT OF PULSE DURATION ON THE USE OF LASER MICROBEAMS FOR CELL LYSIS AND MOLECULAR DELIVERY

5.1   Abstract

Time-resolved imaging and fluorescence microscopy were used to examine the effects of the variation of laser microbeam pulse duration on cavitation bubble dynamics and the subsequent cellular injury. This was accomplished by delivering 532 nm laser pulses with picosecond and nanosecond pulse durations via a 40x, 0.8 NA microscope objective to a confluent monolayer of PtK_2 cells. The process is initiated by laser-induced plasma formation, and it has been shown that cell necrosis and molecular delivery are achieved by the fluid shear stress produced during the cavitation bubble expansion. Here, we study the process dynamics of laser-induced cell injury and transient membrane permeabilization using laser pulse durations ranging from 180 ps to 1100 ps and pulse energies of 0.5 to 10 μJ corresponding to 1x, 2x, 3x, and 5x the threshold for plasma formation. This process is imaged at times of 0.5 ns to 50 μs following delivery of the pulse laser microbeam to visualize the cavitation bubble dynamics. Fluorescence assays are used to assess the subsequent cell viability and molecular delivery. The spatial extent of cell lysis, cell necrosis, and molecular

delivery increased with laser pulse duration and pulse energy. Hydrodynamic analysis from time-resolved imaging revealed that the maximum wall shear stress associated with the pulsed laser microbeam-induced cavitation bubble expansion governs the location and spatial extent of these regions.

5.2   Introduction

Thus far, we have characterized the physical perturbations offered by the delivery of 6 ns laser microbeam pulses to adherent cells, and have assessed the biological response of the cells to characterize the spatial extant of cell lysis and molecular delivery. This chapter examines the ability to selectively modulate the spatial degree of cellular perturbations using pulsed laser microbeams of varying pulse durations.

We have previously characterized the physical interaction and subsequent biological response of cells irradiated with 6 ns, $\lambda = 532$ nm pulsed laser microbeam irradiation as a function of pulse energy [44, 93, 94]. In Chapter 3, time-resolved imaging was used to verify that the cavitation bubble expansion is the primary agent of cell lysis when using 6 ns laser microbeams focused at a location 10 μm above the cell monolayer, and that fluid shear associated with cavitation bubble expansion is the physical process that governs the spatial extent of cellular injury. In Chapter 4, we provided an assessment of the cellular biological response using fluorescence assays to identify quantified regions of (a) immediate cell lysis, (b) cell necrosis, and (c) molecular delivery via optoporation in response to 6 ns laser microbeam irradiation in cell monolayers cultured at a density of 1000 cells/mm^2. Hydrodynamic analysis of

the cavitation bubble dynamics produced by the 6 ns laser microbeam irradiation revealed that over a 5-fold variation in laser microbeam energy, the spatial extent of each of these regions is linked directly to the maximum transient shear stress produced by the fluid displaced by the cavitation bubble expansion. It is clear that fluid shear created by the cavitation bubble dynamics is strongly dependent on laser pulse energy, and enables control of the spatial extent of cell lysis, necrosis, and molecular delivery. In this chapter, we will examine how the variation of pulse duration may allow modulation of the relative sizes of these areas of cellular modification in order to tailor the cellular perturbations and optimize specific applications for cell lysis, cell detachment, and/or molecular delivery.

The impact of pulse duration on optical breakdown was discussed previously in Section 2.3. For nanosecond pulses, cascade ionization is the dominant contributor to plasma formation. As pulse duration is decreased from the nanosecond to picosecond time scale, there is less time to generate additional free electrons through cascade ionization, and multiphoton absorption begins to play a larger role the optical breakdown process [127]. Because the mechanisms that are responsible for the generation of free electrons are governed more by a critical irradiance (power/area) as opposed to a critical radiant exposure (energy/unit area), plasmas can be formed using much smaller laser pulse energies when shorter pulse durations are used. Therefore, picosecond laser microbeams may provide more spatially localized effects as compared to the use of nanosecond laser microbeams. Moreover, they may provide more subtle perturbations such as microsurgery and optoinjection.

Our discussion in Chapter 4 ended with a schematic diagram depicting hydrodynamic model predictions of the maximum wall shear stress as a function of radial position at varying pulse energies (Figure 4.7). These experimental results validated our hypothesis that the specific ranges of maximum shear stress effectively delimit the separation between regions of damage. In this chapter, we study the effect of changing pulse duration on cell lysis and molecular delivery. We will investigate if the variation of pulse duration can modify not only the spatial extent of cellular injury, but also the relative sizes of these zones of cellular damage. For example, one particular area of interest in this study is to determine if there exists a pulse duration/energy selection that minimizes cell necrosis, while maximizing cellular injury. Here we aim to establish relationships between the laser microbeam parameters and the subsequent biological response.

5.3   Materials and Methods

5.3.1   Cell Irradiation

An inverted microscope (Axiovert S100, Zeiss, Jena, Germany) was used as the experiment platform. A frequency-doubled Nd:YAG laser (SL332, Ekspla, Lithuania) provides pulses with durations between 180 - 1100 ps at $\lambda = 532$ nm was used for cell irradiation. As shown in Figure 5.1, the linearly polarized laser output was directed through a $\lambda/2$ plate followed by a polarization-sensitive beam splitter, dividing the beam into two components of low and high energy. The low energy beam line was directed through a linear polarizer to allow adjustment of the laser pulse energy, followed by a spatial filter and iris to select the central portion of the beam. The beam was then

directed into the epifluorescence port of the microscope, and reflected upward into the rear entrance aperture of the objective by a dichroic mirror (532rdc, Chroma Technology Corp., Rockingham, VT) placed in the microscope filter cube. The laser pulse energy entering the rear entrance aperture of the objective was measured by removing the objective from the microscope turret and allowing the unobstructed beam to illuminate an energy detector (Model No. J5-09, Coherent, Santa Clara, CA) set on the microscope stage. Pulse-to-pulse energy variation was found to be $\pm$ 5 %. A bright-field objective (Zeiss Achroplan 40x, 0.8 NA) was used for cell irradiation. The focal plane of the pulsed laser microbeam was positioned at a separation distance of 10 μm above the cell monolayer.
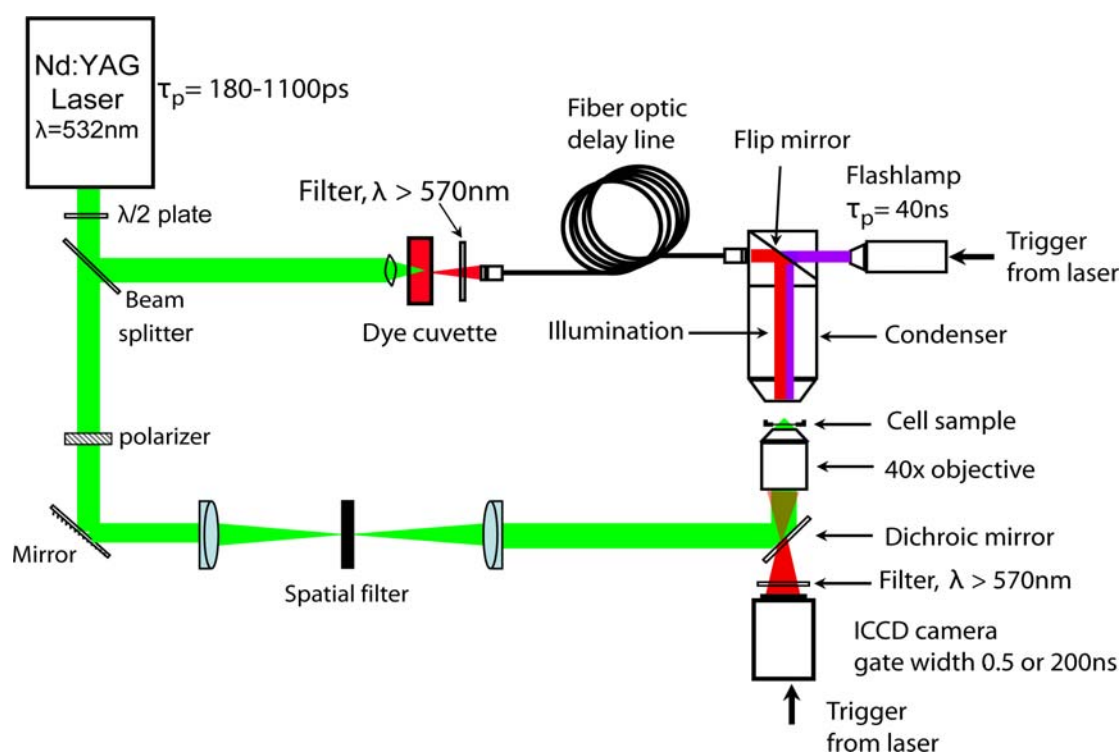
Figure 5.1: Schematic of laser-microscope setup for time-resolved imaging of cell irradiation using varying picosecond pulse durations.

5.3.2 Time-Resolved Bright-Field Imaging of Laser-Induced Cavitation Bubble Dynamics

Illumination for the time-resolved images was provided by delivering a short light pulse at the desired time delay after the arrival of the Nd:YAG laser pulse at the sample. As depicted in Figure 5.1, the high energy beam line was focused into a glass cuvette containing a fluorescent dye (Model No. LDS 698, Exciton, Dayton, OH) that was excited by the λ_{ex} = 532 nm laser pulse and emits light at λ_{em} = 698 nm. The emitted light was coupled into a 600-µm-core diameter multimode optical fiber (Model No. UMT 600, 0.39 NA, Thor Labs, Newton, NJ), and the fiber output was directed into the microscope condenser to illuminate the sample for time-resolved imaging. Optical fibers of different length were used to provide the desired time delay between delivery of the arrival time of the fluorescent emission relative to the arrival of the low energy beam line at the sample. The fluorescence emission from the dye cell provided illumination at λ = 698 ± 20 nm with a full width at half-maximum duration of 15 ns. The maximum delay time for the fiber optic delay line was 2000 ns. At longer time delays, illumination was provided by an ultrashort duration flash lamp (Nanolite KL-L, High-Speed Photo System, Wedel, Germany) that was electronically triggered from the camera. The flash lamp emission provided a broad spectral output (λ = 400-700 nm) with a full width at half-maximum duration of 40 ns.

Images were acquired using a gated intensified CCD camera (PI-MAX 512, Roper Scientific, Trenton, NJ) that was triggered by a TTL pulse from the laser Q-switch. The camera operation and image acquisition was performed using WinView32 imaging software (Princeton Instruments, Trenton, NJ). The camera gate duration was

set to 0.5 ns when using the fluorescent dye cell for illumination and to 500 ns when using the flash lamp illumination due to the electronic jitter in the flash lamp triggering. Thus, for time delays shorter than 3.6 µs, the exposure duration was governed by the 0.5 ns camera gate width, while at longer time delays the exposure duration was governed by the 40 ns duration of the flash lamp. A longpass filter (Model No. LP 570, Edmund Optics, Barrington, NJ) was used to prevent scattered laser radiation from reaching the camera. This system allowed us to irradiate and image the sample at time delays of 0.5 ns to 50 µs required to capture the full dynamics of the process.

5.3.3   Fluorescence Imaging

A Quantix CCD camera (Photometrics, Roper Scientific, Trenton, NJ) was used for the fluorescence and phase contrast imaging, with 20x, 0.45 NA Phase 2 (Zeiss A Plan, Jena, Germany) and 10x, 0.3 NA Phase 1 (Zeiss Plan-NEOFLUAR, Jena, Germany) objectives. Camera operation and image acquisition was performed using V++ imaging software (Photometrics, Roper Scientific, Trenton, NJ). Image intensity levels were adjusted and images were compiled using Adobe Photoshop 7.0 (Adobe, San Jose, CA). The irradiation sites were imaged in both phase contrast and epifluorescence after the cell assays were completed. A minimum of 10 sites for each pulse duration and energy were examined using fluorescence assays.

5.3.4 PtK$_2$ Cell Culture

Potorous rat kidney epithelial (PtK$_2$) cells were grown in polystyrene culture dishes with glass bottoms (P35G-0-14-C, MatTek, Ashland, MA) in advanced minimum essential medium (Advanced MEM, Invitrogen, Carlsbad, CA) supplemented in 1% fetal calf serum, L-glutamine, amphomycin, and gentamicin sulfate. The culture medium was prepared free of phenol red to ensure its transparency to $\lambda = 532$ nm radiation. Cells were cultured in a humidified incubator with a constant temperature of 37°C and a 5% CO$_2$ level. Culture dishes with cells at 100% confluence were used in each experiment. These cells did not exhibit contact inhibition and the surface density (cells/mm^2) was measured and controlled. The results provided are for cell monolayers cultured at a surface density of 1000 cells/mm^2. The cell surface density was determined by counting the number of cells in a square 0.5 mm x 0.5 mm region centered at the site of cell lysis. The site-to-site variation in cell surface density was kept below 10%.

5.3.5 Cell Viability Assay

Cell viability was assessed using Calcein AM (Invitrogen, Carlsbad, CA), a membrane permeant dye that readily passes through the cell membrane of viable cells and is hydrolyzed by esterases to form Calcein which remains inside the cell. Dead cells were identified by Propidium Iodide (Invitrogen, Carlsbad, CA), a DNA intercalating agent that stains the nuclei of dead cells. Cell culture dishes were incubated 30 minutes after laser irradiation and loaded with 2 μM Calcein AM and

5 µg/mL Propidium Iodide by incubation for 20 min. To remove the remaining dyes, cells were washed carefully with medium three times before imaging.

5.3.6   Molecular Delivery Assay

Prior to laser irradiation, cells were placed in a 500 µM solution of Fluorescein isothiocyanate (FITC) conjugated dextran (Sigma, MW = 3 kDa). Cells were lysed and incubated for 30 minutes at 37°C, and a 5 µg/mL solution of Propidium Iodide (PI) was added. Cells were incubated for 20 minutes and washed with buffer three times before imaging.

5.4   Results

5.4.1   Plasma Threshold Energy for Varying Pulse Durations

Prior to the cell irradiation experiments, we determined the threshold for plasma formation at specific pulse durations. This was achieved by delivering an Nd:YAG laser pulse via the 40x, 0.8 NA bright-field objective into a Petri dish filled with culture medium. The luminescence produced by plasma formation in the culture medium was observed visually in a dark room and its incidence for 50 pulses at discrete pulse energies was recorded. The probability of plasma formation p as a function of pulse energy E_p for each pulse duration was fit to a Gaussian error function in the form $p(E_p) = 0.5[1 + \mathrm{erf}\,[S(E_p + E_{th})]]$, where S is the 'sharpness' of the error function and E_{th} is the threshold pulse energy at which the probability of plasma formation is 50%. Figure 5.2 shows the result of the experiment when using pulse durations of 180 ps, 280 ps, 360 ps, 540 ps, and 1100 ps along with the model fits. Reduction in pulse duration from

6 ns to 0.18 ns (33x) achieves an 18-fold reduction in plasma threshold energy. For each pulse duration and corresponding threshold pulse energy, we also calculated the resulting threshold irradiance (I_{th}) while assuming the laser beam radius in the focal plane is the diffraction-limited spot size of 0.405 μm for a 0.8 NA objective. Table 5.1 provides the values of S, E_{th} and I_{th} for each pulse duration tested. Plasma threshold energy increased with increasing pulse duration as expected, while shorter pulse durations increased the sharpness of the plasma threshold.
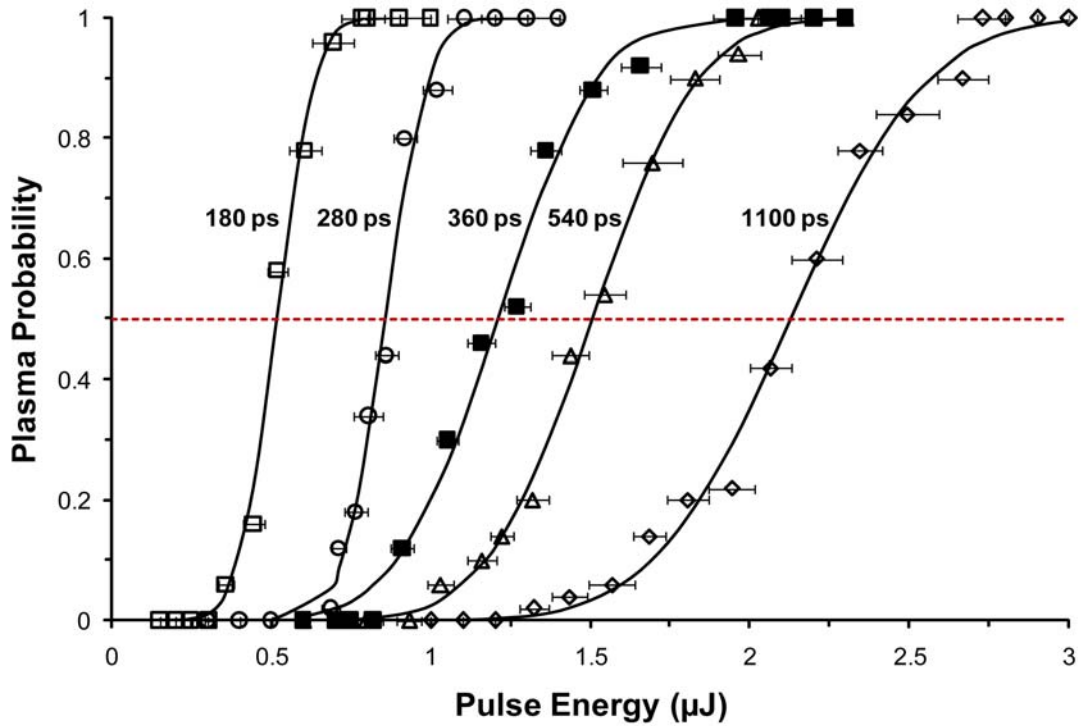
Figure 5.2: Probability of plasma formation as a function of laser pulse energy with Gaussian error function fit for pulse durations of 180 ps, 280 ps, 360 ps, 540 ps, and 1100 ps.

Table 5.1: Sharpness 'S' of the error function and plasma threshold energy values, E_{th}, for varying pulse durations.

Pulse duration [ps]	S [1/µJ]	Threshold Energy E_{th} [µJ]	Threshold Irradiance I_{th} [W/mm^2]
1100	2.1 ± 0.1	2.13 ± 0.01	3.76×10^9
540	2.9 ± 0.2	1.21 ± 0.01	4.35×10^9
360	5.0 ± 0.3	0.97 ± 0.01	5.21×10^9
280	6.7 ± 0.6	0.86 ± 0.01	5.94×10^9
180	8.1 ± 0.3	0.45 ± 0.01	4.85×10^9

5.4.2   Time-Resolved Imaging of Laser-Induced Cavitation Bubble Dynamics

Time-resolved imaging was used to visualize the dynamics of the shock wave propagation and cavitation bubble formation, expansion, and collapse at various time points for pulse durations of 180 ps, 360 ps, 540 ps, and 1100 ps at energies corresponding to 1x, 2x, 3x, and 5x the threshold energy for plasma formation. Figure 5.3 provides representative time-resolved image series depicting these dynamics at various time points at energies corresponding to 2x the threshold for plasma formation for two different pulse durations. Figure 5.3 (a)-(f) shows cavitation bubble dynamics resulting from 180 ps pulses at a pulse energy of 1 µJ and Figure 5.3 (g)-(h) shows the dynamics resulting from 1100 ps pulses at an energy of 4.2 µJ. Close examination of Figure 5.3 (a) and (g) reveal the formation of a shock wave resulting from the rapid plasma expansion that quickly passes out of the field of view. Pressure amplitude estimates approach 500 MPa close to the irradiation site [93]. The pressure wave passage did not cause any visible disruption within the cell monolayer.
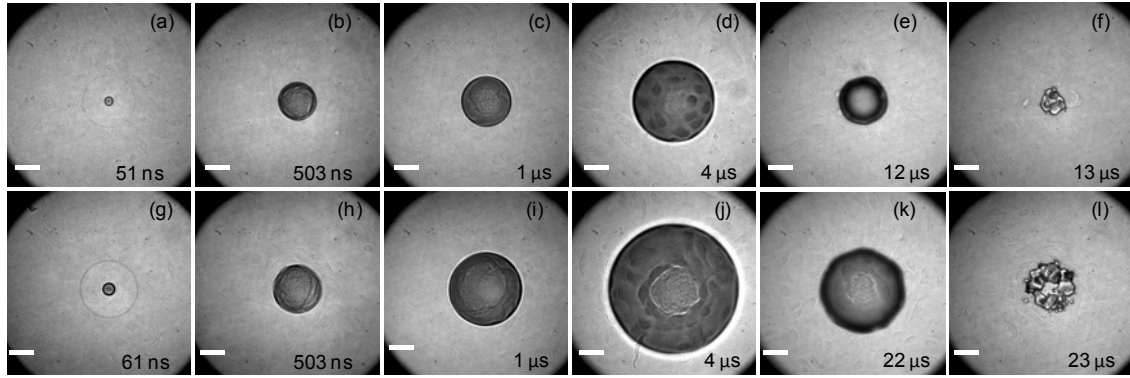
Figure 5.3: Time-resolved image series of the cell lysis process for two pulse durations at energies corresponding to 2x the threshold for plasma formation. (a)-(f) 180 ps pulse at 1 µJ and (g)-(l) 1100 ps at 4.2 µJ.

The plasma expansion resulted in cooling and ion-recombination, thereby leading to the formation of a cavitation bubble within 12 ns following the laser pulse for all pulse durations used. Figure 5.3 (b)-(d) and (h)-(j) reveal that cavitation bubble expansion is the primary mechanism of cell lysis, consistent with our reports for cell lysis using 6 ns pulses [94]. Cell injury is visible within the central region of the bubble and progresses as the bubble continues to expand, thereby increasing the zone of cellular injury. For both pulse durations shown, we can observe the formation of a distinct zone of cellular injury/lysis within 500 ns. Beyond this time point, further bubble expansion does not result in additional visible cellular injury. Instead, further bubble expansion incorporates the cells without lysing them [Figure 5.3 (d) and (j)]. An interesting feature is the transient cellular deformation produced by the bubble expansion, evident both outside and inside the bubble [Figure 5.3 (d) and (j)]. Remarkably, these cells appear to withstand this severe deformation without detachment or visible disruption. After reaching its maximum size, the subsequent bubble collapse phase is rapid, collapsing within 1-3µs for all pulse durations and

energies examined. Note that the use of shorter pulse durations and smaller pulse energies, the cavitation bubble reaches its maximum size and collapses more rapidly. The bubble collapse did not produce further cellular injury but does clear the cellular debris in the cell lysis zone.

We measured the temporal evolution of the cavitation bubble size from a sequence of time-resolved images for pulse durations of 180 ps, 360 ps, 540 ps, and 1100 ps for pulse energies corresponding to 1x, 2x, 3x, and 5x the threshold for plasma formation for each, shown in Figures 5.4, 5.5, 5.6, and 5.7, respectively. A minimum of three images were used to calculate the average and standard deviation for each data point shown.
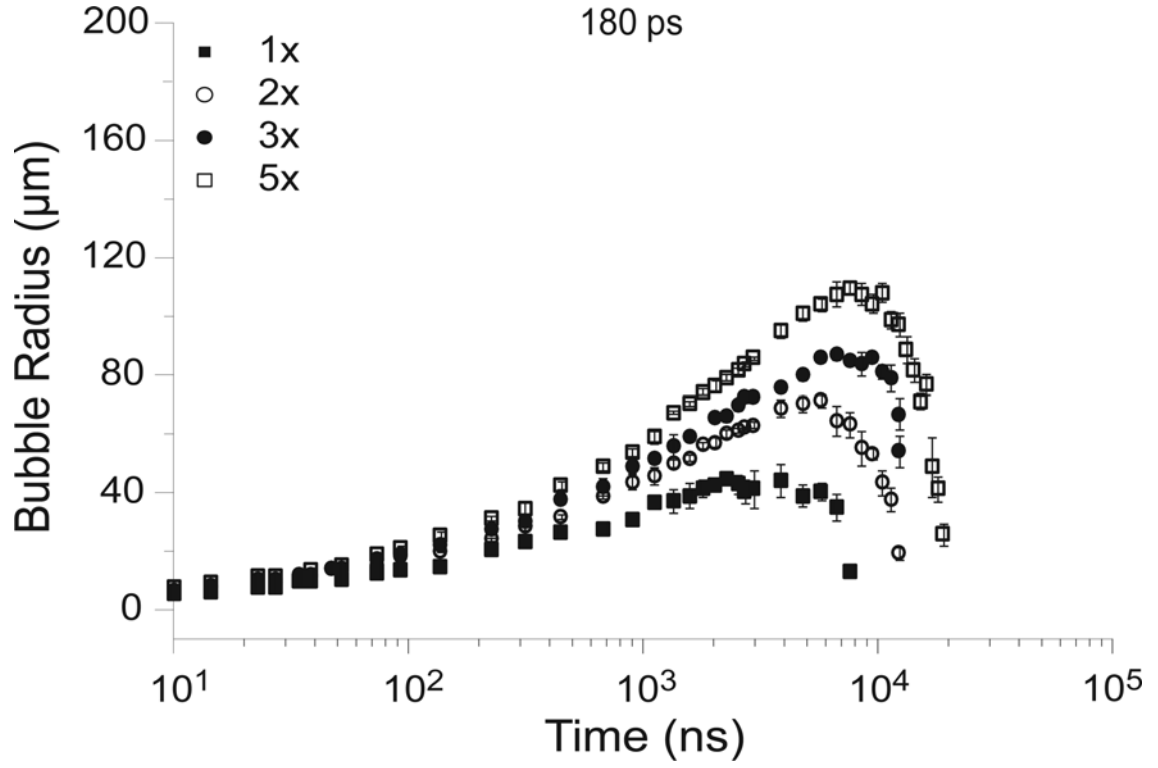
Figure 5.4: Cavitation bubble dynamics for 180 ps laser microbeam pulses at energies corresponding to 1x, 2x, 3x, and 5x the energy for plasma formation. Each data point represents the average of three time-resolved images.
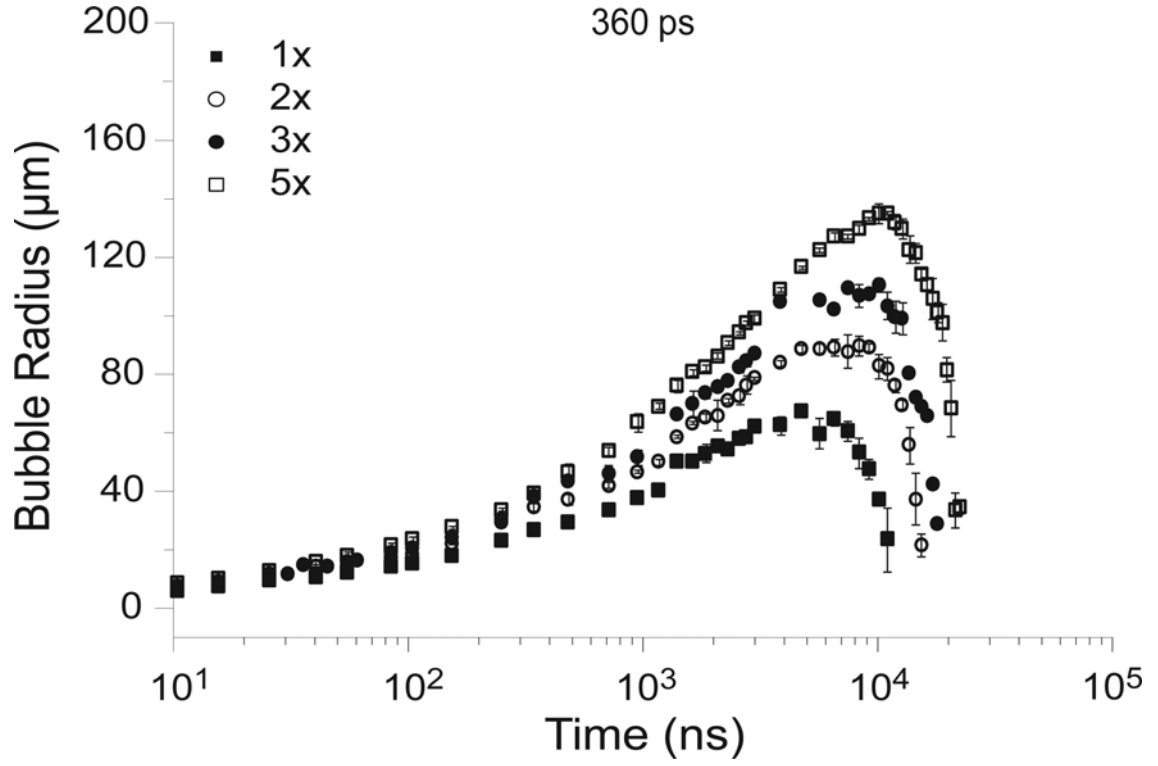
Figure 5.5: Cavitation bubble dynamics for 360 ps laser microbeam pulses at energies corresponding to 1x, 2x, 3x, and 5x the energy for plasma formation. Each data point represents the average of three time-resolved images.
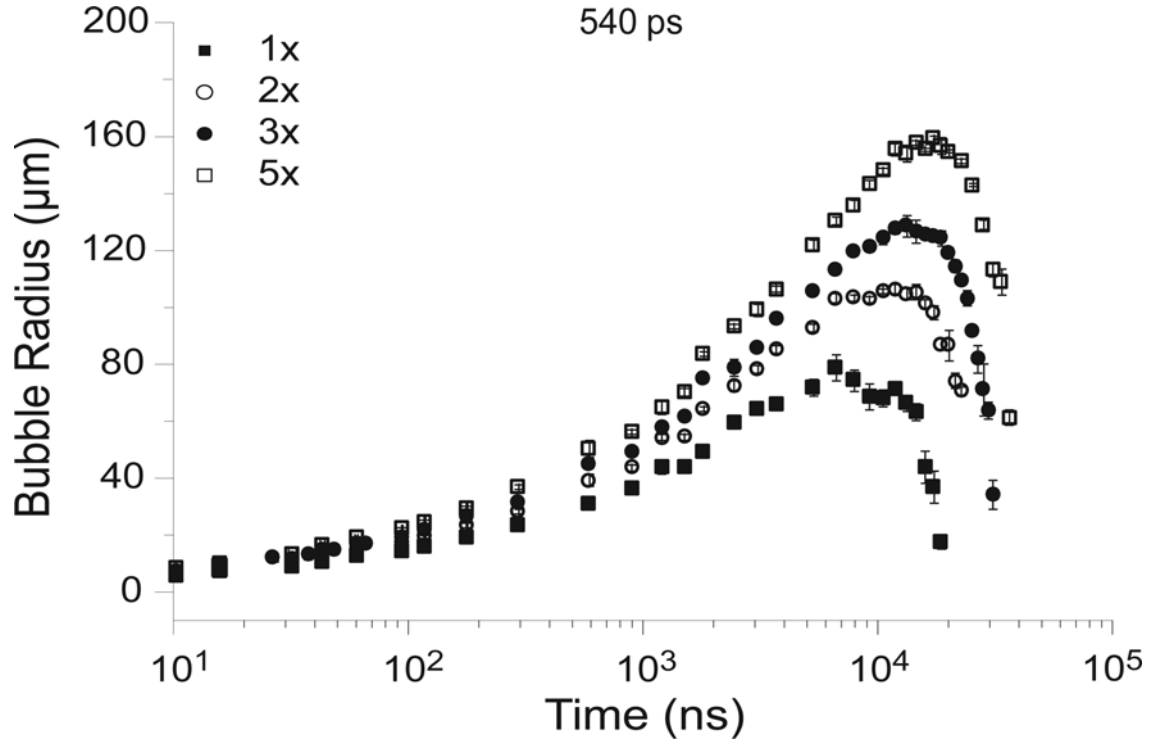
Figure 5.6: Cavitation bubble dynamics for 540 ps laser microbeam pulses at energies corresponding to 1x, 2x, 3x, and 5x the energy for plasma formation. Each data point represents the average of three time-resolved images.
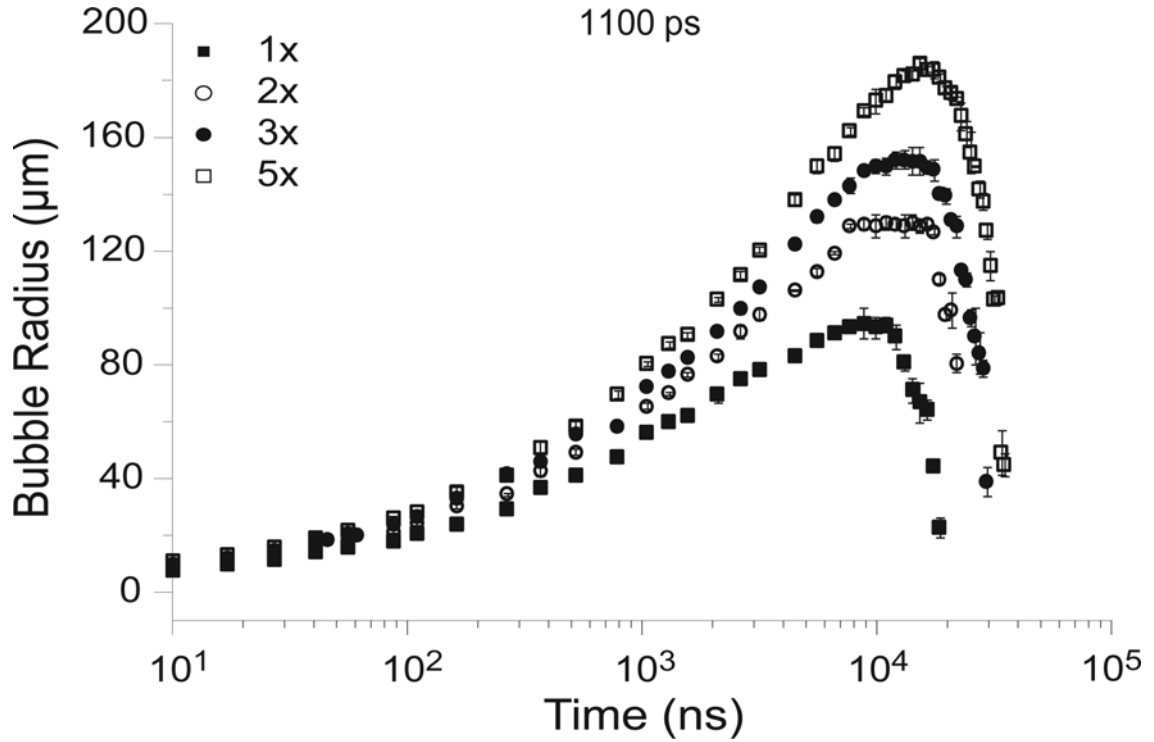
Figure 5.7: Cavitation bubble dynamics for 1100 ps laser microbeam pulses at energies corresponding to 1x, 2x, 3x, and 5x the energy for plasma formation. Each data point represents the average of three time-resolved images.

Table 5.2 lists the vales for the maximum bubble radius R_{max} and oscillation time T_{osc} for each pulse duration and energy observed. The bubble energy calculated using Eq. 3.4 (detailed description in Chapter 3) as well as the percentage of the laser pulse energy transduced into bubble energy [(E_B/E_p) x 100], are also shown in Table 5.2.

Table 5.2: Laser pulse energy (E_p), maximum cavitation bubble radius (R_{max}), oscillation time (T_{osc}), mechanical bubble energy (E_B), mechanical transduction efficiency (E_B/E_p) when using energies corresponding to 1x, 2x, 3x, and 5x the threshold for plasma formation.

Pulse Duration t_p		E_p [µJ]	Meas. T_{osc} [µs]	Meas. R_{max} [µm]	Calc. R_{max} [µm]	E_B [µJ]	E_B/E_p [%]
180 ps	1x Threshold	0.45	8	44 ± 2	43	0.02	3.92
	2x Threshold	0.90	13	71 ± 2	71	0.07	8.24
	3x Threshold	1.35	16	87 ± 2	87	0.14	10.11
	5x Threshold	2.25	20	109 ± 2	110	0.27	11.93
360 ps	1x Threshold	0.96	12	69 ± 2	65	0.07	7.09
	2x Threshold	1.92	17	92 ± 4	92	0.16	8.40
	3x Threshold	2.88	20	111 ± 4	110	0.28	9.84
	5x Threshold	4.80	25	139 ± 4	140	0.56	11.59
540 ps	1x Threshold	1.2	13	79 ± 5	71	0.10	8.51
	2x Threshold	2.4	19	107 ± 2	100	0.25	10.58
	3x Threshold	3.6	23	129 ± 4	130	0.44	12.36
	5x Threshold	6.0	28	160 ± 1	150	0.85	14.15
1100 ps	1x Threshold	2.1	17	93 ± 3	92	0.17	7.83
	2x Threshold	4.2	23	129 ± 3	130	0.44	10.44
	3x Threshold	6.3	27	151 ± 3	150	0.71	11.17
	5x Threshold	10.5	35	184 ± 2	190	1.29	12.12

5.4.3 Fluorescence Assays and Characterization of the Zones of Cellular Injury

To examine the cellular response to the physical effects of the cavitation bubble dynamics the biological response of the adherent cells, we determined the range and extent of cellular injury and molecular delivery following laser microbeam irradiation using viability and molecular delivery assays. Our particular interest is to achieve precise control over the spatial extent of cellular injury and molecular delivery by varying laser parameters such as laser pulse duration and energy. Therefore we are interested primarily in two zones of cellular injury: (1) the radius of necrotic cells, R_{necr}, which denotes the maximum radius at which cell necrosis is seen and beyond which

cells remain intact and viable, and (2) the maximum radius of permeabilized cells, R_{perm}, which characterizes the spatial extent of cells where uptake of 3 kDa FITC-conjugated dextran detected through standard fluorescence microscopy.

Cell cultures were irradiated with single laser pulses with pulse durations of 180 ps, 540 ps, and 1100 ps at pulse energies of 1x, 2x, 3x, and 5x the threshold energy for plasma formation. Viability assays confirmed that the vast majority of the adherent cells surrounding the irradiation site remained viable for all pulse durations and energies tested. Figure 5.8 provides example phase contrast and epifluorescence images of cells after viability staining using pulse durations at 180 ps and 1100 ps at pulse energies corresponding to 2x the threshold energy for plasma formation. Very few dead cells were observed around the laser irradiation site. Outside the region of cell lysis and detachment, the cells remain adherent and viable. These cells were followed 24 hours post-irradiation to confirm their continued viability and proliferation.
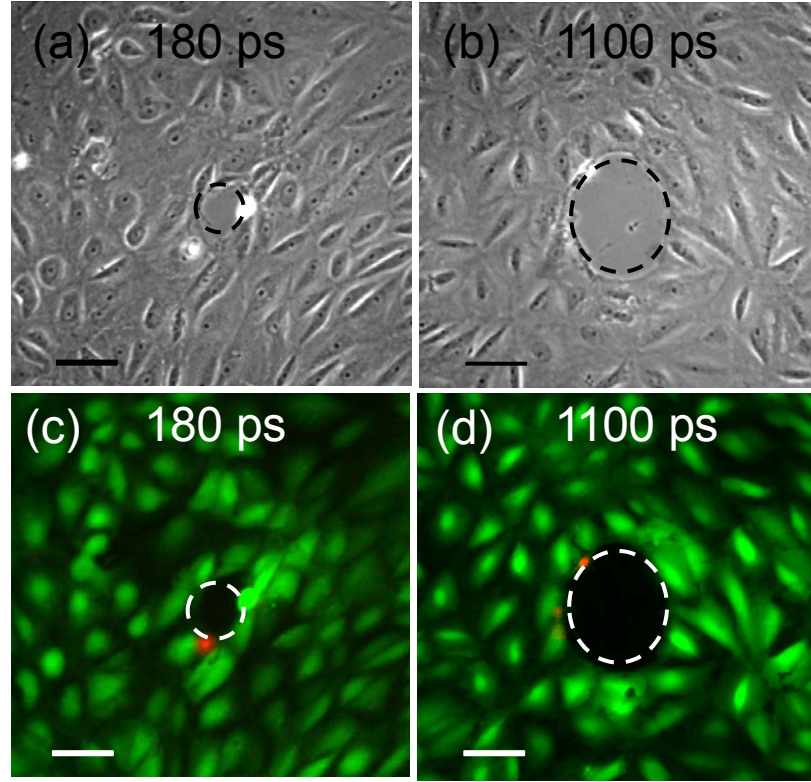
Figure 5.8: Cell viability after irradiation using pulse durations of 180 ps (a, b), and 1100 ps (c, d) at pulse energies corresponding to 2x the threshold energy for plasma formation, i.e. 0.9 μJ for 180 ps (a, c) and 4.2 μJ for 1100 ps (b, d): (a, b) phase contrast image showing the irradiation site and zone of cellular damage (R_{necr}), (c-d) fluorescent images with Calcein AM (green) showing viable cells and Propidium Iodide (red) staining the nuclei of dead cells around the periphery of the irradiation site. Scale bar = 50 μm.

After confirmation that the vast majority of the adherent cells surrounding the irradiation site remain viable, we sought to assess the ability of the laser microbeam irradiation to deliver molecules into the remaining viable cells. Cell cultures were placed in a solution of 3 kDa FITC-conjugated dextran and exposed to a single laser pulse. Figure 5.9 shows phase contrast and fluorescence images demonstrating molecular uptake of dextran after pulsed laser microbeam irradiation using 180 ps, 540 ps, and 1100 ps pulse durations, at $E_p = 2E_{\text{th}}$.
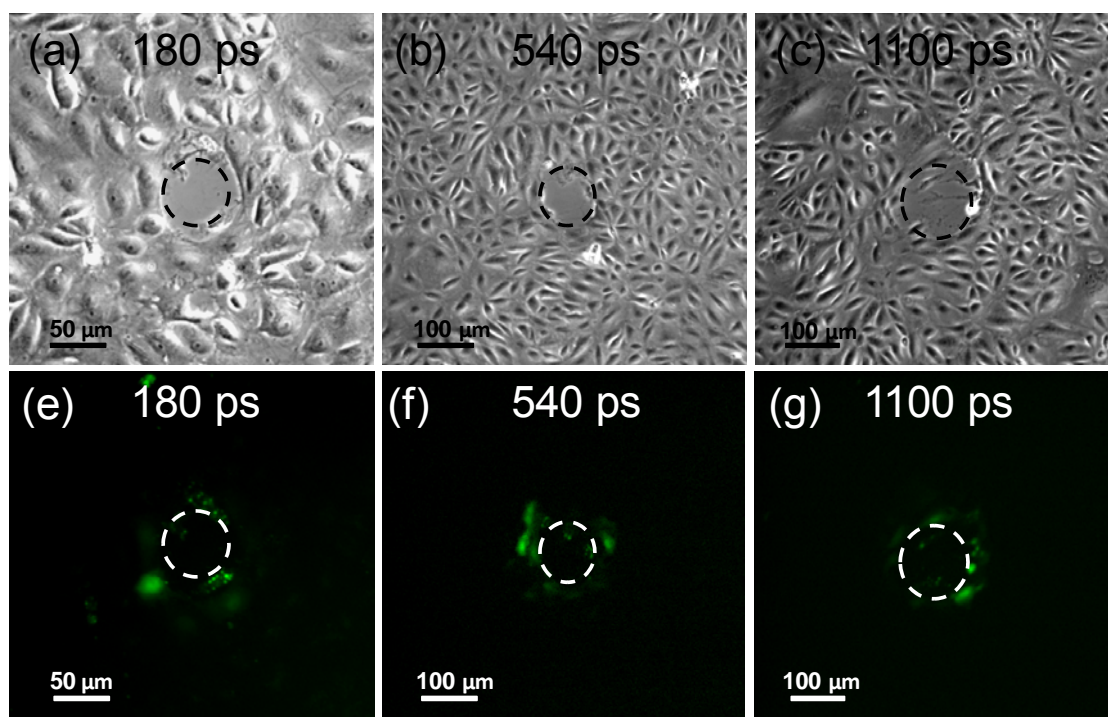
Figure 5.9: Molecular delivery after irradiation using pulse durations of 180 ps (a, d), 540 ps (b, e), and 1100 ps (c, f) at pulse energies corresponding to 2x the threshold energy for plasma formation, i.e. 0.9 µJ for 180 ps (a, d), 2.4 µJ for 540 ps (b, e), and 4.2 µJ for 1100 ps (c, f): (a – c) phase contrast image showing the irradiation site and damage zone, (d – f) fluorescent image showing cells loaded with FITC-dextran (green).

To determine the spatial extent of cell viability and molecular delivery, we measured the average and standard deviation of the locations of R_{necr} and R_{perm} by recording the radius of cellular injury produced at 8-10 irradiation sites. In some instances the zone of cell injury/permeabilization was slightly elliptical. In these cases the radius of a circle of equivalent area was used. The radial dimensions defining the zones of cellular necrosis and permeabilization as a function of pulse duration and pulse energy are shown in Table 5.3. Again we found that for a given pulse duration, the zones of cellular injury increase with pulse energy. Moreover, the reduction in threshold energy with pulse duration provides the ability to better target the delivery.

An interesting observation of this study is that for all pulse durations and energy combinations tested, the measured maximum bubble radius, R_{max}, is contained within the standard deviation of the measured radius of cell membrane permeabilization, R_{perm}.

Table 5.3: Laser pulse energy (E_p), radius of cell death (R_{necr})*,* radius of permeabilized cells (R_{perm}), and the maximum cavitation bubble radius (R_{max}) when irradiating cell cultures with a cell surface density of 1000 cells/mm^2 at pulse energies corresponding to 1x, 2x, 3x, and 5x the threshold for plasma formation at varying pulse durations.

Pulse Duration t_p		E_p [μJ]	R_{necr} [μm]	R_{perm} [μm]	Bubble R_{max} [μm]
180 ps	1x Threshold	0.45	35 ± 5	50 ± 6	44 ± 1.5
	2x Threshold	0.90	46 ± 4	64 ± 9	71 ± 2.1
	3x Threshold	1.35	51 ± 5	82 ± 8	87 ± 1.5
	5x Threshold	2.25	69 ± 7	103 ± 9	109 ± 2.1
540 ps	1x Threshold	0.96	43 ± 4	72 ± 11	79 ± 4.6
	2x Threshold	1.92	57 ± 5	109 ± 12	107 ± 1.6
	3x Threshold	2.88	66 ± 5	135 ± 8	129 ± 3.6
	5x Threshold	4.80	87 ± 7	159 ± 13	160 ± 1.1
1100 ps	1x Threshold	1.2	51 ± 5	86 ± 11	93 ± 2.7
	2x Threshold	2.4	80 ± 6	137 ± 14	129 ± 2.5
	3x Threshold	3.6	89 ± 6	143 ± 12	151 ± 3.3
	5x Threshold	6.0	115 ± 8	176 ± 9	184 ± 1.8

5.5 Analysis and Discussion

Our objectives in this study are three-fold. First, we aim to establish the relationship between the physical effects of the energy deposition of laser microbeam pulses of varying pulse duration and energy. Second, we seek to determine the relationship between the selected laser microbeam parameters and the subsequent cellular biological response. Third, we will examine how variation in laser microbeam parameters can be used to 'modulate' the relative sizes of the regions of cell lysis and molecular delivery.

5.5.1 Hydrodynamic Model for Cavitation Bubble Expansion

We previously reported that for 6 ns laser microbeam pulses focused immediately above the cell monolayer (10 μm), the primary agent for cell lysis, deformation, and injury is the dynamic shear stress produced by the fluid displacement associated with the cavitation bubble expansion [93, 94]. Hydrodynamic analysis from time-resolved imaging studies revealed that the maximum wall shear stress governs the location and spatial extent of cellular necrosis as well as the extent of molecular delivery, independent of laser pulse energy. In addition, we investigated cavitation bubble-induced optoporation and identified a well-defined range of maximum wall shear stress required to achieve molecular delivery to adherent cells [44]. Here we present a summary of this model and apply it to investigate if the cavitation bubble-induced flow is the primary agent for cell necrosis and molecular delivery.

We have utilized a hydrodynamic model (detailed description in Section 3.4.4 and 4.5.1) to determine the spatio-temporal evolution of both the fluid velocity and the wall shear stress produced by the cavitation bubble dynamics resulting from picosecond laser microbeam pulses. Our time-resolved imaging results provided a means to quantify the spatial and temporal evolution of both the radial position $R_B(t)$ and velocity $V_B(t)$ of the bubble wall. The radial position of the bubble wall during the cavitation bubble expansion was fit to the function $R_B(t) = [a + (b/\ln t)]^2$ with $R_B(t)$ representing the bubble radius as a function of time and a and b being the fit parameters. This analytic expression was found to fit all the data series with regression coefficients greater than 0.99 (Table Curve, Systat Software, Richmond, CA). The raw data and curve fit is shown in Figure 5.10, Figure 5.11, and Figure 5.12 for 180 ps, 540 ps, and

1100 ps, respectively. Velocity of the cavitation bubble expansion was determined by differentiation of the analytic curve fit for each pulse duration and energy, also shown. It is seen that the maximum bubble expansion increased with laser pulse duration and energy. Conservation of mass in this system provides the following relationship between the external fluid velocity $V_\infty(r,t)$ and the bubble dynamics as:

$$V_\infty(r,t) = V_B(t) \left[\frac{R_B(t)}{r} \right]^2 \tag{5.1}$$

Conservation of momentum was then applied to obtain the following expression for the wall shear stress $\tau_w(r,t)$ generated by the cavitation bubble expansion [94]:

$$\tau_w(r,t) = \rho \sqrt{\frac{\nu}{\pi}} \int_0^t \frac{\partial V_\infty(r,t')}{\partial t'} \frac{dt'}{\sqrt{t-t'}}, \tag{5.2}$$

where ρ and ν are the density and kinematic viscosity of the fluid medium [94]. Equation (5.2) is valid at any radial position r and time $0 < t \le t'$ where t' is the time of arrival of the bubble wall at position r.
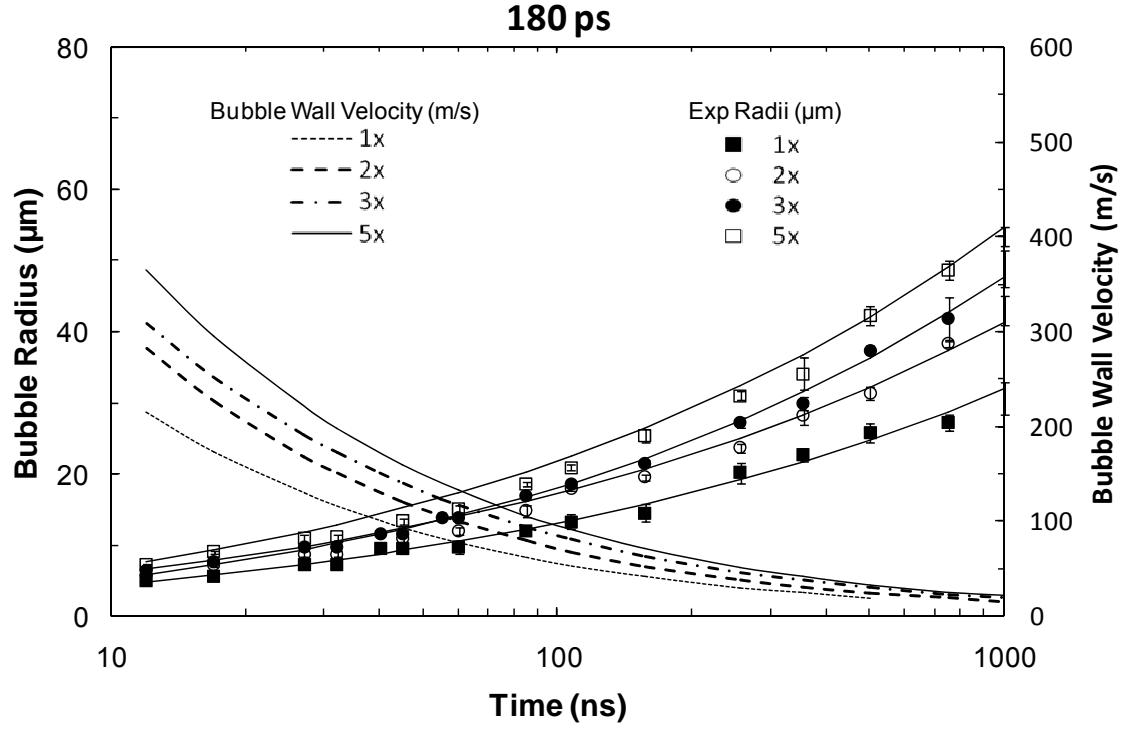
Figure 5.10: Time evolution of the cavitation bubble wall position $R_B(t)$ and velocity $V_B(t)$ determined from time-resolved images of the laser microbeam irradiation using 180 ps pulses at pulse energies corresponding to 1x, 2x, 3x, and 5x the threshold energy for plasma formation.
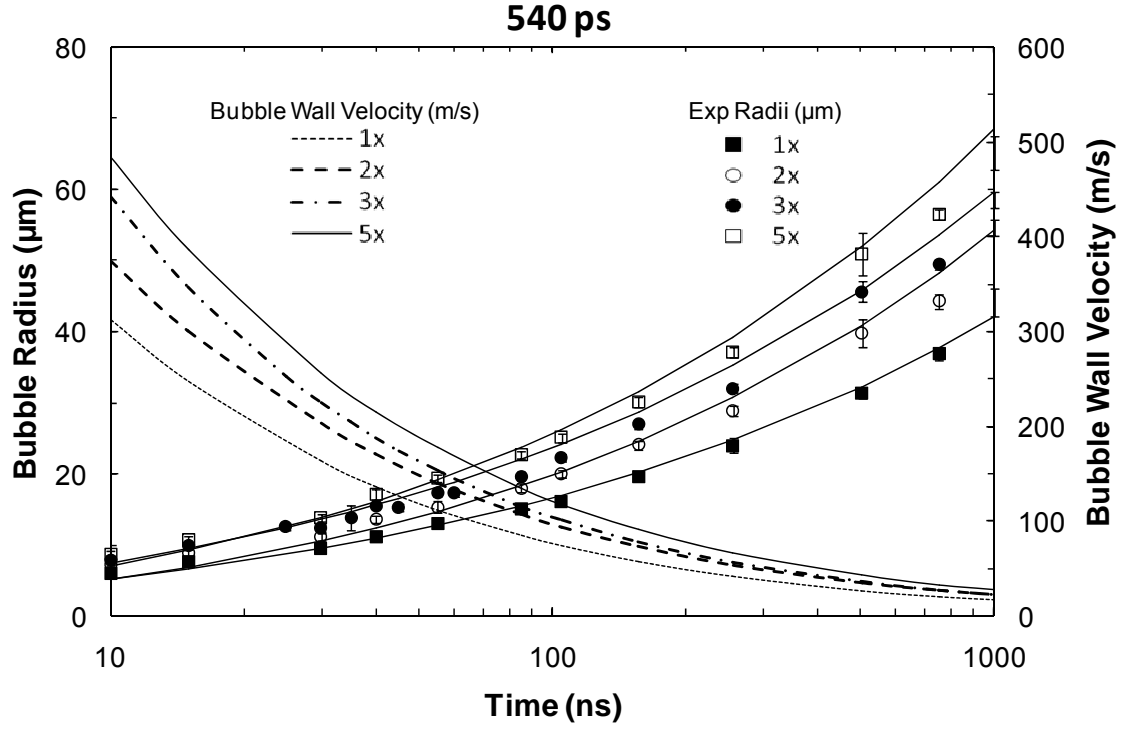
Figure 5.11: Time evolution of the cavitation bubble wall position $R_B(t)$ and velocity $V_B(t)$ determined from time-resolved images of the laser microbeam irradiation using 540 ps pulses at pulse energies corresponding to 1x, 2x, 3x, and 5x the threshold energy for plasma formation.
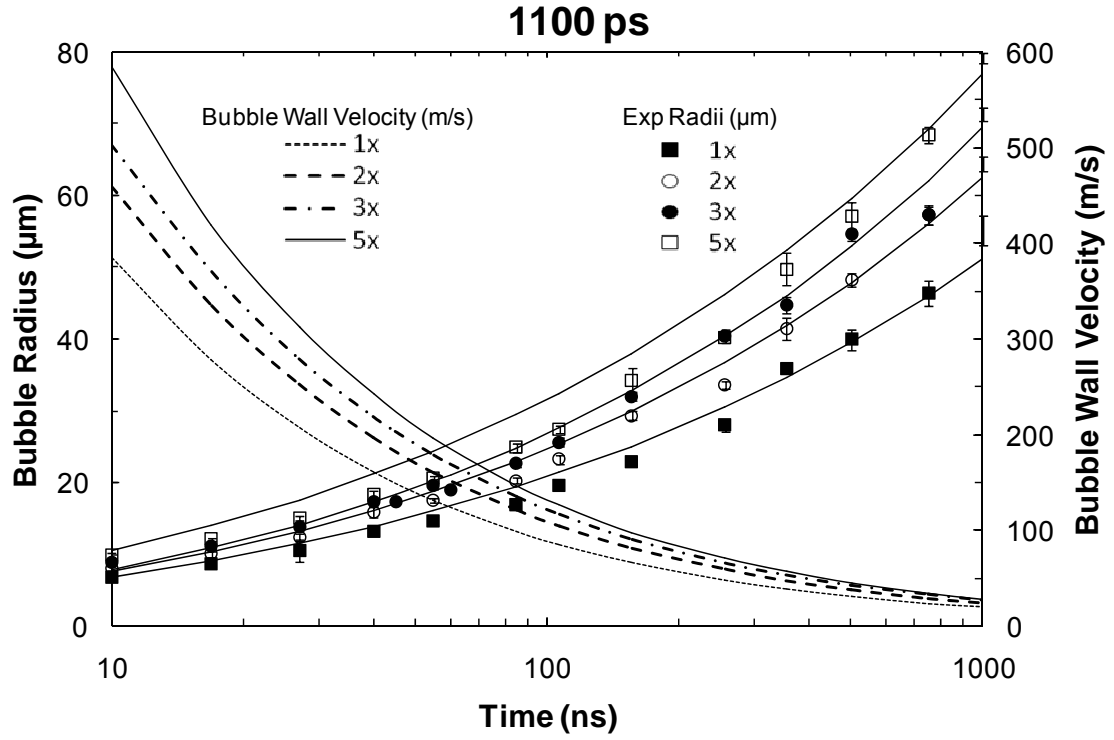
Figure 5.12: Time evolution of the cavitation bubble wall position $R_B(t)$ and velocity $V_B(t)$ determined from time-resolved images of the laser microbeam irradiation using 1100 ps pulses at pulse energies corresponding to 1x, 2x, 3x, and 5x the threshold energy for plasma formation.

5.5.2 Impact of Cavitation Bubble-Induced Shear Stress on Cellular Injury and Molecular Delivery

The profiles of the temporal evolution of the wall shear stress are characterized generally by a rapid ($\leq$ 30 ns) increase to a maximum value followed by a more gradual decay [94]. Of particular interest is the maximum shear stress at radial positions corresponding to the regions of cell necrosis and cell membrane permeabilization. Table 5.4 provides the maximum wall shear stress predicted by our hydrodynamic analysis at the interface of these two regions, i.e., at $r = R_{necr}$ and $r = R_{perm}$. This table encompasses pulse durations of 180 ps, 540 ps, and 1100 ps at energies corresponding to 1x, 2x, 3x, and 5x the threshold energy for plasma formation, resulting in energy ranges of 0.45 μJ – 10.5 μJ. Remarkably, even with wide range of pulse energies examined for each pulse duration, the range of shear stresses calculated at each zone of cellular injury is quite narrow within a given pulse duration. The location representing the maximum extent of necrotic cells ($r = R_{necr}$) is exposed to shear stresses of $\tau_{w,max} > 26 \pm 2$ kPa for 180 ps pulses, $\tau_{w,max} > 33 \pm 4$ kPa for 540 ps pulses, and $\tau_{w,max} > 34 \pm 6$ kPa for 1100 ps pulses. The analysis also indicates that the molecular delivery to these cells with a 3 kDa FITC-conjugated Dextran through transient membrane permeabilization ($r = R_{perm}$) requires a maximum shear stress of $\tau_{w,max} > 12 \pm 1$ kPa for 180 ps pulses, $\tau_{w,max} > 9 \pm 1$ kPa for 540 ps pulses, and $\tau_{w,max} > 13 \pm 2$ kPa for 1100 ps pulses. Cells exposed to shear stresses lower than those reported for $r = R_{perm}$ remain viable and appear unaffected by the pulsed laser microbeam irradiation.

Table 5.4: Summary of hydrodynamic data and analysis providing the maximum wall shear stress $\tau_{w,max}$ computed at R_{necr} and R_{perm} for 180 ps, 540 ps, and 1100 ps at energies corresponding to 1x, 2x, 3x, and 5x the threshold for plasma formation. The mean and standard deviation $\tau_{w,max}$ for each pulse duration are also shown.

Pulse Duration, t_p		E_p [μJ]	Maximum wall shear stress $\tau_{w,max}$ [kPa] @ $r = R_{necr}$	@ $r = R_{perm}$
180 ps	1x Threshold	0.45	23 ± 7	11 ± 3
	2x Threshold	0.90	26 ± 5	14 ± 4
	3x Threshold	1.35	28 ± 6	11 ± 2
	5x Threshold	2.25	27 ± 6	12 ± 2
Mean ± SD			**26 ± 2**	**12 ± 1**
540 ps	1x Threshold	1.2	31 ± 6	11 ± 2
	2x Threshold	2.4	33 ± 6	9 ± 2
	3x Threshold	3.6	38 ± 6	9 ± 1
	5x Threshold	6.0	28 ± 5	8 ± 1
Mean ± SD			**33 ± 4**	**9 ± 1**
1100 ps	1x Threshold	2.1	44 ± 9	16 ± 4
	2x Threshold	4.2	29 ± 4	10 ± 2
	3x Threshold	6.3	30 ± 4	12 ± 3
	5x Threshold	10.5	31 ± 4	13 ± 1
Mean ± SD			**34 ± 6**	**13 ± 2**

Figure 5.13 illustrates the interrelationship between the spatial region occupied by the necrotic, optoporated, and unaffected viable cells and the maximum transient shear stress for 180 ps, 540 ps and 1100 ps laser pulse durations at varying pulse energy. The curves represent the predictions of the hydrodynamic model for the maximum wall shear stress as a function of radial position for each laser microbeam pulse energy. The shaded regions are defined by the range of shear stresses necessary for the laser microbeam to produce the appropriate cellular effect. The intersection of an individual curve with each shaded region defines the range of maximum wall shear stress and radial positions in which the various cellular effects are achieved for the given pulse energy. The location of the experimental data points is remarkably consistent with the boundaries of the shaded regions.
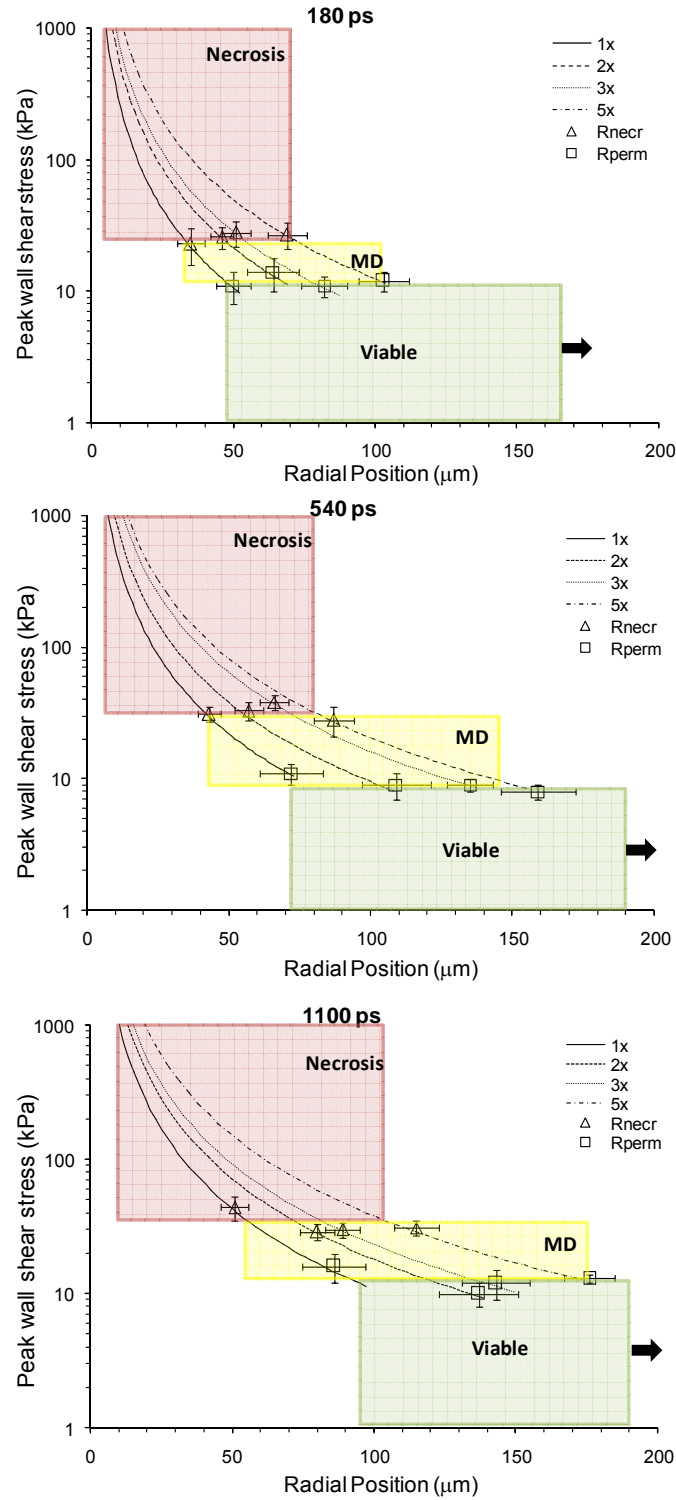
Figure 5.13: Hydrodynamic model predictions of the maximum wall shear stress $\tau_{w,max}$ for pulse durations of 180 ps, 540 ps, and 1100 ps at energies corresponding to 1x, 2x, 3x, and 5x the threshold for plasma formation. Colored regions indicate the resulting cellular effect: necrotic, molecular delivery (MD) and viable.

5.5.3 Modulation of Extent of Cellular Injury and Molecular Delivery By Varying Pulse Duration

The use of shorter pulse durations provides the ability to produce plasmas at smaller pulse energies and create cellular modifications with greater spatial precision and specificity, as demonstrated in Table 5.3. In addition, it is well known that a change in pulse duration also affects how the energy of the plasma is dissipated amongst the various pathways, e.g. plasma luminescence, vaporization, shock wave energy, bubble energy, etc. For this reason, we wish to explore if variation of pulse laser microbeam duration can be used to modulate the relative amount of cell necrosis or molecular delivery.

In Table 5.5, we list the pulse energy, bubble energy, and ratio of bubble energy to pulse energy for 180 ps, 540 ps, and 1100 ps. We also provide an estimate for the number of necrotic and optoporated cells by taking the product of the area of cell injury or permeabilization and the cell surface density of 1000 cells/mm^2. Collectively, the results demonstrate that increases in pulse energy at each pulse duration produces substantial increases in both the zones of cellular damage and the number of permeabilized cells. To determine if there is exists an 'optimal' optoporation pulse duration which achieves maximum molecular delivery and minimal cell necrosis, we examined the ratio of permeabilized cells to necrotic cells for each of the laser parameters examined, as shown in the last column of Table 5.5. We found 540 ps to be the most favorable pulse duration to achieve this, providing the maximum ratio of permeabilized to necrotic cells for all pulse energies tested. At this pulse duration, the ratio of the calculated number of permeabilized cells to necrotic cells was as high as

3.11 for a pulse energy of 3x threshold (Table 5.5). Figure 5.14 illustrates the mechanical transduction efficiency (i.e. the percentage of laser pulse energy converted to bubble energy) across all pulse durations examined for pulse energies of 1x, 2x, 3x, and 5x the threshold energy for plasma formation. At all pulse energies tested, 540 ps provides the highest mechanical transduction efficiency. The higher bubble energy at this pulse duration may be a contributing factor to the higher spatial extent of permeabilized cells.

Table 5.5: Laser pulse energy (E_p), mechanical bubble energy (E_B), mechanical transduction efficiency (E_B/E_p). number of necrotic cells, number of permeabilized cells, and the ratio of permeabilized cells to necrotic cells for pulse durations of 180 ps, 540 ps, and 1100 ps at energies corresponding to 1x, 2x, 3x, and 5x the threshold for plasma formation.

Pulse Duration t_p		E_p [μJ]	E_B [μJ]	E_B/E_p [%]	# Necr. Cells	# Perm. Cells	# Perm/ #Necr
180 ps	1x Threshold	0.45	0.02	3.92	4 ± 1	4 ± 2	0.98
	2x Threshold	0.90	0.07	8.24	7 ± 1	6 ± 4	0.96
	3x Threshold	1.35	0.14	10.11	8 ± 2	13 ± 4	1.53
	5x Threshold	2.25	0.27	11.93	15 ± 3	18 ± 7	1.24
540 ps	1x Threshold	0.96	0.07	7.09	6 ± 1	10 ± 5	1.81
	2x Threshold	1.92	0.16	8.40	10 ± 2	27 ± 8	2.68
	3x Threshold	2.88	0.28	9.84	14 ± 2	43 ± 7	3.11
	5x Threshold	4.80	0.56	11.59	24 ± 4	55 ± 13	2.32
1100 ps	1x Threshold	1.2	0.10	8.51	8 ± 2	15 ± 6	1.82
	2x Threshold	2.4	0.25	10.58	20 ± 3	39 ± 12	1.96
	3x Threshold	3.6	0.44	12.36	25 ± 4	40 ± 11	1.59
	5x Threshold	6.0	0.85	14.15	42 ± 6	56 ± 12	1.35
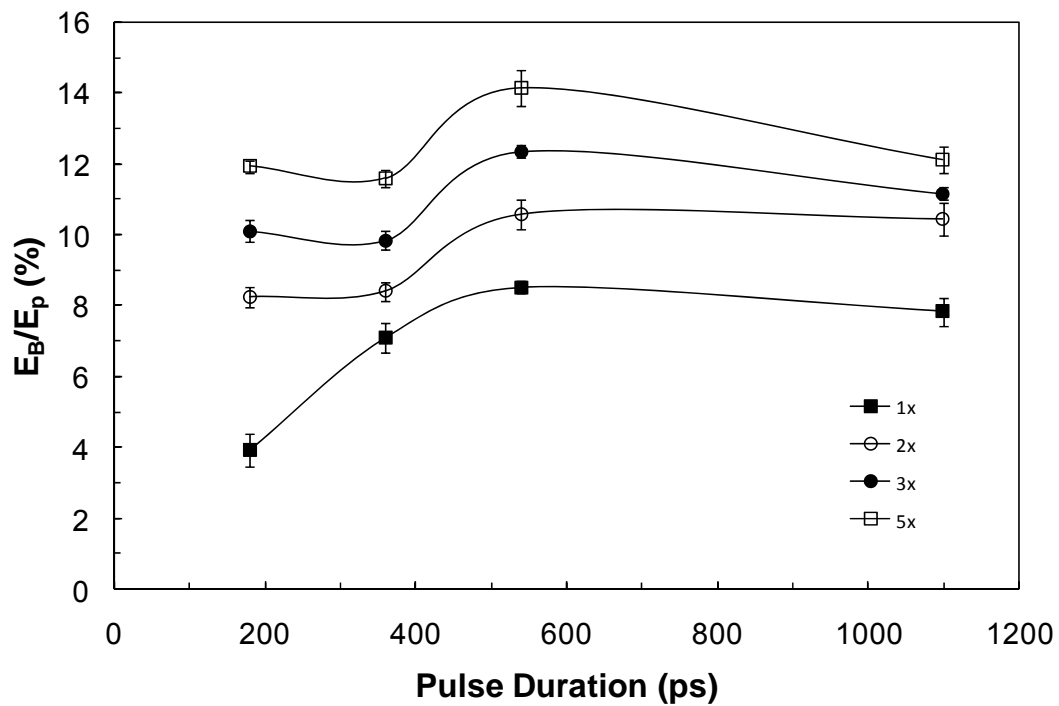
Figure 5.14: Mechanical transduction efficiency of pulse energy transferred to cavitation bubble energy (E_B/E_p) for 180 ps, 360 ps, 540 ps, and 1100 ps at energies corresponding to 1x, 2x, 3x, and 5x the threshold for plasma formation. A pulse duration of 540 ps achieves the highest mechanical transduction efficiency.

5.6   Conclusion

We have examined the effects of pulse duration and energy on the cellular response to laser microbeam pulses produced by pulsed laser microbeam irradiation at $\lambda = 532$ nm in PtK$_2$ cell monolayers cultured at a density of 1000 cells/mm^2. Time resolved imaging was used to characterize the physical dynamics laser-microbeam interactions with cells for pulse durations ranging from 180 ps to 1100 ps and energies from 0.45 µJ to 10.5 µJ. Fluorescence viability and membrane permeability assays were used to assess the cellular response and spatial extent of resulting cell necrosis and membrane permeability. The reduction in pulse duration provides the ability to generate a plasma at smaller energies, thereby greatly improving the spatial precision and specificity of the pulsed laser microbeam effects. Moreover, the variation of pulse duration allows for modulation of the relative of cellular damage versus molecular delivery. This may be useful for some applications where molecular delivery is favored over cell lysis. As was found when using 6 ns pulses, the peak wall shear stresses produced by cavitation bubble expansion was seen to be the primary agent for cell necrosis and molecular delivery via transient permeabilization of the cell membrane in viable cells when using picosecond pulses. We have defined a narrow range of shear stress required for molecular delivery into this cell type at this surface density.

5.7   Acknowledgements

of California System-wide Biotechnology Research and Education Program (UC BREP)

GREAT Training Grant #2006-12.

Chapter 6

LASER MICROBEAMS AS TOOLS TO STUDY

BIOCHEMICAL PATHWAYS IN-VITRO

6.1   Introduction

Thus far in this dissertation, we have evaluated the cellular response to laser microbeam irradiation with viability and molecular delivery assays using standard fluorescence microscopy techniques. We have characterized the physical interaction of cavitation bubble expansion with the cell monolayer and have deemed the cells beyond the observed permeabilized region as 'unaffected'. However, conventional microscopy techniques are insufficient to determine if the cells are in fact truly unaffected. It is of interest to determine if the cellular biochemical activity is modified in response to the stress from laser microbeam irradiation. It has been shown that laser microbeam irradiation can induce a stress response in cells, such as spikes in calcium signaling [48, 107]. In this chapter, we will determine if the fluid shear resulting from cavitation bubble expansion) is capable of stimulating biochemical pathways.

The study of cellular response to mechanical stimuli has advanced greatly with the availability of molecular probes to facilitate measurements of cell signaling [16]. The type of stress stimuli, as well as its level of intensity, can induce responses within

both the targeted cell and neighboring cells. This diverse set of responses can range from electrophysiological modulation of membrane proteins, cellular reorganization, signal transduction cascades, and activation of transcription factors. Often, a response to stress stimuli can have important roles in the pathogenesis of a disease. Thus, there is a strong interest in the field of cellular manipulation to discover stress response elements. However, many questions remain as to how cells sense mechanical stimuli and transmit them into intracellular biochemical signals. Current techniques to induce a stress response to live cells, such as laser tweezers [16] and flow chambers [3, 70], are very bulky and slow, with a limited ability for high throughput cell screening.

Laser microbeam-induced cavitation provides a fast, non-contact means to create transient localized shear stresses to nearby cells. In previous chapters we have characterized laser-generated cavitation bubble dynamics in fluid media, providing spatially and temporally resolved shear stress distributions resulting from cavitation bubble expansion. Hydrodynamic analysis of the cavitation bubble dynamics revealed that cells surrounding the site of laser irradiation are subject to high (relative to physiological values) transient shear stresses on the nanosecond to microsecond time scales. The use of laser-generated cavitation bubbles to induce a stress response in cells is a promising technique for evaluating activity of mechanical transduction pathways for high throughput cell screening/sorting with applications in disease diagnostics and therapeutics.

In this section we validate the method of using laser-generated cavitation bubbles to induce a stress response in a cell sample by demonstrating the ability to successfully activate a cellular biochemical pathway in response to mechanical stress.

The Src kinase has been shown to be a key player in the transduction of mechanical stimuli from the extracellular environment into the cell via cell adhesion and focal adhesion complexes [35]. Here we use a Förster resonance energy transfer (FRET)-based biosensor capable of detecting Src kinase activation.

6.2   Description of FRET and the Src Kinase Biosensor

In the fields of molecular biology and fluorescence microscopy, FRET is a useful tool to quantify molecular dynamics such as protein-protein interactions and protein conformational changes in live cells with high spatial and temporal resolution [103, 122]. FRET occurs between two fluorophores if they are in close proximity and if the emission spectrum of the donor fluorophore sufficiently overlaps the excitation spectrum of the acceptor fluorophore [16]. Any change in the distance and/or relative orientation between the two fluorophores can affect the efficiency of FRET and the resulting ratio of fluorescence emission by the acceptor and donor.

A FRET-based biosensor capable of detecting Src kinase activation has been used in this proof-of-principle experiment. This genetically encoded biosensor is a Src substrate peptide with cyan and yellow fluorescent proteins (CFP and YFP) attached in close proximity to yield a high FRET signal. Upon Src phosphorylation, the CFP and YFP are separated, thus decreasing the FRET signal (Figure 6.1). This Src biosensor has been shown to specifically report Src activation *in vitro* [121, 137].

Figure 6.1: (a) Schematic representation of the Src reporter. The cartoon illustrates the FRET effect of the Src reporter upon the actions of Src kinase or phosphatase. (b) Emission spectra of the Src reporter before (black) and after (red) phosphorylation by Src. (Adapted from Wang YX, *et. al., Nature,* 434 (7036) 1040-1045, 2005) [137].

6.3   Materials and Methods

6.3.1   Cell Irradiation

Figure 6.2 shows the current setup for achieving cellular manipulations using a pulsed laser. The cell sample is placed on the stage of an inverted Zeiss Axiovert S100 microscope. An Nd:YAG laser pulse (λ = 532 nm, E_p = 1 – 10.5 μJ) is focused at a location 10 μm above the cell monolayer. A bright-field objective (40x, 0.8 NA,

Achroplan, Zeiss) was used for cell irradiation. The cavitation bubble generated by the laser pulse expands and collapses, exposing the cells to a transient shear stress surrounding the site of laser irradiation.
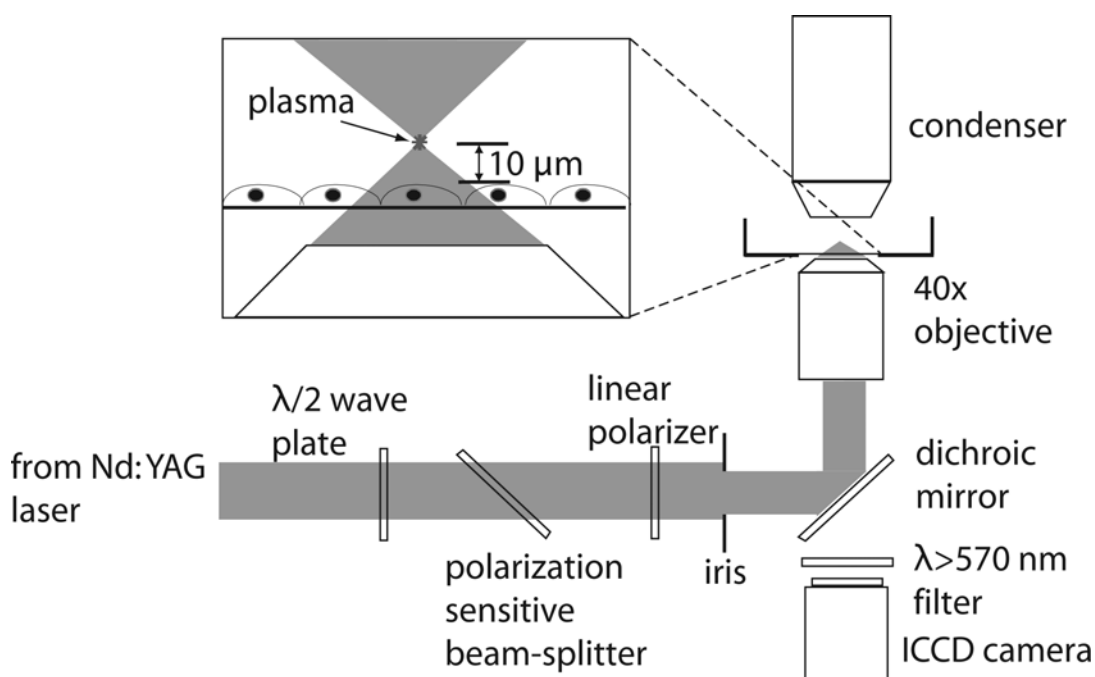
Figure 6.2: Setup for cellular manipulations using laser-generated cavitation.

6.3.2   Cell Culture

Bovine aortic endothelial cells (BAEC) were cultured using standard cell culture techniques and grown to 80% confluence in polystyrene culture dishes with glass bottoms in Advanced DMEM with Glutamax (Invitrogen) and transfected with the Src reporter using Fugene 6 (Roche).

6.3.3   Fluorescence Imaging of FRET

Cells were imaged in bright-field and trans-fluorescence both before and after (within 2 minutes) of the laser pulse delivery to the cell sample. For trans-fluresccence imaging, the fluorescence lamp was mounted on the microscope condenser with a CFP excitation filter in front, and both CFP and YFP emission filters (Chroma Technology Corp.) were placed in the microscope filter cube. A Quantix CCD camera (Photometrics, Roper Scientific, Trenton, NJ) was used for the trans-fluorescence and bright-field imaging, using a 40x, 0.8 NA (Zeiss Achroplan, Jena, Germany) objective. Camera operation and image acquisition was performed using V++ imaging software (Photometrics, Roper Scientific, Trenton, NJ).

6.3.4   Image Analysis

Image processing was conducted in Matlab and the CFP/YFP intensity ratio was computed to determine the FRET signal. Matlab code developed by Dr. Elliot Botvinick at the University of California, San Diego was used, and has been described in detail in literature [16]. The following procedures were applied: extraction of the CFP and YFP subimages from the raw image, pixel registration between the two subimages, extraction of the cell from the background, subtraction of the background signal, and calculation of the ratio image.

6.4   Results

We found a decrease in the FRET signal (i.e. an increase in the CFP/YFP ratio), indicating the activation of Src, in cells following the laser pulse at distances up to

1 mm away from the site of laser irradiation when using a pulse duration of 1100 ps and a pulse energy of 10.5 µJ. Examples are shown in Figure 6.3 and Figure 6.4. A definite increase in intensity of the ratio of CFP to YFP emission can be seen after the laser pulse was fired, indicating activation of the Src kinase and a biochemical response to the cavitation bubble-induced shear stress.
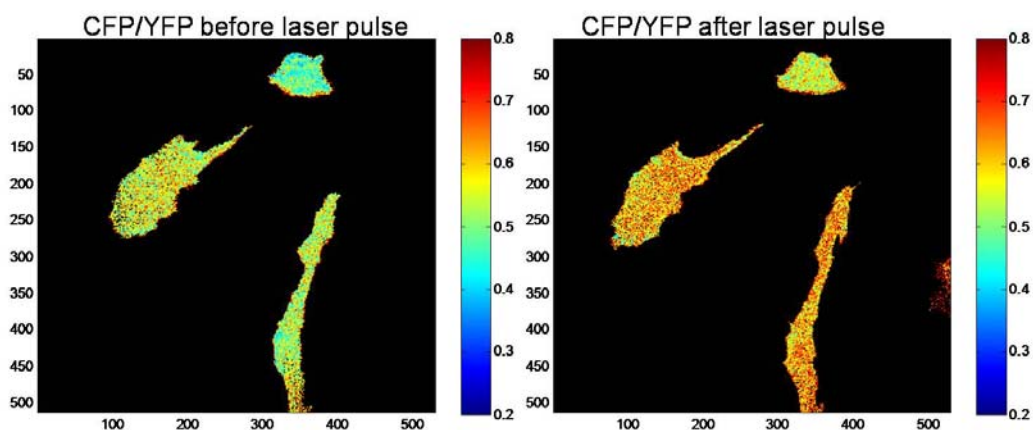
Figure 6.3: Images showing the ratio of CFP/YFP emission of cells positioned 740 microns away from the site of laser irradiation before and after a 10.5 µJ, 1100 ps pulse.
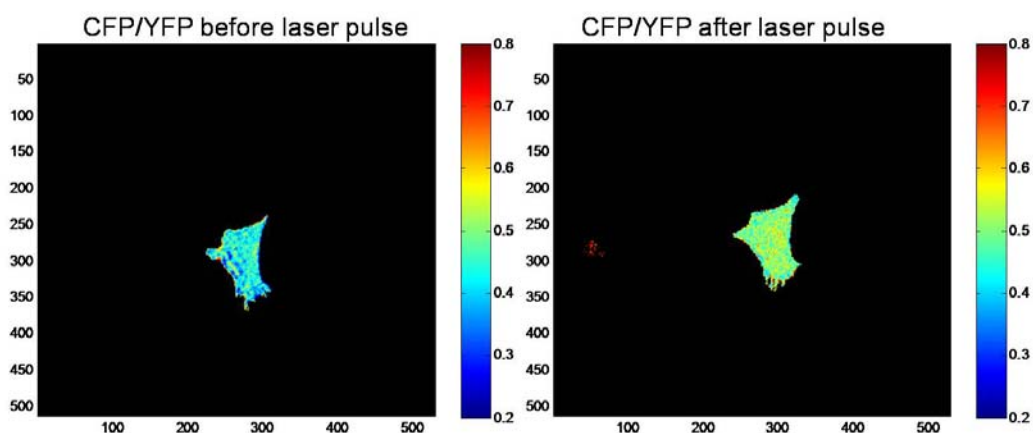
Figure 6.4: Images showing the ratio of CFP/YFP emission of cells positioned 200 microns away from the site of laser irradiation before and after a 10.5 µJ, 1100 ps pulse.

This technique holds great promise as a non-contact, non-chemical means for inducing a stress response in cells to evaluate the activity of biochemical pathways for high throughput cell screening/sorting for applications in molecular imaging, disease diagnostics, and therapeutics.

6.5   Acknowledgements

Chapter 7

APPLICATIONS FOR PULSED LASER MICROBEAMS IN MICROFLUIDIC DEVICES

7.1   Introduction

Microfluidic devices have emerged as effective platforms for the manipulation and analysis of small sample volumes and the integration of multiple processes for lab-on-a-chip (LOC) experiments.   The integration of pulsed laser microbeams with microfluidic devices is particularly advantageous for LOC applications to achieve the manipulation of cells and fluids within a microfluidic environment [43, 91].   One particular advantage is that pulsed laser microbeam irradiation does not require the incorporation of any specialized on-chip instrumentation.   This greatly reduces the design complexity and cost of the individual microdevice, thereby making it economical to dispose of the LOC device after single-use.   Rather, one must invest in a laser platform and a microscope objective to deliver the laser radiation into the microdevice. Second, the laser microbeam can be directed to any optically-accessible location within the microdevice.   This provides tremendous flexibility with respect to the timing and location of cell/fluid manipulation; enabling potentially the parallelization of cellular analysis at multiple device locations.

In this chapter, we demonstrate three examples of the use of laser microbeams for manipulation within microfluidic devices. Based on our understanding of laser microbeam processes we have tailored the microbeam parameters (i.e. pulse duration and energy) to achieve the desired effect. First, we demonstrate the use of nanosecond and picosecond laser pulses to achieve targeted lysis of non-adherent cells for cellular analytics. Second, we utilize picosecond pulses to provide precise localized damage of neuronal axons for the study of central nervous system neuronal injury and regeneration. Lastly, we discuss the ability of laser microbeams to provide localized mixing of two fluid streams within the confines of a microfluidic device that may provide a means to subject cells to a transient or repeated exposure of a chemical agonist.

7.2   Targeted Single Cell Lysis in Microfluidic Channels

Our laboratory, in conjunction with the Allbritton group, has been working towards the use of laser microbeams to facilitate single cell analysis via electrophoresis on a LOC device [91]. Studies utilizing 6 ns pulses to achieve cell lysis within a microfluidic channel posed substantial challenges due to the cavitation bubble size. Time-resolved imaging studies have shown that in a confluent cell culture, the optical lysis event from a 6 nanosecond laser pulse is accompanied by the formation of a cavitation bubble whose maximum size is roughly 300 μm in diameter [93, 94]. Cavitation bubbles of this size may pose problems in a microfluidic channel because fluid equivalent to the volume of the bubble must be displaced. Even though these bubbles expand and collapse within microseconds, they may damage or otherwise elicit a biochemical response in neighboring cells resident on the device. Furthermore, the

expanding cavitation bubble deforms the polymeric walls of the microfluidic channel. Figure 7.1 provides and image taken using our time-resolved imaging system of cavitation bubble formation within a 50μm channel at 275 ns after delivery of single laser pulse. One cell was lysed while its neighbor remained intact, and the intracellular contents can be seen jetting out. The deformation of the polymeric walls caused by the cavitation bubble expansion is also seen. This demonstrates the ability of a laser microbeam system to create damage with high spatial specificity as well as the impact of secondary effects caused by cavitation bubble dynamics in confined volumes.
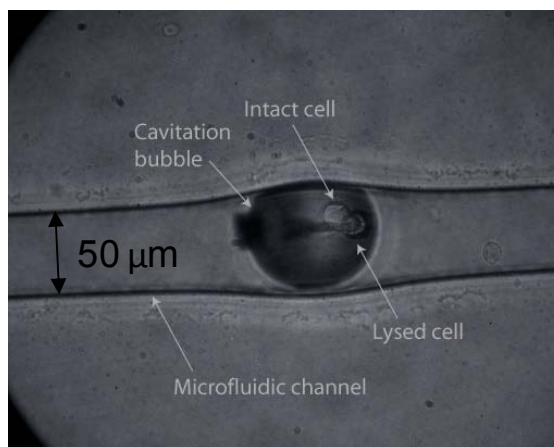
Figure 7.1: Laser microbeam induced cell lysis within a 50 μm wide microfluidic channel 275 ns after the delivery of one 6 ns, 20 μJ laser pulse. The targeted cell was lysed with its neighbor remaining intact. Cavitation bubble expansion also caused deformation of the silicone microfluidic channel walls.

These results, combined with our study of the impact of pulse duration on laser microbeam irradiation (Chapter 5), motivated us to move to shorter pulse durations to provide more localized cell lysis. Another study in our laboratory utilized 540 ps pulses and fluorescent time-resolved imaging to visualize the cell contents during the cell lysis process [91]. Figure 7.2 provides a series of time-resolved fluorescence images that

depict the interaction of a single BAF-3 cell (loaded with CellTracker^{TM} dye) with the laser-induced cavitation bubble. At 16 ns we see that the light emission from the plasma produced by the pulsed laser microbeam irradiation excites the fluorescence of the cell and makes the cell very bright. At 31 ns the outline of the bubble is clearly visible because during its expansion it compresses the cell against the top and side walls of the microchannel and the fluorescent contents have already started to be released from the cell. At 95 ns and 239 ns time delays, the cell appears to have been lysed completely and the fluorescent cytosol has been dispersed around the entire periphery of the bubble as well as almost the entire length of the microfluidic channel within the field of view.
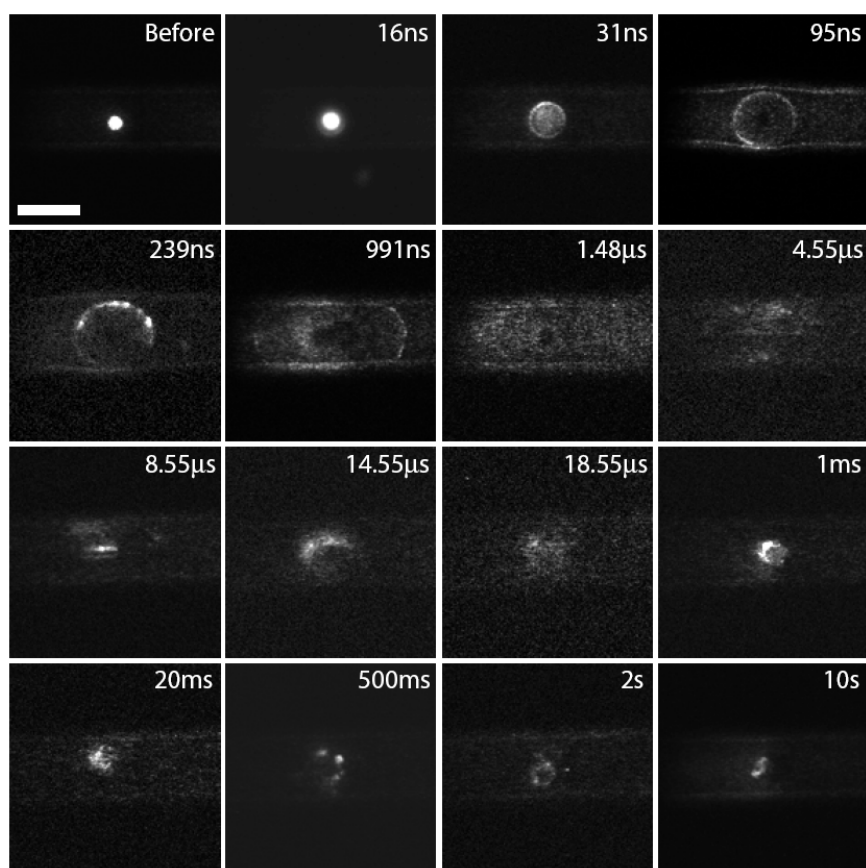
Figure 7.2: Fluorescent cell lysis dynamics inside the microfluidic chip. Fluorescent images of the laser-microbeam cell lysis process inside the microfluidic channel on time scales spanning 9 orders of magnitude. Adapted from Quinto-Su et. al. *Lab on a Chip* 2008 [91]. Scale bar = 50 μm.

The initial release and dispersion of the cell contents occurs on the sub-microsecond time scale. This characteristic of pulsed laser microbeam cell lysis makes it a strong candidate for analytical applications where the biochemical dynamics of the analyte of interest is very rapid. Another positive characteristic of the pulsed laser microbeam cell lysis process is that while the initial dispersion and dilution of the cell contents is significant, the fluid flow associated with the cavitation bubble collapse relocalizes the cell contents with minimal dilution. This re-localization of the cell contents is consistent with the present understanding of cavitation bubble dynamics in

microfluidic channels. The end effect is that the cellular biochemical reactions are effectively terminated on the millisecond time scale. These characteristics are particularly advantageous for subsequent analysis or manipulation of the cellular constituents. Given the relative ease with which optical methods can be integrated with microfluidic devices, we expect that the use of pulsed laser microbeam cell lysis may provide a power method for a broad variety of lab-on-chip applications.

7.3   Localized Neuronal Injury to Study CNS Regeneration

Here we demonstrate another application for targeted cellular manipulation in microfluidic devices to study central nervous system (CNS) injury and regeneration. Spinal cord injury is a challenging field of study, in part because simple and reproducible *in vitro* models do not currently exist. Instead, researchers must perform time-consuming and technically demanding studies *in vivo* that preclude the rapid, high-throughput screening of compounds of interest. More recently, microfluidic approaches are being increasingly used in a variety of neuroscience applications [87, 88]. The Jeon Lab at the University of California, Irvine has developed a novel microfabricated, multi-compartment neuronal culture chamber for neuroscience research using microfabrication and soft lithography techniques [118, 119]. This chamber allows active control and fluidic isolation of neuronal microenvironments, and may result in new avenues of research for neurodegenerative diseases. Additionally, this chamber can be coupled with substrate patterning to direct the sites of neuronal attachment, orientation, and length of neurite outgrowth. Compared to conventional assays, the microfluidic device is easy to use, yields reproducible results (>90%), is compatible with long-term

culture of CNS neurons, and allows reproducible severing of neurons, otherwise known as axotomy.
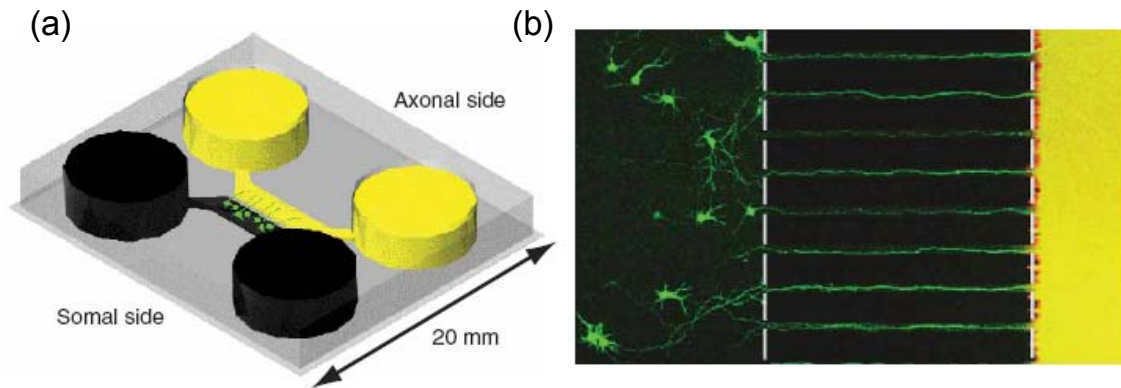
Figure 7.3: The microfluidic-based culture platform directs axonal growth of CNS neurons and fluidically isolates axons. (a) Schematic of the culture platform showing the somal and axonal compartments connected by microgrooves (10 μm wide, 3 μm high). (b) Rat CNS neurons stained with Cell Tracker Green in the microfluidic device. Adapted from Taylor, et. al. *Nature Methods,* (2)8, 2005 [118].

Axotomy is currently achieved in these devices by applying gentle suction with a laboratory vacuum for 10-15 seconds on the axonal chamber [87]. Due to high fluidic resistance of the microgrooves, only the fluid in axonal chamber is removed. This procedure results in reproducible, unambiguous severing of all the processes in the axonal chamber. Meanwhile, cell bodies and neuritic processes attached in the somal chamber are not affected as they are fluidically isolated from axonal chamber.

Although these devices provide a reproducible way to study neural injury and regeneration in vitro, the current axotomy technique removes all axons on the axonal side of the chamber, making it impossible to compare a severed axon to an intact neighbor within the same device. This situation provides an ideal opportunity to apply

pulsed laser microbeam irradiation as a non-contact means for targeted axotomy of neurons within the device. In Figure 7.4 we provide a proof of principle demonstration where focused a 180 ps, 0.8 µJ laser microbeam pulse on a single axon coming out of the microgrooves in a device. The laser irradiation was used to sever a single axon, while the neighboring axons less than 50 µm away remained intact. Subsequent time-lapse photography allowed monitoring of the axonal regrowth over a 24 hour period.
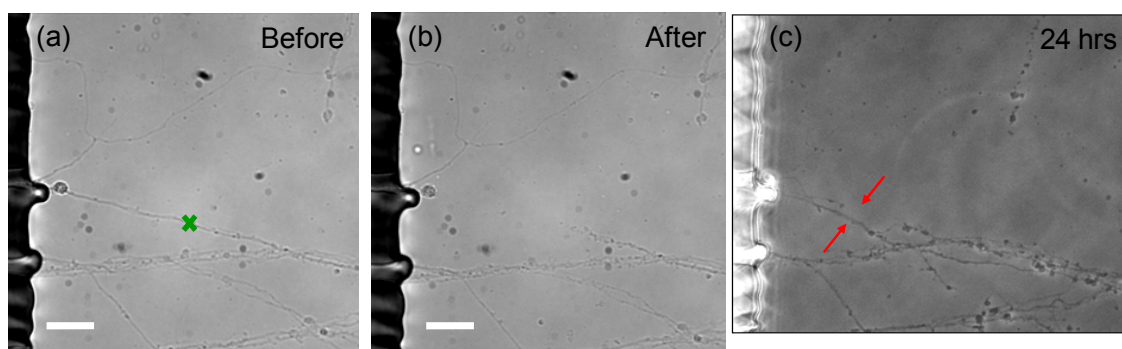
Figure 7.4: Laser microbeam-induced axotomy of rat CNS neurons in a microfluidic device. The microgrooves can be seen in the left of each frame with the axons coming out. (a) Bright-field image with 'x' marking the location of laser microbeam pulse delivery. (b) Bright field image immediately after 180 ps, 0.8 µJ irradiation. (c) Phase contrast image showing axonal regrowth 24 hours post-irradiation. Scale bar = 50 µm.

While the above device is extremely useful in studying CNS regeneration *in vitro*, it does not recapitulate the organized structure of the spinal cord and thus poorly simulates CNS injury. To better mimic axon bundles as they exist *in vivo*, the Jeon group has also developed a microfluidic-based strip assay that utilizes cultures of dissociated neurons to model the organized structure of the spinal cord, such as spatial separation of the axonal extensions from the cell bodies [124]. They have combined micropatterning and microfluidics to selectively place high purity CNS neurons on a favorable substrate but allow only axons to interact with permissive (i.e. polylysine) and

inhibitory substrates (i.e. aggrecan) presented in alternating strips. The resulting microfluidic device provides alternating strips of neuron bundles 25 μm in width.

Pulsed laser microbeams offer a great advantage for performing precise axotomy in these devices. Figure Figure 7.5 provides the result of one such experiment in which a 180 ps, 0.5 μJ laser microbeam pulse was used to irradiate a 25 μm-wide bundle of axons within a microfluidic device. The laser microbeam irradiation resulted in the creation of a lesion less than 25 μm in diameter in the targeted bundle, while the neighboring bundle 25 μm away remained unaffected. Time lapse photography allows monitoring of the axonal retraction and regrowth.
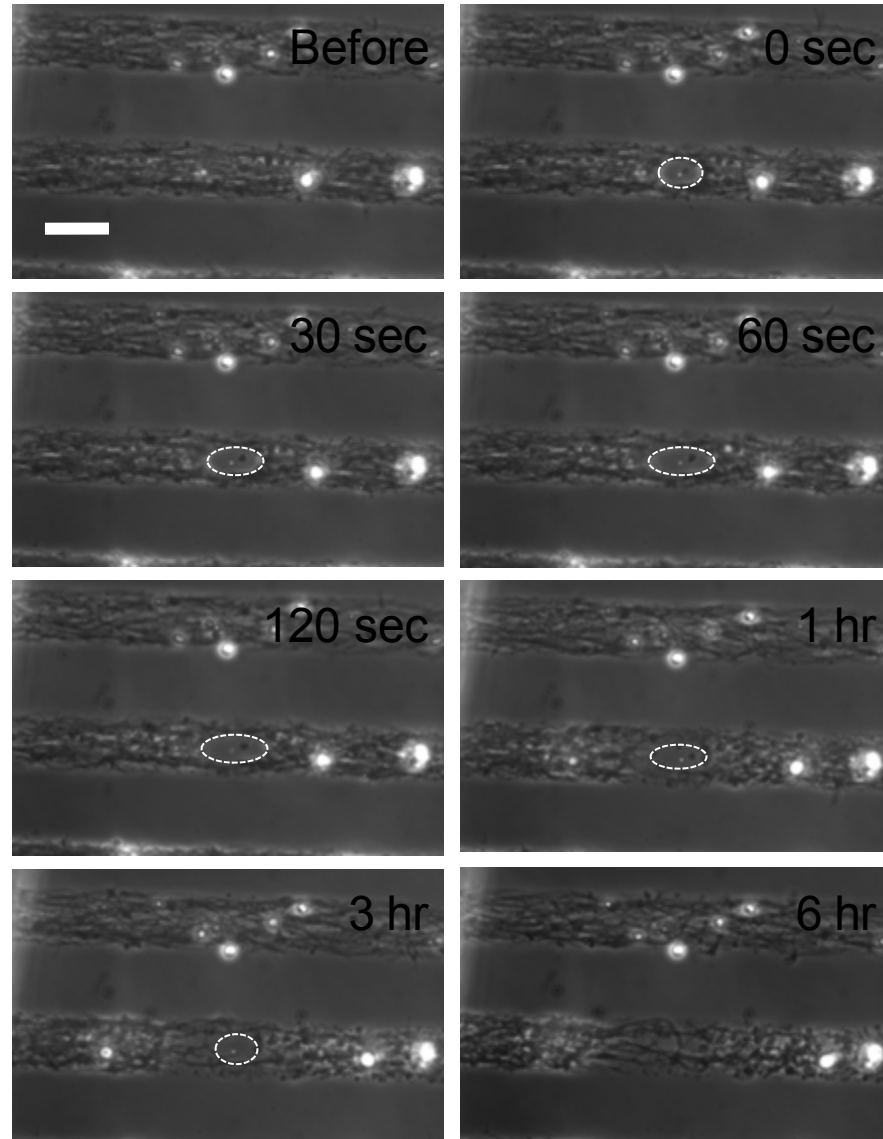
Figure 7.5: Laser axotomy of 25 μm-wide axon bundles within a microfluidic device. A single, 180 ps, 0.5 μJ pulse was focused onto the glass coverslip in the center of the lower bundle, creating a damage zone of less than 25 μm. Size of the damaged area can be monitored over time and axonal regeneration begins within 1 hour after irradiation. After 6 hours, the axons have regenerated across the area of damage. Scale bar = 25 μm.

We employed time-resolved imaging to clearly visualize the cavitation bubble interaction with the axon bundles and determine the mechanism responsible for damage. Figure 7.6 is a time-resolved image series of the shock wave and cavitation bubble dynamics resulting from a 180 ps, 0.5 μJ laser microbeam pulse. In Figure 7.6 (a) and

(b), the shock wave can be seen and quickly passes out of the field of view and does not appear to create any axonal damage. Upon close inspection of Figure 7.6 (d), (e) and (f), it appears that the severing of axons occurs within the first 1 µs. In Figure 7.6 (d), axons can still be seen under the bubble. In Figure 7.6 (e) it appears that there is damage occurring to the axons and in Figure 7.6 (f), no axons can be seen in the center of the bubble, indicating that the axons have been severed. The axon bundles can be seen near the edge of the bubble. This is consistent with our studies of laser microbeam-induced cell lysis that cellular injury occurs during cavitation bubble expansion when the laser microbeam focal volume is focused 10 µm above the cell surface.
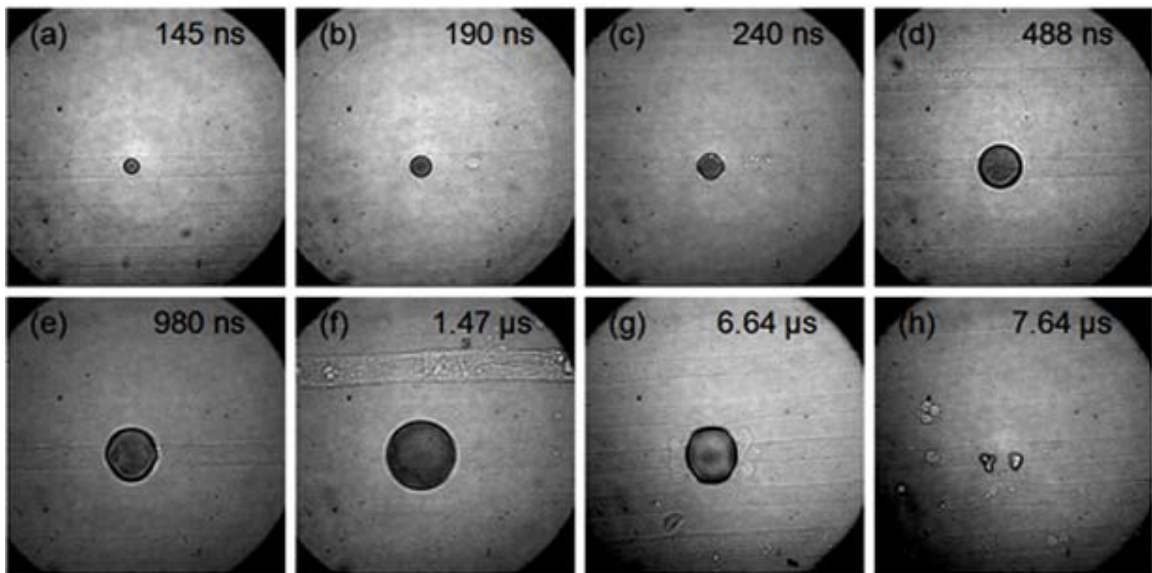
Figure 7.6: Time-resolved image series of laser axotomy of 25-µm-wide bundles following irradiation with a 180 ps, 0.5 µJ laser microbeam pulse.

Through careful selection of the laser parameters, we can modulate the spatial degree of damage within these devices, depending on the specific application. A

similar technique termed 'femtosecond laser nanoaxotomy' is also being used to study nerve regeneration *in vivo*, as other researchers have used 780 nm femtosecond pulses to study nerve regeneration of touch neurons in *C.elegans* [17, 145]. Laser microbeam-based techniques offer a precise surgical tool with variable degrees of spatial specificity to observe and study nerve regeneration both *in vitro* and *in vivo*.

7.4   Laser-Induced Mixing in Microfluidic Channels

Here we introduce a novel strategy for mixing solutions and initiating chemical reactions in microfluidic systems[3]. We utilize nanosecond laser pulses generate cavitation bubbles within 100 μm and 200 μm wide microfluidic channels containing the parallel laminar flow of two fluids. The bubble expansion and subsequent collapse within the channel disrupts the laminar flow of the parallel fluid streams and produces a localized region of mixed fluid. This approach to generate the mixing of adjacent fluids may prove advantageous in many microfluidic applications as it neither requires tailored channel geometries nor the fabrication of specialized on-chip instrumentation.

The challenge of rapidly mixing two fluids within a laminar flow has received considerable attention within the microfluidics community [36, 41, 49, 50, 64, 86, 101]. Microfluidic devices possess characteristic channel widths in the range $W \sim 50$-500 μm

---

[3] Portions of this section have appeared in *Analytical Chemistry*, reference 43. Hellman A, Rau K, Yoon H, Bae S, Palmer J, Phillips K, Allbritton N, Venugopalan V: Laser-induced mixing in microfluidic channels. *Analytical Chemistry* 79:4484-4492, 2007

with volumetric flow rates of $Q \sim$ 50-500 µL/hr resulting in Reynolds numbers of $Re \ll$ 10. The resulting laminar flow admits only diffusion as a mechanism to mix two adjacent fluid streams. The reliance on diffusion alone for the mixing of reactants results in extremely long mixing times and lengths. Specifically, molecular diffusion across a distance of 100 µm requires times of 10-1000 seconds when considering molecules with diffusivities in the range of 10^{-3} -10^{-5} mm/s [83]. This translates into mixing lengths of 0.1-10 m. Such mixing times and lengths are clearly impractical for rapid mixing of small volumes. Thus microfluidic devices that aim to provide rapid kinetic biochemical analysis cannot rely on diffusion alone to mix reagents. Several articles have considered in detail these issues pertaining to flow and transport at the microscale [46, 83, 85, 111].

The limitations posed by diffusion-based transport have spurred researchers to develop various strategies to rapidly mix small volumes in microfluidic devices. Generally these strategies either employ changes in channel geometry (static mixers) or introduce external energy sources (active mixers) to enhance fluid contact and/or de-stabilize the laminar flow [20]. In static mixers, the simplest design modifications are to increase channel length and tortuosity to increase fluid contact time and enhance diffusion. The use of hydrodynamic focusing to achieve reductions in both the flow cross-section and molecular diffusion time has also been described [57, 102, 110]. Such hydrodynamic focusing strategies have provided mixing times as rapid as 8 µs [45]. In other areas, researchers have designed static mixers that utilize chaotic advection, a process in which fluid interfaces undergo stretching and folding to achieve higher mixing efficiencies. Mixers that employ chaotic advection can involve complex designs

with three-dimensional microchannels or relief features on the microchannel floor to achieve mixing of two fluid streams [67, 114, 120]. In active mixers, an energy source is used to destabilize the laminar flow. A simple case of this approach utilizes the temporal pulsing of the flow rate of two fluid streams and has been shown to create well-mixed regions within 250 ms in a 200 μm x 120 μm channel at a flow rate of 1.55 μL/s [37]. Designs employing ultrasound [68, 146], electro-osmotic flow [79], dielectrophoresis [31] and magnetic microstirrers [71, 116] have all been examined to mix two fluids within microchannels. Thus a multitude of approaches have been proposed to handle the microfluidic mixing problem. The choice of mixer type is best decided by the specific application and other considerations such as complexity of design and fabrication.

In this report we present a new method to provide rapid, localized mixing of fluids in microfluidic channels on demand. The concept utilizes the delivery of a highly-focused nanosecond laser pulse resulting in plasma formation and subsequent cavitation bubble generation. The three dimensional character of the fluid flow associated with the cavitation dynamics causes two adjacent fluid streams to mix on microsecond to millisecond time scales. This laser-based method of fluid mixing has several important characteristics that differentiate it from those using more conventional active mixing methods such as ultrasound. First, laser-generated cavitation produces a volume of mixed fluid only in the region surrounding the laser focal volume; thereby enabling the production of a locally mixed fluid volume within the microfluidic channel. Second, the focal volume of the laser beam can be moved easily and thus the site of mixing is not fixed at a particular location in the device. Third, the laser delivery can be

easily switched on and off to provide fluid mixing only at specific times in a microfluidic process. Last, since the laser is decoupled from the microfluidic device, this approach provides microfluidic mixing capabilities without requiring any modification to the microfluidic device design or fabrication. Pulsed laser microbeams also offer additional capabilities in a microfluidic context and can provide a multi-functional tool for capabilities such as selective cell lysis [61], fluorescence excitation, and un-caging of photo-excitable compounds [89]. Finally, one can envision new applications wherein the use of an on-demand, localized mixing capability could prove useful, for example, to mix small volumes of two reactants to synthesize small quantities of product.

In this study a highly-focused Q-switched Nd:YAG laser emitting 6 ns duration pulses at λ = 532 nm was used to produce mixing within the parallel flow of two adjacent fluids within a microfluidic channel. The dynamics and extent of mixing were assessed in three studies. First, time-resolved photography was used to visualize the spatio-temporal dynamics of the cavitation-induced mixing at the site of laser pulse delivery on nanosecond to millisecond time scales. Second, a fluorescence detection system was used to examine the spatial extent of the mixed bolus of fluid approximately 7 mm downstream from the site of pulsed laser delivery. Third, fluorescence video microscopy was used to visualize the efficacy of this mixing approach to initiate a biochemical reaction. This was done by establishing the parallel flow of two adjacent fluid streams containing non-fluorescent substrate and catalyst molecules that, when mixed, yield a fluorescent product.

7.4.1   Materials and Methods

7.4.1.1 Microfluidic Device Fabrication

The microfluidic device was fabricated from poly(dimethyl siloxane) (PDMS) using casting techniques. A SU-8 photo-resist layer was spin coated onto a silicon wafer and the desired pattern was etched using standard photolithography techniques. The channel design (shown in the lower left hand corner of Figure 7.7) consisted of two inlets and an outlet in the form of a Y, with channel widths of either 100 or 200 μm and a channel depth of 50 μm. Two-part silicone resin (Sylgard 184, Dow Corning Corp.) was mixed in a 10:1 ratio (PartA:PartB, v/v) and poured over the silicon master, degassed and cured at 70°C for 1 hour. The cured polymer was peeled from the silicon wafer and sealed against a glass coverslip after punching inlet and outlet vias for fluid access.
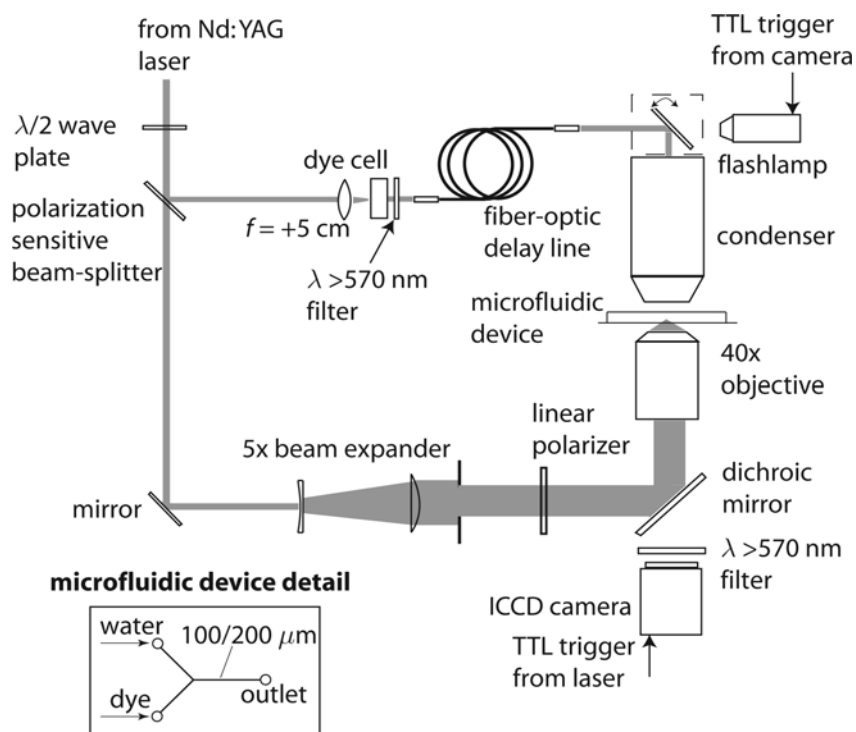
Figure 7.7: Setup for laser-induced mixing and time-resolved imaging.

7.4.1.2 Time-Resolved Bright-Field Imaging of Laser-Induced Mixing

Figure 7.7 is a schematic of the experimental system used in the time-resolved imaging experiments. Fluid was metered into the microfluidic channels using two 100 µL syringes (Gastight No. 81026, Hamilton Co.) connected to the device using Teflon tubing and driven by a syringe pump (Pump 11, Harvard Apparatus). Two fluid streams consisting of water and 8 mg/mL Naphthol Green Dye (Sigma), were supplied from separate syringes each at a flow rate of 50 µL/hr into individual channels of 100 or 200 µm width. The flow rate of 100 µL/hr resulted in mean flow velocities of 2.8 and 5.6 mm/s in channels of 200 µm and 100 µm width, respectively.

The microfluidic device was placed on the sample stage of an inverted microscope (Zeiss Axiovert A110) and the $\lambda = 532$ nm output from a frequency-doubled Q-switched Nd:YAG laser (INDI I-10, Spectra Physics) with a pulse duration of 6 ns was introduced through the fluorescence port into the rear aperture of a microscope objective (Zeiss Acroplan 40x, 0.8 NA or 20x, 0.5 NA). The focal volume of the objective was positioned within the microfluidic channel at the interface between the two parallel fluid streams. Laser pulse energies in the range of 20-25 µJ were employed in all the experiments reported. The laser pulse generated a plasma on the nanosecond time scale resulting in the formation of a cavitation bubble that, upon collapse, produced mixing of the adjacent fluid streams. Mixing dynamics were visualized using a custom-built time-resolved imaging setup that has been described previously [93, 94] and employs the emission from a fluorescent dye cell or an ultra-short duration flashlamp to provide image illumination to the microscope condenser at the desired delay time. A gated intensified CCD camera (PI-MAX, Roper Scientific) was mounted

on the microscope for image capture. The camera gate duration was set to 0.5 ns when using the fluorescent dye cell for illumination and 200 ns when using the flashlamp illumination due to electronic jitter in the flashlamp triggering. Thus, when using the flashlamp illumination i.e., for time delays longer than 3.6 μs, the exposure duration was governed by the 40-ns duration of the flash lamp. WinView software (Roper Scientific) was used to control relevant image acquisition parameters such as gate delay and gate duration as well as coordinating the delivery of the pulsed laser radiation and the image illumination. Differential transmission of the illumination pulse through the water and dye streams generated contrast and allowed these dynamics to be imaged [67]. Adjustments to image brightness and contrast were performed subsequently using Adobe Photoshop (Adobe Systems, Cupertino, CA) as necessary. Each time point was imaged a minimum of three times and representative images are shown in the results.

7.4.1.3 Fluorescence System for Downstream Detection of Mixed Fluid

To examine the dynamics downstream from the site of laser delivery, we utilized the same microfluidic configuration described above but replaced the Naphthol Green dye solution with a solution of 10 μM fluorescein and employed a fluorescence detection system, as shown in Figure 7.8. The two fluids were pumped individually at flow rates of 50 μL/hr through a 200 μm wide channel and brought together at a `Y' junction. To monitor the presence of fluorescent molecules within the channel the output of a continuous-wave Argon ion laser at $\lambda = 488$ nm (2214-10SL, JDS Uniphase) was coupled through a single-mode fiber optic and reflected by a dichroic mirror into the back aperture of a microscope objective (Nikon, 50x, 0.55 NA) that was screwed

into a custom-made filter block. The objective directed the Argon-ion laser beam to the desired location within the microfluidic channel. Any fluorescent emission collected by the microscope objective was directed to a photomultiplier tube (PMT, R928, Hamamatsu Photonics) that was also attached to the filter block. A long-pass filter (LP 500, Edmund Scientific) was used to prevent any Argon ion laser light from reaching the PMT and a 50 μm diameter pinhole was placed in front of the PMT to provide confocal detection. This assembly was mounted on a 3-axis translation stage that was fixed to the microscope stage above the microfluidic device. The translation stage allowed positioning of the detection system at a defined distance downstream from the microscope objective that delivered the pulsed Nd:YAG laser radiation to produce mixing. Moreover, the translation stage provided precise positioning of the focal volume of the Argon ion laser beam at the desired lateral and depth locations within the channel. The fluorescence excitation volume provided by the Argon ion laser was positioned laterally on the `water side' of the channel 20 μm from the channel wall and 80 μm from the water fluorescein interface. This configuration ensured that fluorescence would not be detected when no mixing was accomplished and that appearance of a PMT signal indicated the presence of fluorescein throughout nearly the entire width of the microfluidic channel. The Nd:YAG laser was fired at a repetition rate of 0.4 Hz while the PMT monitored the fluorescence emission at 60 Hz. Custom software routines written in Testpoint (Keithley MetraByte) provided automated control over the delivery of Nd:YAG laser pulses and PMT signal collection.
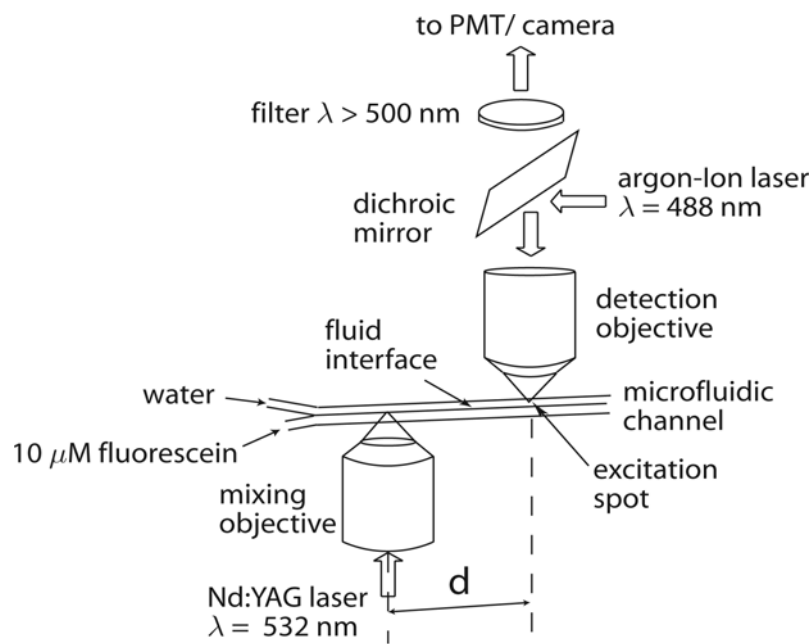
Figure 7.8: Setup for fluorescent system for downstream confocal detection of mixed fluid. The separation distance *d* between the site of mixing and the site of fluorescent detection is approximately 7 mm.

7.4.1.4 Fluorescence Detection of Amplex Red/Horseradish Peroxidase (HRP) Reaction

To demonstrate that the mixing provided by this technique can be utilized to initiate an enzyme-catalyzed biochemical reaction, we imaged the generation of fluorescent resorufin resulting from mixing two non-fluorescent reactant streams, one containing Amplex Red and the other containing horseradish peroxidase (HRP) and hydrogen peroxide (H_2O_2). The two fluids were pumped individually through 100 μm wide channels and brought together at a 'Y' junction. Amplex UltraRed reagent, HRP, and 1M Tris-HCL buffer were acquired from Invitrogen Corporation (Carlsbad, CA). 30% H_2O_2 and dimethyl sulfoxide (DMSO) were acquired from Sigma Chemical Co (St. Louis, MO). All chemicals were reagent-grade quality or better. A 10 mM stock solution of Amplex Red was prepared in DMSO and a 300 units/mL stock solution of

HRP was made using 0.1 M Tris-HCL buffer solution. Immediately prior to use, the stock solutions were diluted in 0.1 M Tris-HCL buffer solution to make one solution containing 250 μM Amplex Red and one solution containing 160 μM H_2O_2 and 1.6 units/mL HRP. Each solution was metered using a 10 μL syringe (Gastight No. 1701, Hamilton, Co.) connected to the device using Teflon tubing and driven by a syringe pump (Pump 11, Harvard Apparatus) at a flow rate setting of 5 μL/hr into a 100 μm channel resulting in a mean flow velocity of 560 μm/s in the main channel.

Bright field and fluorescence images of the enzyme reaction were acquired using the Zeiss Axiovert microscope described above equipped with a 100-W mercury lamp and band-pass filters (λ_{ex} = 540 nm, λ_{em} = 630 nm, Chroma Technology Corp.). The laser was fired to generate mixing, and the production of resorufin was imaged using a digital video camera (Panasonic GP-KR222) and saved using a video cassette recorder (JVC HR-S7800U). Still images at desired time points were captured from the taped recording using Power Director Pro 25ME software (CyberLink USA, Fremont, CA).

7.4.2   Microfluidic Mixing Results and Analysis

7.4.2.1 Time-Resolved Bright-Field Imaging of Laser-Induced Mixing

Delivery of nanosecond Nd:YAG laser pulses focused within the microfluidic channel induced plasma formation in the fluid whose expansion resulted in shock wave propagation and cavitation bubble formation. The plasma formation and shock wave dynamics have been well-studied [93, 126, 129, 132] and here we focus on the cavitation dynamics as it serves as the agent for the observed fluid mixing. Figure 7.9 provides images from our time-resolved photography apparatus depicting the shock wave propagation, cavitation bubble formation, expansion, and collapse at various time points following the delivery of a single 20 μJ laser pulse within the 200 μm channel. The time point is given in each frame and the flow is from viewer's left to right. Figure 7.9 (a) reveals a shock wave resulting from the rapid plasma expansion and cavitation bubble formation. The high pressure within the bubble causes its initial rapid expansion that begins to slow measurably on a timescale of ≤ 100 [129]. The bubble assumes an ellipsoidal shape as its expansion is constrained by the channel walls [Figure 7.9 (c)]. The ellipsoidal bubble reaches a maximum `length' of 240 μm (measured along its longest axis) at a time of 4.4 μs. The maximum volume of the cavitation bubble is estimated as 1.04 nL that corresponds to the volume of an ellipsoid with dimensions of 240, 165, and 50 μm along its three axes.
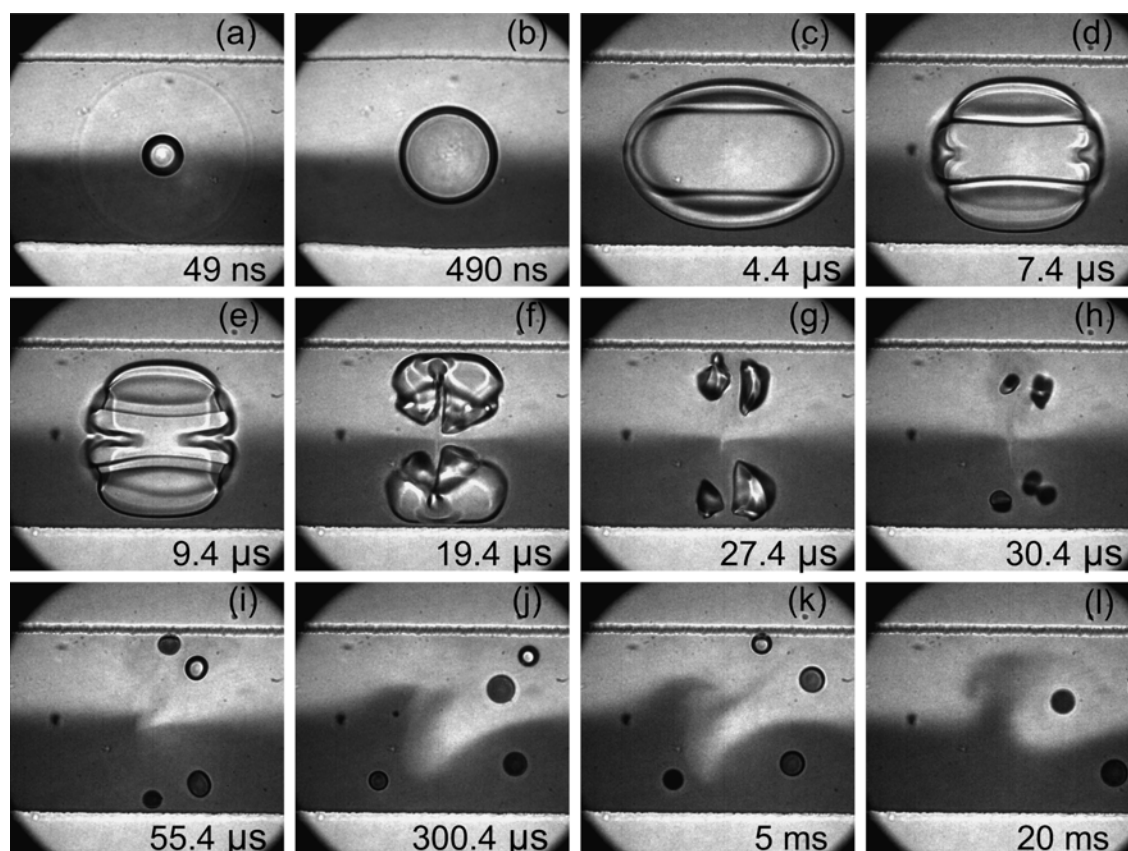
Figure 7.9: Time-resolved image series of cavitation bubble expansion and collapse and subsequent mixing effects produced by a single nanosecond laser pulse in a 200-μm-wide channel.

After reaching its maximum size the bubble collapses rapidly with the reduction in the bubble size occurring faster in the direction parallel with the channel walls. The rapid fluid inflow associated with the bubble collapse results in bubble splitting along the longitudinal axis of the microchannel [Figure 7.9 (d)-(e)] and produces counter-propagating jets towards the channel walls [Figure 7.9 (f)-(h)] that results in a second bubble splitting event and the formation of four very small bubbles that are convected downstream. The appearance of the second bubble splitting event suggests that these jets occupy the full height of the microfluidic channel. These complex bubble dynamics disrupts the smooth interface separating the two fluids mixes the adjacent fluid streams.

Upon bubble collapse, mixing is most evident in the upper part of the channel due to a higher concentration Naphthol Green [Figure 7.9 (h)-(i)]. However, since the bubble collapse is symmetric relative to the interface that initially separates the two fluid streams, one can deduce that the mixing region is also symmetric. At 300 μs, we observe the generation of symmetrical whorls that are formed as a result of the impact of the fluid jet on the channel walls. The spatio-temporal dynamics of the mixing process are remarkably reproducible, demonstrating that laser-generated cavitation bubbles produce consistent well-defined fluid patterns upon collapse within a microfluidic channel. In this case, the mixing zone has a lateral extent of roughly 250 μm that persists for approximately 50 ms after which restoration of the interface between the two adjacent fluids begins and the region of mixed fluid flows downstream and out of the field of view. Since we image the dynamics in one plane the total volume in which this fluid jetting and mixing occurs is unknown. However, by approximating the mixed region as an ellipsoid with dimensions equal to 250 μm x 200 μm x 50 μm we can estimate the mixed volume of fluid to be 1.3 nL.

Figure 7.10 shows the mixing dynamics within a 100 μm wide channel using a laser pulse energy of 25μJ. The ellipsoidal bubble shape is even more elongated due to the smaller channel cross-section and reaches a maximum length of 230 μm [Figure 7.10 (d)]. The stronger confinement offered by the smaller channel reduces the maximum bubble volume even more than that seen in Figure 7.9 even though a higher pulse energy was used to cause plasma formation. Using measured dimensions of 230 μm x 110 μm x 50 μm we calculate a maximum ellipsoidal bubble volume of only

0.6 nL. Another interesting feature is the transient deformation of the channel walls caused by the rapid bubble expansion as seen in Figure 7.10 (c).
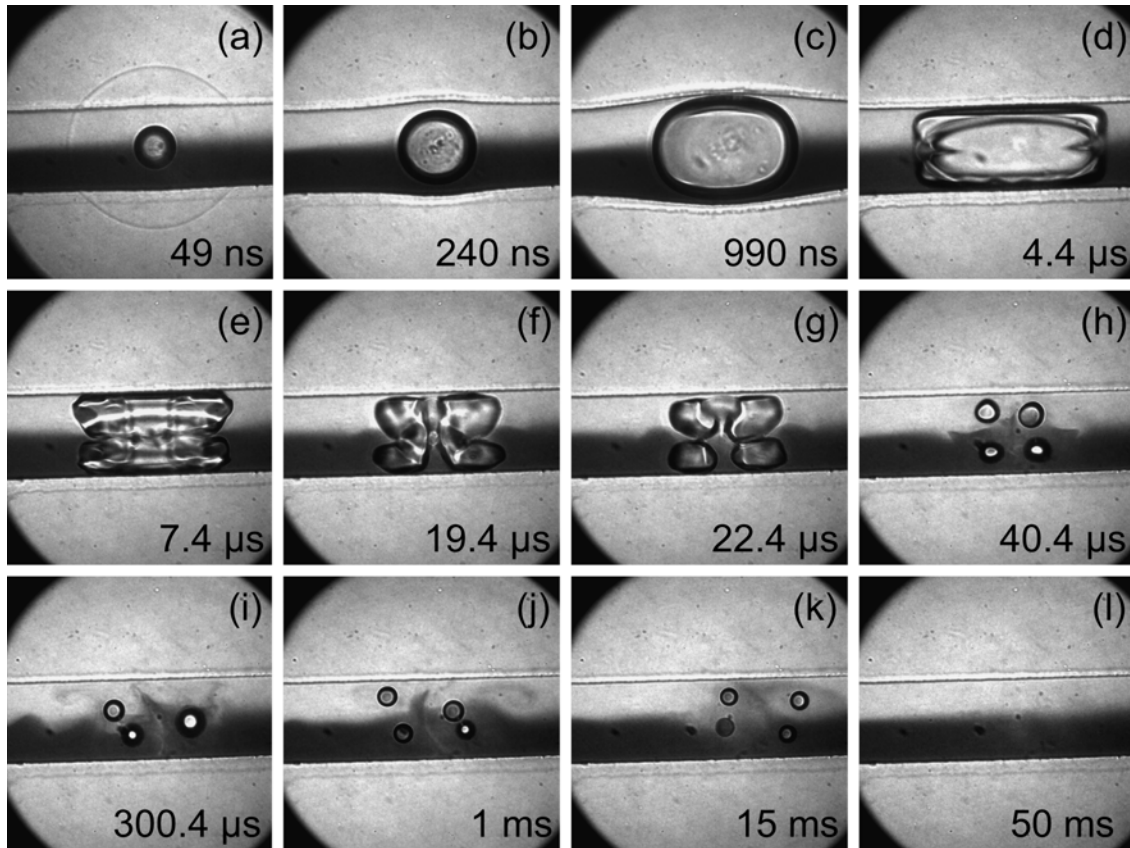
Figure 7.10: Time-resolved image series for cavitation bubble dynamics and mixing within a 100-μm-wide microfluidic channel.

The features of the bubble collapse are slightly different than those seen in Figure 7.9. The narrower channel enhances the speed of the bubble collapse along the longitudinal axis of the channel that again results in complete bubble splitting upon collapse [Figure 7.10 (e) and (f)]. Again, we see counter-propagating jets towards the bubble walls that occupy the full height of the microfluidic channel and results in the second bubble splitting event. The jets produced in the 100 μm wide channel seem to

produce more lateral mixing upon bubble collapse [Figure 7.10 (h)-(k)] than in the 200 μm wide channel. In this case, the mixed region extends laterally for a distance of 200 μm and persists until the interface is restored at 50 ms. Again we see that while the bubble collapse is complete within 50 μs, the mixing dynamics persist for more than 15 ms. Approximating mixed fluid region by an ellipsoid with dimensions 200 μm x 100 μm x 50 μm provides an estimate of 0.52 nL for the mixed fluid volume.

7.4.2.2 Downstream Fluorescence Detection of Mixed Bolus of Fluid

The PMT-based fluorescence detection system was employed to examine the characteristics of the mixed bolus of fluid roughly 7 mm downstream from the region where the Nd:YAG laser pulse was delivered. The focal volume of the Argon-ion laser output used to excite fluorescence was placed at a lateral position in the microfluidic channel where only water was present so long as the parallel laminar flow of the water and fluorescein solution remained undisturbed. Figure 7.11 shows the result of one experimental run using this system. The first pair of traces shown in Figure 7.11 provide signals for the firing of the Nd:YAG laser used to produce the mixing and the measured signal from the PMT when water was supplied to both inlets of the microfluidic device. This shows that the presence of only water in the channel results is no significant PMT signal even when mixing is produced upstream by the firing of the Nd:YAG laser. The second pair of traces show results when one of the water streams is replaced by a 10 μM fluorescein solution. The firing of each Nd:YAG laser pulse results in a spike in the PMT signal indicating the presence of the fluorescein solution on the side of the microfluidic channel where only water is usually present. This result is indicative of the

production of a mixed bolus of fluid that occupies nearly the entire width of the channel and is convected down the channel along with the main flow. Some pulse-to-pulse variation in the peak intensity of the fluorescence signal measured by the PMT is observed. This variation is likely due to the small fluid volume interrogated by the confocal fluorescence detection system and the 60 Hz sampling rate of the PMT signal which may be insufficient to adequately resolve the temporal fluctuations in fluorescent intensity on the microscale.
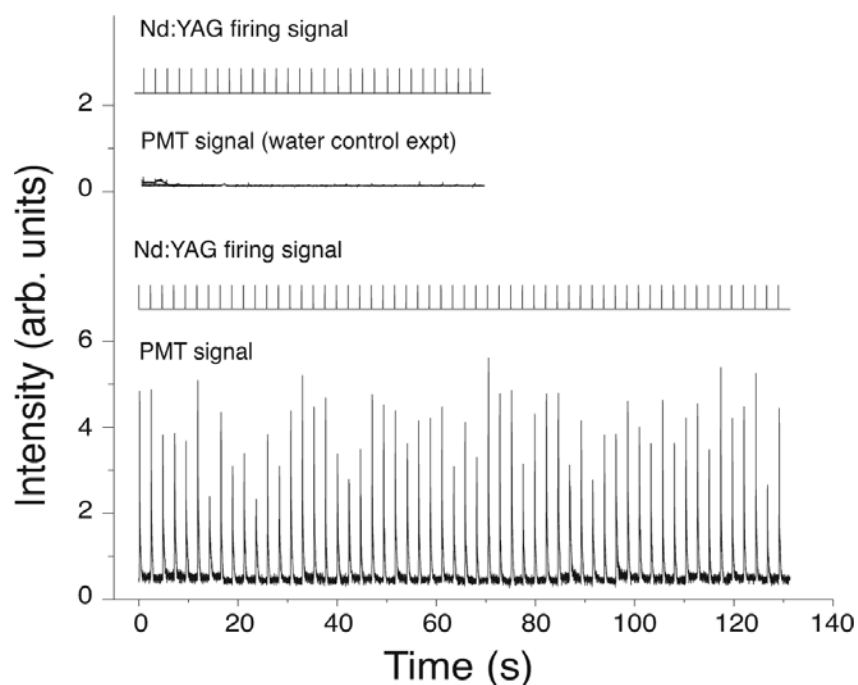
Figure 7.11: Fluorescent detection of mixing effects produced by Nd:YAG laser pulses using the setup shown in Figure 7.8.
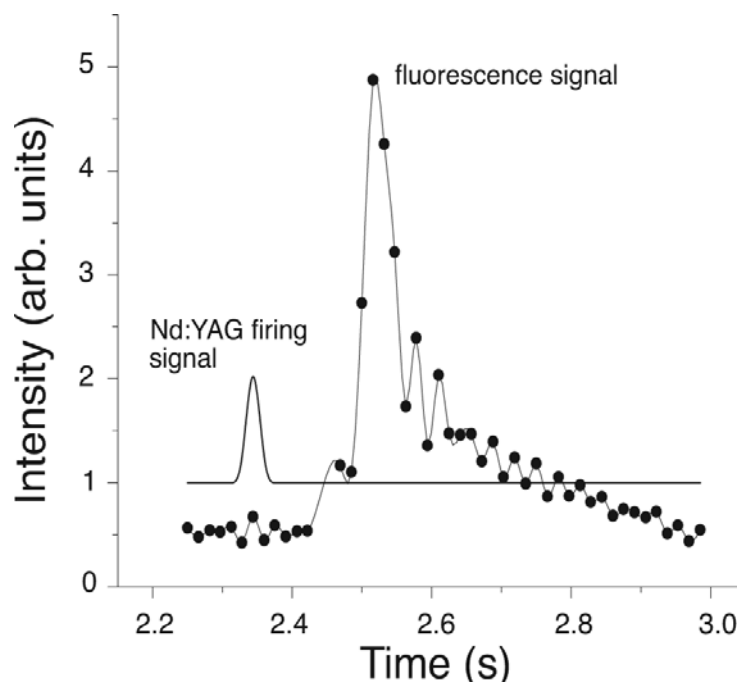
Figure 7.12: Expanded view of one fluorescent signal peak from Figure 7.11 with the corresponding Nd:YAG firing signal.

Figure 7.12 provides an expanded plot of one fluorescence signal peak from Figure 7.11 that follows the firing signal produced by the Nd:YAG laser. The delay of 120 ms between the Nd:YAG firing signal and the increase in the fluorescence signal is not meaningful as it takes several seconds for the bolus of mixed fluid to travel the several millimeters between the site of mixing to the site of fluorescence detection. Thus the fluorescence intensity peak that is detected due to fluid mixing is not produced by the Nd:YAG laser pulse whose firing signal is shown, but by a preceding laser pulse. The width of the fluorescent peak (measured full-width at half maximum) is 70 ms. This indicates that the bulk of the detected fluorescein is concentrated in a bolus of mixed fluid approximately 200 μm in length for the total volumetric flow rate of 100 μL/hr in the 200 μm x 50 μm microfluidic channel. This dimension is roughly consistent with the dimensions of the the mixed bolus of fluid visualized in our time-

resolved imaging experiments. Close examination of the PMT signal immediately surrounding the main peak reveals a `ringing' pattern. This may indicate that a small region is present between the main bolus of mixed fluid and unmixed fluid where there are larger scale fluid structures of fluorescein and water. In this experiment a Nd:YAG laser pulse repetition rate of 0.4 Hz was chosen in order to create a small region of mixed fluid followed by an unmixed region. The duration of the fluorescence peak suggests that continuous mixing within the channel can be achieved by increasing the pulse repetition rate of the Nd:YAG laser to 6 -10 Hz.

7.4.2.3 Fluorescence Imaging of Amplex Red/HRP Reaction

To demonstrate that the laser-induced mixing observed in the time-resolved imaging studies is sufficient to initiate a biochemical reaction within a continuous-flow microfluidic system, we used this technique to initiate the horseradish peroxidase (HRP)-catalyzed reaction between H_2O_2 and Amplex Red. In the presence of HRP, Amplex Red reacts with H_2O_2 in a 1:1 stoichiometry, producing highly fluorescent resorufin [149]. Figure 7.13 (a) is a bright field image at the intersection merging the two non-fluorescent streams: H_2O_2 and HRP in the top stream and amplex red in the bottom stream. Figure 7.13 (b) provides a `background' fluorescence image prior to delivery of the laser pulse. Figure 7.13 (c) provides the fluorescence image at the time of laser pulse delivery ($t = 0$) showing the fluorescence produced by the plasma emission. Figure 7.13 (d) and (e) are fluorescence images taken $t = 0.33$ and 0.5 sec following the laser pulse delivery, respectively. One can easily identify a `bolus' of fluorescence that corresponds to the formation of the reaction product that occupies the

entire width of the channel and is convected downstream by the main flow. Figure 7.13

(f) is the fluorescence image at $t = 2$ seconds following the laser pulse delivery and

bears a strong similarity to Figure 7.13 (b) since the bolus of the fluorescent reaction

product has been convected downstream and out of the field of view. This timescale for

the flow of the reaction product out of the field of view and the re-establishment of

parallel laminar flow is consistent with the mean flow velocity of 560 µm/s.
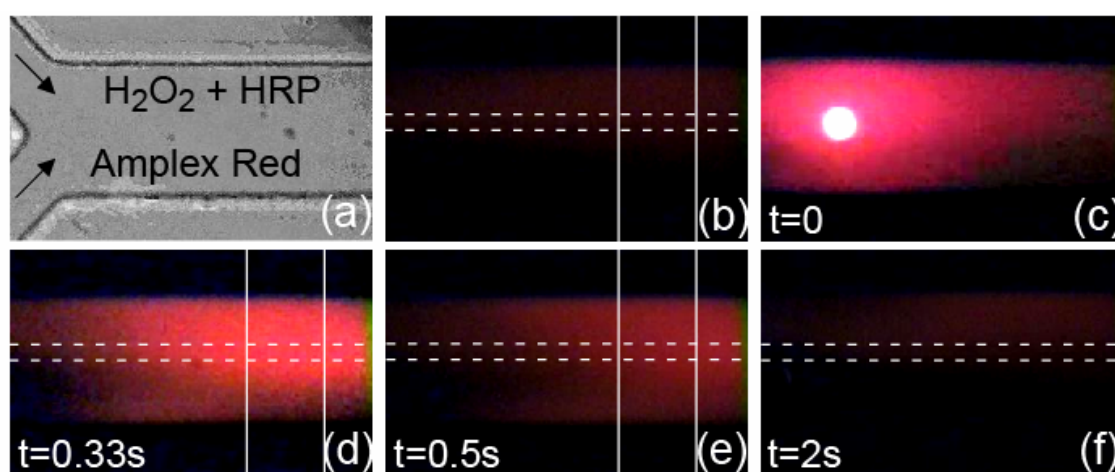
Figure 7.13: Image series demonstrating the production of fluorescent resorufin using the proposed mixing technique to initiate the HRP-catalyzed reaction between Amplex Red and hydrogen peroxide.

To provide a more quantitative assessment of the spatial distribution of the fluorescent reaction product within the channel we provide the spatial distribution of the fluorescent intensities in Figure 7.14. Figure 7.14 (a) is an integrated measure of the fluorescent intensity as a function of *vertical* position within the channel between the two vertical solid lines shown in Figure 7.13 (b), (d), and (e). The fluorescent intensities shown are those determined from Figure 7.13 (d) and (e) normalized against the `background' intensity of Figure 7.13 (b). These traces clearly show that the fluorescent product of the reaction occupies the full width of the channel. Figure 7.14 (b) is an integrated measure of the fluorescent intensity as a function of *horizontal* position along the length of the channel between the two horizontal dashed lines shown in Figure 7.13 (b) and (d)-(f). This figure illustrates the minimal fluorescence intensity before and 2 seconds following the laser delivery as well as the propagation of the reaction product downstream on the sub-second time scale.
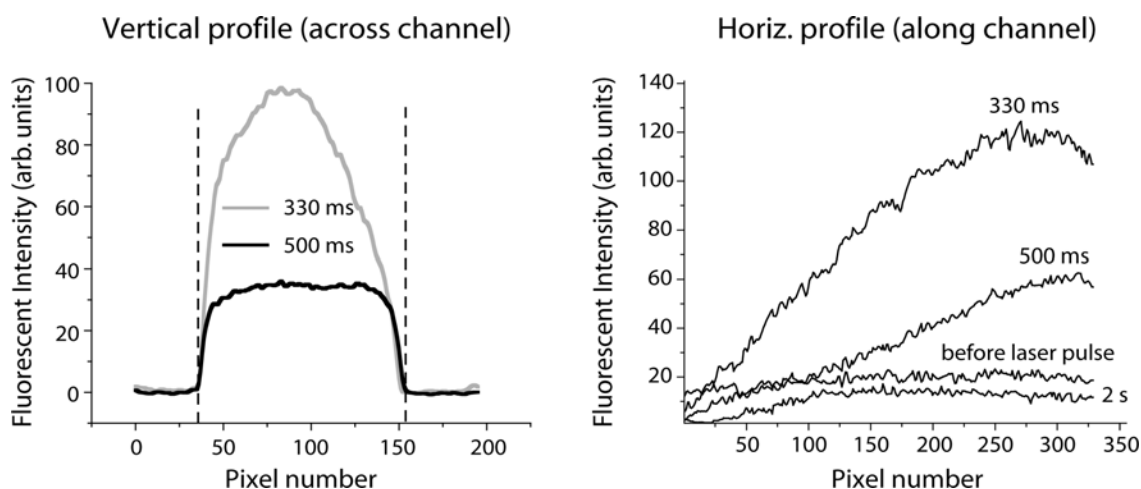
Figure 7.14: Quantitative analysis of the fluorescent images in Figure 7.13 demonstrating that the fluorescent product resorufin is produced throughout the entire width of the microfluidic channel and is convected downstream with the main hydrodynamic flow.

7.4.3 Mixing Discussion

These time-resolved imaging and fluorescence methods have enabled the examination of both the hydrodynamic events that lead to the formation of a small volume of mixed fluid and its downstream convection in the microfluidic channel on nanosecond to second time scales. The initiating event for the mixing process is the formation of a laser-induced plasma within the aqueous medium. Plasma formation is a nonlinear process and does not rely on linear optical absorption by the aqueous medium. Thus the proposed method is applicable at any optically accessible location within a microfluidic device. The process of laser-induced plasma formation in water is a well-studied phenomenon whose lifetime, for nanosecond pulse widths, is governed by the duration of the laser pulse [132]. The rapid plasma expansion results in cavitation bubble formation, expansion, and collapse; processes that are all clearly visualized within the microfluidic channel. The confinement offered by the microfluidic channel results in maximum bubble volumes that are smaller than those observed for expansion in a free medium. The confinement also results in bubble splitting and jet formation upon bubble collapse that accomplishes the fluid mixing. While cavitation bubble dynamics in the proximity of single rigid or elastic boundaries [131, 132] as well as bubble-bubble interactions within microfluidic channels [24] have been studied, we believe this is the first examination of the dynamics of a single cavitation bubble within a channel whose dimensions are similar in size to the bubble itself. The hydrodynamic resistance offered by the microfluidic channel walls results in the more rapid collapse of the bubble surfaces that are not adjacent to the channel walls. This leads to asymmetric bubble collapse, specifically invagination or `pinching' of the bubble wall in the

midplane of the channel, followed by jet formation and a second bubble splitting event. While the impact of cavitation-induced jets have been known to cause pitting damage in metal films and tissue puncture in ophthalmic surgery [135], we do not observe mechanical damage due to the low laser pulse energies used and the mechanical resilience of PDMS. Instead, upon hitting the channel walls, the jet flows outward, leading either to whorl formation in the case of the 200 μm channel, or more complex patterns seen in the case of the 100 μm channel. The bubble collapse dynamics also caused stretching and folding of fluid elements, characteristics necessary for good micro-mixing. We also observed that the mixing region extended to regions upstream of the flow leading to `active mixing', defined as a process in which the fluid interfaces interact with the flow and modify it [82]. Clearly, the imaging system employed here could find general use for the examination and analysis of other fast biophysical effects in microfluidic devices [39].

Although mixers based on the use of ultrasound to generate cavitation bubbles have been described [66, 68, 146] there are several important differences between our method and those that employ ultrasound. In ultrasonic mixers, an acoustic wave is launched into the medium by a piezoelectric transducer that is integrated onto the device. Mixing occurs due to micro-flows and eddies set up by cavitation micro-streaming. In our method the localized flow instability and mixing is produced by a single bubble, as opposed to the formation of multiple bubbles as is the case for cavitation micro-streaming. The site of bubble formation (and hence mixing) can be accurately controlled by focusing the laser microbeam with a high numerical objective at the desired location. The bubble collapse was found to produce flow patterns that

were reproducible on both microsecond and millisecond time scales. Since flow patterns produced during ultrasound mixing in microchannels have not been studied it is not known whether similar processes are operative in these methods.

The production of cavitation bubble-induced mixing through laser-induced plasma formation may be cause for concern due to potential for direct damage by the plasma. While the plasma itself can reach high temperatures [112], the plasma is typically very small (~10 μm diameter), has a short lifetime (~ 20 ns), and cools rapidly upon expansion. Nonetheless, it is likely that an amount of fluid equivalent to the plasma volume is thermally inactivated. Experimental studies show that for the laser parameters used in this study, the plasma volume is well-described by an ellipsoid ~13 μm in length and ~8 μm in diameter resulting in a plasma volume of ~ 0.7 pL [26, 126]. This suggests that there is over a 1000:1 ratio between the volume of mixed fluid (~1 nL) to the volume of reactants destroyed by plasma formation. Moreover, even if the entire energy of the 20 μJ laser pulse is confined to the mixed fluid volume on the order of 1 nL, the resulting temperature rise is no more than 5 degrees Kelvin. Our successful demonstration of the HRP-catalyzed reaction of Amplex Red and H_2O_2 resulting in resorufin demonstrates that any generated heat did not result in significant inactivation of the reactants, catalyst, or product. One potential limitation of this technique is that the plasma does indeed vaporize a small volume of fluid thereby leading to the generation of vapor bubbles that persist after the cavitation bubble collapse. Although we did not encounter problems when operating the Nd:YAG laser at a pulse repetition rate of 0.4 Hz, higher pulse repetition rates may lead to the generation of large numbers of vapor bubbles that could block the channel. This can be remedied

by the use of shorter wavelengths (e.g λ = 355 nm) or shorter laser pulse durations (ps or fs) [134, 136]. Reductions in wavelength and/or pulse duration enable the formation of a laser-induced plasma at lower pulse energies ($\leq$ 1 µJ/pulse) with less energy available for vaporization. However, this may also lead to a smaller amount of bubble energy, leading to less violent bubble collapse and the production of smaller volumes of mixed fluid. Another approach could be surface modification of the channel walls to make them more hydrophilic and less prone to bubble sticking. Clearly the promising results of this study need to be followed up with a detailed examination of the dependence of the fluid mixing process on laser pulse duration, pulse energy, wavelength, and pulse repetition rate.

7.5   Conclusion

In this chapter, we have demonstrated the ability to achieve precise cellular manipulations within the confines of a microfluidic channel, such as targeted lysis of a single cell for subsequent biochemical analysis, and localized cutting of axons for the study of central nervous system injury and regrowth. Further studies regarding these applications are currently underway in our laboratory.

We have also demonstrated a novel technique for mixing two streams within a microfluidic channel using laser generated cavitation bubbles. Time resolved imaging allowed visualization of the complex fluid patterns produced upon bubble collapse. While the cavitation bubble formation expansion and collapse was complete on a time scale of ~ 25 µs, the restoration of laminar flow did not occur until 50 ms following the laser pulse delivery. The cavitation bubble dynamics disrupted the parallel laminar

flow and led to the formation of a local volume of mixed fluid. We estimated this mixed volume to be in the range of 0.5 - 1.5 nL. Fluorescence detection downstream of the mixing site confirmed that the delivery of each Nd:YAG laser pulse resulted in the formation of a mixed bolus of fluid that occupied the entire channel and was convected downstream with the main flow. We also used fluorescence video microscopy to demonstrate that laser induced mixing can be used to initiate an enzyme catalyzed reaction within a microfluidic system. This method of mixing using laser generated cavitation bubbles may be particularly attractive for microfluidic applications since no modifications need be made to the microfluidic channel geometry and there is complete flexibility in the location of the mixing site. Moreover, the time-resolved imaging system detailed in this report could be used for the visualization of other fast phenomena in microfluidics.

7.6   Acknowledgements

REFERENCES

1. Aggen JB, Nairn AC, Chamberlin R: Regulation of protein phosphatase-1. *Journal of Biological Chemistry* 7:R13-23, 2000

2. Amy R, Storb R: Selective mitochondrial damage by a ruby laser microbeam: An electron microsocpic study. *Science* 150:756-757, 1965

3. Anderson E, Tate M: Open access to novel dual flow chamber technology for in vitro cell mechanotransduction, toxicity and pharamacokinetic studies. *Biomedical Engineering Online* 6, 2007

4. Bao S, Thrall B, Miller D: Transfection of a reporter plasmid into cultured cells by sonoporation in vitro. *Ultrasound Medicine and Biology* 23:953-959, 1997

5. Becker-Hapak M, McAllister S, Dowdy S: TAT-mediated protein transduction into mammalian cells. *Methods in Cell Biology* 24:247-256, 2001

6. Berns M: A History of Laser Scissors (Microbeams). *Methods in Cell Biology* 82:3-58, 2007

7. Berns M: Partial cell irradiation with a tunable organic-dye laser. *Nature* 240:483-&, 1972

8. Berns M, Olson R, Rounds D: Argon laser micro-irradiation of nucleoli. *Journal of Cell Biology* 43:621-&, 1969

9. Berns M, Olson R, Rounds D: In vitro production of chromosomal lesions with an argon laser microbeam. *Nature* 221:74-&, 1969

10. Berns M, Wang Z, Dunn A, Wallace V, Venugopalan V: Gene inactivation by multiphoton-targeted photochemistry. *Proceedings of the National Academy of Sciences of the United States of America* 97:9504-9507, 2000

11. Berns MW: A possible two-photon effect in vitro using a focused laser beam. *Biophysical Journal* 16:973-977, 1976

12. Berns MW, Aist J, Edwards J, Strahs K, Girton J, McNeill P, Rattner JB, Kitzes M, Hammer-Wilson M, Liaw LH, Siemens A, Koonce M, Peterson S, Brenner S, Brut J, Water R, Bryant PJ, Dyk Dv, Colombe J, Cahill T, Berns GS: Laser microsurgery in cell and developmental biology. *Science* 213:505-513, 1981

13. Bessis M, Gires F, Mayer G, Nomarski G: Irradiation des organites cellulaires a l'aide d'un laser a rubis. *C.R. Acad.Sci* 225:1010-1012, 1962

14. Bilek AM, Dee KC, Gaver DP: Mechanisms of surface-tension-induced epithelial cell damage in a model of pulmonary airway reopening. *Journal of Applied Physiology* 94:770-783, 2003

15. Boal D: *Mechanisms of the Cell*. Cambridge, UK, Cambridge University Press, 2002

16. Botvinick E, Wang Y: Laser tweezers in the study of mechanobiology in live cells. *Methods in Cell Biology. Laser Manipulation of Cells and Tissues* 82:497-523, 2007

17. Bourgeois F, Ben-Yakar A: Femtosecond laser nanoaxotomy properties and their effect on axonal recovery in C-elegans. *Optics Express* 15:8521-8531, 2007

18. Brennen C: *Cavitation and Bubble Dynamics*. New York, Oxford University Press, 1995

19. Calmettes P, Berns M: Laser-induced multiphoton processes in living cells. *Proceedings of the National Academy of Sciences of the United States of America- Biological Sciences* 80:7197-7199, 1983

20. Campbell CJ, Grzybowski BA: Microfluidic mixers: from microfabricated to self-assembling devices. *Philosophical Transactions of the Royal Society of London Series a-Mathematical Physical and Engineering Sciences* 362:1069-1086, 2004

21. Caprara A, Reali GC: Time-Resolved M2 of Nanosecond Pulses from a Q-Switched Variable-Reflectivity-Mirror Nd-Yag Laser. *Optics Letters* 17:414-416, 1992

22.   Celis J: Microinjection of somatic cells with micropipettes - comparison with other transfer techniques. *Biochemical Journal* 223:281-291, 1984

23.   Chen CS, Tan J, Tien J: Mechanotransduction at cell-matrix and cell-cell contacts. *Annual Review of Biomedical Engineering* 6:275-302, 2004

24.   Chen YH, Chu HY, I L: Interaction and fragmentation of pulsed laser induced microbubbles in a narrow gap. *Physical Review Letters* 96:-, 2006

25.   Clark I, Hanania E, Stevens J, Gallina M, Fieck A, Brandes R, Palsson B, Koller M: Optoinjection for efficient targeted delivery of a broad range of compounds and macromolecules into diverse cell types. *Journal of Biomedical Optics* 11:-, 2006

26.   Colombelli J, Grill SW, Stelzer EHK: Ultraviolet diffraction limited nanosurgery of live biological tissues. *Review of Scientific Instruments* 75:472-478, 2004

27.   Conn P [ed]: *Laser capture in microscopy and microdissection*. New York, Academic Press, 2002

28.   Cooper MG, Lloyd AJP: Microlayer in Nucleate Pool Boiling. *International Journal of Heat and Mass Transfer* 12:895-&, 1969

29.   Courant R, Hilbert D: *Methods of Mathematical Physics*. New York, Wiley-Interscience, 1962

30.   Dafna B, SRina S, Irena S: Laser Capture Microdissection and Laser Pressure Catapulting as Tools to Study Gene Expression in Individual Cells of a Complex Tissue. *Methods in Cell Biology* 82:675-707, 2007

31.   Deval J, Tabeling P, Ho CM: In: *15th IEEE Int. Conf. MEMS*, pp 36-39., 2002

32.   Doukas A, Mcauliffe D, Lee S, Venugopalan V, Flotte T: Physical Factors Involved in Stress Wave-Induced Cell Injury - The Effect of Stress Gradient. *Ultrasound in Medicine and Biology* 21:961-967, 1995

33. Eldstrom J, La K, Mathers D: Polycationic lipids translocate lipopolysaccharide into HeLa cells. *Biotechniques* 28:510-+, 2000

34. Faurie C, Golzio M, Phez E, Teissie J, Rols M: Electric field-induced cell membrane permeabilization and gene transfer: Theory and experiments. *Engineering in Life Sciences* 5:179-186, 2005

35. Felsenfeld D, Schwartzberg P, Venegas A, Tse R, Sheetz M: Selective regulation of integrin-cytoskeleton interactions by the tyrosine kinase Src. *Nature Cell Biology* 1:200-206, 1999

36. Garstecki P, Fuerstman MJ, Fischbach MA, Sia SK, Whitesides GM: Mixing with bubbles: a practical technology for use with portable microfluidic devices. *Lab on a Chip* 6:207-212, 2006

37. Glasgow I, Aubry N: Enhancement of microfluidic mixing using time pulsing. *Lab on a Chip* 3:114-120, 2003

38. Grill S, Gonczy P, Stelzer E, Hyman A: Polarity controls forces governing asymmetric spindle positioning in the Caenorhabditis elegans embryo. *Nature* 409:630-633, 2001

39. Grumann M, Brenner T, Beer C, Zengerle R, Ducree J: Visualization of flow patterning in high-speed centrifugal microfluidics. *Review of Scientific Instruments* 76:-, 2005

40. Hapala I: Breaking the barrier: Methods for reversible permeabilization of cellular membranes. *Critical Reveiws in Biotechnology* 17:105-122, 1997

41. He B, Burke BJ, Zhang X, Zhang R, Regnier FE: A picoliter-volume mixer for microfluidic analytical systems. *Analytical Chemistry* 73:1942-1947, 2001

42. He MY, Edgar JS, Jeffries GDM, Lorenz RM, Shelby JP, Chiu DT: Selective encapsulation of single cells and subcellular organelles into picoliter- and femtoliter-volume droplets. *Analytical Chemistry* 77:1539-1544, 2005

43. Hellman A, Rau K, Yoon H, Bae S, Palmer J, Phillips K, Allbritton N, Venugopalan V: Laser-induced mixing in microfluidic channels. *Analytical Chemistry* 79:4484-4492, 2007

44. Hellman A, Rau K, Yoon H, Venugopalan V: Biophysical response to pulsed laser microbeam-induced cell lysis and molecular delivery. *Journal of Biophotonics* 1:24-35, 2008

45. Hertzog DE, Michalet X, Jager M, Kong XX, Santiago JG, Weiss S, Bakajin O: Femtomole mixer for microsecond kinetic studies of protein folding. *Analytical Chemistry* 76:7169-7178, 2004

46. Ho CM, Tai YC: Micro-electro-mechanical-systems (MEMS) and fluid flows. *Annual Review of Fluid Mechanics* 30:579-612, 1998

47. Hutson M, Tokutake Y, Chang M, Bloor J, Venakides S, Kiehart D, Edwards G: Forces for morphogenesis investigated with laser microsurgery and quantitative modeling. *Science* 300:145-149, 2003

48. Iwanaga S, Kaneko T, Fujita K, Smith N, Nakamura O, Takamatsu T, Kawata S: Location-dependent photogeneration of calcium waves in HeLa cells. *Cell Biochemistry and Biophysics* 45:167-176, 2006

49. Jacobson SC, McKnight TE, Ramsey JM: Microfluidic devices for electrokinetically driven parallel and serial mixing. *Analytical Chemistry* 71:4455-4459, 1999

50. Johnson TJ, Ross D, Locascio LE: Rapid microfluidic mixing. *Analytical Chemistry* 74:45-51, 2002

51. Junge L, Ohl C, Wolfrum B, Arora M, Ikink R: Cell detachment method using shock-wave-induced cavitation. *Ultrasound in Medicine and Biology* 29:1769-1776, 2003

52. Keller U: Recent developments in compact ultrafast lasers. *Nature* 424:831-838, 2003

53. Khodjakov A, Cole R, Oakley B, Rieder C: Centrosome-independent mitotic spindle formation in vertebrates. *Current Biology* 10:59-67, 2000

54. Khodjakov A, Cole R, Rieder C: A synergy of technologies: Combining laser microsurgery with green fluorescent protein tagging. *Cell Motility and the Cytoskeleton* 38:311-317, 1997

55. Khodjakov A, Rieder C, Sluder G, Sibon O, Cassels G, Wang C: De novo formation of centrosomes in vertebrate somatic cells. *Molecular Biology of the Cell* 13:49A-49A, 2002

56. Kim JS, Krasieva TB, LaMorte V, Taylor AM, Yokomori K: Specific recruitment of human cohesin to laser-induced DNA damage. *Journal of Biological Chemistry* 277:45149-53, 2002

57. Knight JB, Vishwanath A, Brody JP, Austin RH: Hydrodynamic focusing on a silicon chip: Mixing nanoliters in microseconds. *Physical Review Letters* 80:3863-3866, 1998

58. Kodama T, Doukas A, Hamblin M: Shock wave-mediated molecular delivery into cells. *Biochemica et Biophysica Acta - Molecular Cell Research* 1542:186-194, 2002

59. Kodama T, Hamblin M, Doukas A: Cytoplasmic molecular delivery with shock waves: Importance of impulse. *Biophysical Journal* 79:1821-1832, 2000

60. Koshiyama K, Kodama T, Yano T, Fujikawa S: Structural change in lipid bilayers and water penetration induced by shock waves: Molecular dynamics simulations. *Biophysical Journal* 91:2198-2205, 2006

61. Krasieva TB, Chapman CF, LaMorte VJ, Venugopalan V, Berns MW, Tromberg BJ: Cell Permeabilization and molecular transport by laser microirradiation. In: *SPIE*, pp 38-44, 1998

62. Lee S, Anderson T, Zhang H, Flotte T, Doukas A: Alteration of cell membrane by stress waves in vitro. *Ultrasound in Medicine and Biology* 22:1285-1293, 1996

63.   Lee S, Doukas A: Laser-generated stress waves and their effects on the cell membrane. *IEEE Journal of Seclected Topics in Quantum Electronics* 5:997-1003, 1999

64.   Liau A, Karnik R, Majumdar A, Cate JHD: Mixing crowded biological solutions in milliseconds. *Analytical Chemistry* 77:7618-7625, 2005

65.   Lin CP, Kelly NW, Sibayan SAB, Latina MA, Anderson RR: Selective cell killing by microparticle absorption of pulsed laser radiation. *Ieee Journal of Selected Topics in Quantum Electronics* 5:963-968, 1999

66.   Liu RH, Lenigk R, Druyor-Sanchez RL, Yang JN, Grodzinski P: Hybridization enhancement using cavitation microstreaming. *Analytical Chemistry* 75:1911-1917, 2003

67.   Liu RH, Stremler MA, Sharp KV, Olsen MG, Santiago JG, Adrian RJ, Aref H, Beebe DJ: Passive mixing in a three-dimensional serpentine microchannel. *Journal of Microelectromechanical Systems* 9:190-197, 2000

68.   Liu RH, Yang JN, Pindera MZ, Athavale M, Grodzinski P: Bubble-induced acoustic micromixing. *Lab on a Chip* 2:151-157, 2002

69.   Lokhandwalla M, Sturtevant B: Mechanical haemolysis in shock wave lithotripsy (SWL): I. Analysis of cell deformation due to SWL flow-fields. *Physics in Medicine and Biology* 46:413-437, 2001

70.   Lorenzen-Schmidt I, Schmid-Schonbein G, Giles W, McCulloch A, Chien S, Omens J: Chronotropic response of cultured neonatal rat ventricular myocytes to short term fluid shear. *Cell Biochemistry and Biophysics* 46:113-122, 2006

71.   Lu LH, Ryu KS, Liu C: A magnetic microstirrer and array for microfluidic mixing. *Journal of Microelectromechanical Systems* 11:462-469, 2002

72.   McNeil P, Miyake K, Vogel S: The endomembrane requirement for cell surface repair. *Proceedings of the National Academy of Sciences of the United States of America* 100:4592-4597, 2003

73. Meredith G, Sims C, Soughayer J, Allbritton N: Measurement of kinase activation in single mammalian cells. *Nature Biotechnology* 18:309-312, 2000

74. Miller M: Cell size relations for sonolysis. *Ultrasound in Medicine and Biology* 30:1263-1267, 2004

75. Miller M, Miller D, Brayman A: A review of in vitro bioeffects of inertial ultrasonic cavitation from a mechanistic perspective. *Ultrasound in Medicine and Biology* 22:1131-1154, 1996

76. Miller M, Sherman T, Brayman A: Comparative sensitivity of human and bovine erythrocytes to sonolysis by 1-MHz ultrasound. *Ultrasound in Medicine and Biology* 26:1317-1326, 2000

77. Mitragotri S: Innovation - Healing sound: the use of ultrasound in drug delivery and other therapeutic applications. *Nature Reviews Drug Discovery* 4:255-260, 2005

78. Noack J, Vogel A: Laser-induced plasma formation in water at nanosecond to femtosecond time scales: Calculation of thresholds, absorption coefficients, and energy density. *IEEE Journal of Quantum Electronics* 35:1156-1167, 1999

79. Oddy MH, Santiago JG, Mikkelsen JC: Electrokinetic instability micromixing. *Analytical Chemistry* 73:5822-5832, 2001

80. Ohl C, Arora M, Ikink R, de Jong N, Versluis M, Delius M, Lohse D: Sonoporation from jetting cavitation bubbles. *Biophysical Journal* 91:4285-4295, 2006

81. Ohl C, Wolfrum B: Detachment and sonoporation of adherent HeLa-cells by shock wave-induced cavitation. *Biochemica et Biophysica Acta - General Subjects* 1624:131-138, 2003

82. Ottino JM: *The kinematics of mixing: stretching, chaos and transport*. Cambridge, UK, Cambridge University Press, 1988

83. Ottino JM, Wiggins S: Introduction: mixing in microfluidics. *Philosophical Transactions of the Royal Society of London Series a-Mathematical Physical and Engineering Sciences* 362:923-935, 2004

84. Palsson B, Koller M, Eisfeld T: Method and apparatus for selectively targeting specific cells within a mixed cell population. U.S., 2003

85. Papautsky I, Brazzle J, Ameel T, Frazier AB: Laminar fluid behavior in microchannels using micropolar fluid theory. *Sensors and Actuators a-Physical* 73:101-108, 1999

86. Park HY, Qiu XY, Rhoades E, Korlach J, Kwok LW, Zipfel WR, Webb WW, Pollack L: Achieving uniform mixing in a microfluidic device: Hydrodynamic focusing prior to mixing. *Analytical Chemistry* 78:4465-4473, 2006

87. Park J, Vahidi B, Kim H, Rhee S, Jeon N: Quantitative Analysis of CNS Axon Regeneration Using a Microfluidic Neuron Culture Device. *Biochip Journal* 2:44-51, 2008

88. Park J, Vahidi B, Taylor A, Rhee S, Jeon N: Microfluidic culture platform for neuroscience research. *Nature Protocols* 1:2128-2136, 2006

89. Paul PH, Garguilo MG, Rakestraw DJ: Imaging of pressure- and electrokinetically driven flows through open capillaries. *Analytical Chemistry* 70:2459-2467, 1998

90. Pitsillides CM, Joe EK, Wei XB, Anderson RR, Lin CP: Selective cell targeting with light-absorbing microparticles and nanoparticles. *Biophysical Journal* 84:4023-4032, 2003

91. Quinto-Su P, Lai H, Yoon H, Sims C, Allbritton N, Venugopalan V: Examination of laser microbeam cell lysis in a PDMS microfluidic channel using time-resolved imaging. *Lab on a Chip* 8:408-414, 2008

92. Quinto-Su P, Venugopalan V: Mechanisms of Laser Cellular Microsurgery. *Methods in Cell Biology* 82:113-151, 2007

93. Rau K, Guerra A, Vogel A, Venugopalan V: Investigation of laser-induced cell lysis using time-resolved imaging. *Applied Physics Letters* 84:2940-2942, 2004

94. Rau K, Quinto-Su P, Hellman A, Venugopalan V: Pulsed laser microbeam-induced cell lysis: Time-resolved imaging and analysis of hydrodynamic effects. *Biophysical Journal* 91:317-329, 2006

95. Rhodes K, Clark I, Zatcoff M, Eustaquio T, Hoyte K, Koller M: Cellular Laserfection. *Methods in Cell Biology* 82:309-333, 2007

96. Rink K, Delacretaz G, Salathe RP: Fragmentation Process of Current Laser Lithotriptors. *Lasers in Surgery and Medicine* 16:134-146, 1995

97. Ryan PL, Foty RA, Kohn J, Steinberg MS: Tissue spreading on implantable substrates is a competitive outcome of cell-cell vs. cell-substratum adhesivity. *Proceedings of the National Academy of Sciences of the United States of America* 98:4323-4327, 2001

98. Salazar G, Jensen-McMullen C, Ng S, Bachman M, Sims C, Li G, Allbritton N: Rapid, nondisruptive isolation of single adherent cells from a heterogeneous population. *Biophysical Journal* 88:375A-375A, 2005

99. Salazar G, Wang Y, Young G, Bachman M, Sims C, Li G, Allbritton N: Micropallet arrays for the separation of single, adherent cells. *Analytical Chemistry* 79:682-687, 2007

100. Schlichting H: *Boundary-Layer Theory,* pp 90-91. Englewood Cliffs, NJ, McGraw-Hill, 1979

101. Seong GH, Crooks RM: Efficient mixing and reactions within microfluidic channels using microbead-supported catalysts. *Journal of the American Chemical Society* 124:13360-13361, 2002

102. Shapiro H: *Practical Flow Cytometry*. New York, Wiley-Liss, 2003

103. Shimozono S, Miyawaki A: Engineering FRET constructs using CFP and YFP. *Fluorescent Proteins, Second Edition* 85:381-+, 2008

104. Sims CE, Allbritton NL: Metabolism of inositol 1,4,5-trisphosphate and inositol 1,3,4,5-tetrakisphosphate by the oocytes of Xenopus laevis. *J Biol Chem* 273:4052-8, 1998

105. Sims CE, Allbritton NL: Single-cell kinase assays: opening a window onto cell behavior. *Curr Opin Biotechnol* 14:23-8, 2003

106. Sims CE, Meredith GD, Krasieva TB, Berns MW, Tromberg BJ, Allbritton NL: Laser-micropipet combination for single-cell analysis. *Anal Chem* 70:4570-7, 1998

107. Smith N, Fujita K, Kaneko T, Katoh K, Nakamura O, Kawata S, Takamatsu T: Generation of calcium waves in living cells by pulsed-laser-induced photodisruption. *Applied Physics Letters* 79:1208-1210, 2001

108. Sonden A, Svensson B, Roman N, Brismar B, Palmblad J, Kjellstrom BT: Mechanisms of shock wave induced endothelial cell injury. *Lasers in Surgery and Medicine* 31:233-241, 2002

109. Soughayer J, Krasieva T, Jacobson S, Ramsey J, Tromberg B, Allbritton N: Characterization of cellular optoporation with distance. *Analytical Chemistry* 72:1342-1347, 2000

110. Spielman L, Goren SL: Improving Resolution in Coulter Counting by Hydrodynamic Focusing. *Journal of Colloid and Interface Science* 26:175-&, 1968

111. Squires TM, Quake SR: Microfluidics: Fluid physics at the nanoliter scale. *Reviews of Modern Physics* 77:977-1026, 2005

112. Stolarski D, Hardman J, Bramlette C, Noojin G, Thomas T, Rockwell B, Roach W: *Proc. SPIE* 2391:100-109, 1995

113. Storb R, Amy R, RK W, B F, Bessis M: An electron microscope study of vitally stained single cells irradiated with a ruby laser microbeam. *Journal of Cell Biology* 31:11-29, 1966

114. Stroock AD, Dertinger SKW, Ajdari A, Mezic I, Stone HA, Whitesides GM: Chaotic mixer for microchannels. *Science* 295:647-651, 2002

115. Sundaram J, Mellein B, Mitragotri S: An experimental and theoretical analysis of ultrasound-induced permeabilization of cell membranes. *Biophysical Journal* 84:3087-3101, 2003

116. Suzuki H, Kasagi N, Ho CM: In: *3rd Int. Symp. Turbulence Shear Flow Phenomena*, pp 817-822, 2003

117. Tao W, Wilkinson J, Stanbridge E, Berns M: Direct gene-transfer into human cultured-cells facilitated by laser micropuncture of the cell membrane. *Proceedings of the national Academy of Sciences of the United States of America* 84:4180-4184, 1987

118. Taylor A, Blurton-Jones M, Rhee S, Cribbs D, Cotman C, Jeon N: A microfluidic culture platform for CNS axonal injury, regeneration and transport. *Nature Methods* 2:599-605, 2005

119. Taylor A, Rhee S, Tu C, Cribbs D, Cotman C, Jeon N: Microfluidic multicompartment device for neuroscience research. *Langmuir* 19:1551-1556, 2003

120. Therriault D, White SR, Lewis JA: Chaotic mixing in three-dimensional microvascular networks fabricated by direct-write assembly. *Nature Materials* 2:265-271, 2003

121. Thomas S, Brugge J: Cellular functions regulated by Src family kinases. *Annual Review of Cell and Developmental Biology* 13:513-609, 1997

122. Ting A, Kain K, Klemke R, Tsien R: Genetically encoded fluorescent reporters of protein tyrosine kinase activities in living cells. *Proceedings of the National Academy of Sciences of the United States of America* 98:15003-15008, 2001

123. Turovets I, Lewis A, Palanker D, Gilo H, Vilenz A, Broder J, Lewis S: Permeabilizing millions of cells with single pulses of an excimer-laser. *Biotechniques* 15:1022-&, 1993

124. Vahidi B, Park J, Kim H, Jeon N: Microfluidic-based strip assay for testing the effects of various surface-bound inhibitors in spinal cord injury. *Journal of Neuroscience Methods* 170:188-96, 2008

125. VanBavel E: Effects of shear stress on endothelial cells: Possible relevance for ultrasound applications. *Progress in Biophysics & Molecular Biology* 93:374-383, 2007

126. Venugopalan V, Guerra A, Nahen K, Vogel A: Role of laser-induced plasma formation in pulsed cellular microsurgery and micromanipulation. *Physical Review Letters* 88:-, 2002

127. Vogel A: Nonlinear absorption: Intraocular microsurgery and laser lithotripsy. *Physics in Medicine and Biology* 42:895-912, 1997

128. Vogel A, Busch S, Jungnickel K, Birngruber R: Mechanisms of Intraocular Photodisruption with Picosecond and Nanosecond Laser-Pulses. *Lasers in Surgery and Medicine* 15:32-43, 1994

129. Vogel A, Busch S, Parlitz U: Shock wave emission and cavitation bubble generation by picosecond and nanosecond optical breakdown in water. *Journal of the Acoustical Society of America* 100:148-165, 1996

130. Vogel A, Horneffer V, Lorenz K, Linz N, Huttmann G, Gebert A: Principles of laser microdissection and catapulting of histologic specimens and live cells. *Methods in Cell Biology* 82:153-205, 2007

131. Vogel A, Lauterborn W, Timm R: Optical and acoustic investigations of the dynamics of laser-produced cavitation bubbles near a solid boundary. *Journal of Fluid Mechanics* 206:299-338, 1989

132. Vogel A, Nahen K, Theisen D, Noack J: Plasma formation in water by picosecond and nanosecond Nd:YAC laser pulses.1. Optical breakdown at threshold and superthreshold irradiance. *IEEE Journal of Seclected Topics in Quantum Electronics* 2:847-860, 1996

133. Vogel A, Noack J, Huttman G, Paltauf G: Mechanisms of femtosecond laser nanosurgery of cells and tissues. *Applied Physics B - Lasers and Optics* 81:1015-1047, 2005

134. Vogel A, Noack J, Nahen K, Theisen D, Busch S, Parlitz U, Hammer D, Noojin G, Rockwell B, Birngruber R: Energy balance of optical breakdown in water at nanosecond to femtosecond time scales. *Applied Physics B - Lasers and Optics* 68:271-280, 1999

135. Vogel A, Schweiger P, Frieser A, Asiyo MN, Birngruber R: Intraocular Nd-Yag Laser-Surgery - Light Tissue Interaction, Damage Range, and Reduction of Collateral Effects. *IEEE Journal of Quantum Electronics* 26:2240-2260, 1990

136. Vogel A, Venugopalan V: Mechanisms of pulsed laser ablation of biological tissues. *Chemical Reviews* 103:577-644, 2003

137. Wang Y, Botvinick E, Zhao Y, Berns M, Usami S, Tsien R, Chien S: Visualizing the mechanical activation of Src. *Nature* 434:1040-1045, 2005

138. Wang Y, Young G, Bachman M, Sims C, Li G, Allbritton N: Collection and expansion of single cells and colonies released from a micropallet array. *Analytical Chemistry* 79:2359-2366, 2007

139. Ward M, Wu J, Chiu J: Ultrasound-induced cell lysis and sonoporation enhanced by contrast agents. *Journal of the Acoustical Society of America* 105:2951-2957, 1999

140. Williams A, Hughes D, Nyborg W: Hemolysis near a transversely oscillating wire. *Science* 169:871-&, 1970

141. Wilson AK, Horwitz J, De Lanerolle P: Evaluation of the electroinjection method for introducing proteins into living cells. *Am J Physiol* 260:C355-63, 1991

142. Wolfrum B, Mettin R, Kurz T, Lauterborn W: Observations of pressure-wave-excited contrast agent bubbles in the vicinity of cells. *Applied Physics Letters* 81:5060-5062, 2002

143. Wu J: Shear stress in cells generated by ultrasound. *Progress in Biophysics & Molecular Biology* 93:363-373, 2007

144. Wu J, Ross J, Chiu J: Reparable sonoporation generated by microstreaming. *Journal of the Acoustical Society of America* 111:1460-1464, 2002

145. Yanik M, Cinar H, Cinar H, Gibby A, Chisholm A, Jin Y, Ben-Yakar A: Nerve regeneration in Caenorhabditis elegans after femtosecond laser axotomy. *IEEE Journal of Selected Topics in Quantum Electronics* 12:1283-1291, 2006

146. Yaralioglu GG, Wygant IO, Marentis TC, Khuri-Yakub BT: Ultrasonic mixing in microfluidic channels using integrated transducers. *Analytical Chemistry* 76:3694-3698, 2004

147. Zayhowski J: Microchip lasers. *Optical Materials* 11:255-267, 1999

148. Zayhowski J: Q-switched microchip lasers find real-world application. *Laser Focus World* 35:129-+, 1999

149. Zhou MJ, Diwu ZJ, PanchukVoloshina N, Haugland RP: A stable nonfluorescent derivative of resorufin for the fluorometric determination of trace hydrogen peroxide: Applications in detecting the activity of phagocyte NADPH oxidase and other oxidases. *Analytical Biochemistry* 253:162-168, 1997